Purdue University
Purdue e-Pubs

Department of Electrical and Computer Engineering Technical Reports | Department of Electrical and Computer Engineering

5-1-1991

Computer Simulation and Device Physics of SiGe Heterojunction Bipolar Transistors

Troy Thomas Herman
Purdue University

Follow this and additional works at: https://docs.lib.purdue.edu/ecetr

Herman, Troy Thomas, "Computer Simulation and Device Physics of SiGe Heterojunction Bipolar Transistors" (1991). *Department of Electrical and Computer Engineering Technical Reports.* Paper 738.
https://docs.lib.purdue.edu/ecetr/738

This document has been made available through Purdue e-Pubs, a service of the Purdue University Libraries. Please contact epubs@purdue.edu for additional information.

COMPUTER SIMULATION AND DEVICE PHYSICS OF SiGe HETEROJUNCTION BIPOLAR TRANSISTORS

A Thesis

Submitted to the Faculty

of

Purdue University

by

Troy Thomas Herman

In Partial Fulfillment of the

Requirements for the Degree

of

Master of Science in Electrical Engineering

May 1991

ACKNOWLEDGEMENTS

I would like to express my gratitude to several important people whose assistance has been priceless throughout the past two years. First and foremost is my major professor Mark Lundstrom. His expertise stimulated my thinking and helped me through many difficult jams. Professor Jeff Gray has lent a helping hand several times, and I have picked up many useful hints from our conversations. I would also like to thank Professor John Nyenhuis for his assistance with electromagnetics problems and his willingness to be part of my graduate committee. My colleagues Mark Stettler, Paul Dodd, and Amitava Das have been called upon for their technical knowledge many times. In addition, we have shared many good conversations. Michael "codemaster" McLennan has answered many questions concerning FORTRAN and the computer systems at Purdue. I must thank my fiance, Joanne, and my family for their patience and support while I have been in school. Finally, I would like to especially thank Dr. Ming Liaw and Motorola for funding this research through the Motorola University Partnerships in Research Program. Without the support of each of the aforementioned, this work would not have been possible.

To my fiance Joanne for her enduring love and patience

TABLE OF CONTENTS

Page

LIST OF FIGURES....................vi

LIST OF TABLES....................ix

ABSTRACT....................x

CHAPTER 1: INTRODUCTION....................1

1.1. Fundamentals of HBT Operation....................1
1.2. Overview of SiGe Technology....................6
1.3. History of SiGe HBT's....................10
1.4. Research Objectives and Thesis Overview....................11

CHAPTER 2: MATERIAL PARAMETERS....................12

2.1. Introduction....................12
2.2. Bandgap and Bandgap Narrowing....................12
2.3. Density of States....................14
2.4. Dielectric Constant and Electron Affinity....................16
2.4.1. Dielectric Constant....................16
2.4.2. Electron Affinity....................17
2.5. Bulk Recombination and Carrier Lifetimes....................18
2.6. Carrier Mobilities....................19
2.6.1. Silicon Mobility....................20
2.6.2. $Si_{1-x}Ge_x$ Mobility....................23
2.7. Approach for Modelling Strain Effects....................27
2.8. Summary....................30

Page

CHAPTER 3: MODEL DEVELOPMENT....31

3.1. Introduction....31
3.2. PUPHS2D Code Structure....31
3.2.1. General Structure....31
3.2.2. Material Dependent Subroutines....34
3.2.3. Addition of Material Systems....35
3.3. Field Dependent Mobility....35
3.3.1. Introduction....35
3.3.2. Model Formulation....36
3.3.3. Solution of the Semiconductor Equations....44
3.3.4. Model Implementation....47
3.4. Model Verification....50
3.4.1. Introduction....50
3.4.2. NIN Diode....51
3.4.3. SiGe Heterojunction Diode....52
3.5. Summary....60

CHAPTER 4: A SIMULATION STUDY OF HIGH-SPEED BIPOLAR TRANSISTORS....61

4.1. Introduction....61
4.2. Conventional Silicon Bipolar Transistors....62
4.3. Advanced Silicon Bipolar Transistors....70
4.4. Conventional SiGe HBT's....73
4.5. Advanced SiGe HBT's....77
4.6. Future Microwave Bipolar Transistors....79
4.7. Summary....84

CHAPTER 5: SUMMARY AND RECOMMENDATIONS....86

5.1. Summary....86
5.2. Recommendations....87

LIST OF REFERENCES....89

LIST OF FIGURES

Figure Page

1.1 np $Si/Si_{0.85}Ge_{0.15}$ heterojunction band diagram. (a) mobile charge is fixed. (b) mobile charge is free to cross the junction. 2

1.2 Current components in a $Si/Si_{0.8}Ge_{0.2}$ HBT in forward active mode of operation. 4

1.3 Energy bandgap and lattice constant of various semiconductor systems. 7

1.4 Two-dimensional representation of SiGe growth on a Si (100) substrate. (a) unstrained SiGe is grown on a Si substrate. growth is: (b) pseudomorphic. (c) non-pseudomorphic. 8

1.5 Critical thickness of $Si_{1-x}Ge_x$ alloys grown on Si (100) substrates. 9

2.1 Electronic bandgap of strained and unstrained $Si_{1-x}Ge_x$ alloys. 13

2.2 Conduction band minima constant energy surfaces for (a) Si. (b) strained SiGe. 15

2.3 Intrinsic concentration versus 1000/T for Si and three SiGe alloys. 17

2.4 Silicon electron mobility versus impurity concentration. 24

2.5 Silicon hole mobility versus impurity concentration. 25

2.6 PUPHS2D $Si_{1-x}Ge_x$ electron mobilities. 27

2.7 PUPHS2D $Si_{1-x}Ge_x$ hole mobilities. 28

2.8 Node spacing and evaluation points within a strained alloy for a two-dimensional finite center difference mesh 29

3.1 PUPHS2D code structure. 33

3.2 Mobility versus driving force 40

3.3 Carrier velocity versus driving force 40

Figure Page

3.4 Electron diffusivity in lightly doped silicon as a function of field at 300K....44

3.5 Field-dependent mobility algorithm flowchart....48

3.6 Convergence of solution for field-dependent mobility and constant mobility models....50

3.7 NIN diode device structure....51

3.8 Electric field magnitude in an NIN diode....53

3.9 Electron mobility in an NIN diode....53

3.10 Electron concentration in an NIN diode....54

3.11 Electron velocity in an NIN diode....54

3.12 IV characteristics for the NIN diode....55

3.13 Electron velocity in the NIN diode at a bias of 1.5 volts....55

3.14 N^+P diode simulation structure....56

3.15 IV characteristics of the silicon homojunction diode and $Si/Si_{.8}Ge_{.2}$ heterojunction diode....56

3.16 Electron concentration in the silicon homojunction diode and the Si/SiGe heterojunction diode for V_A=0.7 volt....58

3.17 Excess electron concentration in the silicon diode for V_A=0.7V....59

3.18 Excess electron concentration in the Si/SiGe diode for V_A=0.7V....59

4.1 Conventional silicon bipolar transistor device structure....63

4.2 Electron concentration in the conventional silicon BJT at a bias of V_{BE}=0.9 volt, V_{CE}=1.0 volt....64

4.3 Electric field magnitude at V_{BE}=0.9 volt, V_{CE}=1.0 volt....65

4.4 Recombination rate at V_{BE}=0.9 volt, V_{CE}=1.0 volt....66

4.5 Hole concentration at V_{BE}=0.9 volt, V_{CE}=1.0 volt....67

Figure Page

4.6 Conventional silicon bipolar transistor Gummel plot. 68

4.7 Current gain of the conventional silicon bipolar transistor. 68

4.8 Unity gain cutoff frequency for the conventional transistor. 69

4.9 Advanced silicon bipolar transistor device structure. 71

4.10 Unity gain cutoff frequency for the advanced bipolar transistor. 72

4.11 Current gain of the advanced silicon bipolar transistor. 72

4.12 Gummel plot for the advanced silicon bipolar transistor. 73

4.13 Conventional SiGe HBT device structure. 75

4.14 Conventional SiGe HBT Gummel plot. 76

4.15 Current gain of the conventional SiGe HBT. 76

4.16 Cutoff frequency of the conventional SiGe HBT. 77

4.17 Hole concentration in the conventional SiGe HBT at V_{CE}=1V, V_{BE}=0.8V. 78

4.18 Graded base SiGe HBT device structure. 80

4.19 Gummel plot for the graded base SiGe HBT. 81

4.20 Current gain of the graded base SiGe HBT. 81

4.21 Cutoff frequency data for the graded base SiGe HBT. 82

LIST OF TABLES

Table Page

2.1 Caughy-Thomas silicon mobility constants....21

2.2 Arora silicon mobility constants....21

3.1 Caughy-Thomas velocity-field constants....37

3.2 Field-dependent mobility constants used in (3.3)....37

3.3 Field-dependent mobility constants used in (3.5)....38

4.1 Delay components for advanced transistors....84

ABSTRACT

Herman, Troy Thomas. M.S.E.E., Purdue University, May 1991.
Computer Simulation and Device Physics of SiGe Heterojunction Bipolar Transistors. Major Professor: Dr. Mark S. Lundstrom.

Recent advances in semiconductor growth technology have enabled the growth of SiGe strained layers on silicon substrates. Si/SiGe technology has a promising future, especially in microwave HBT applications. This work describes the development of an existing two-dimensional drift-diffusion device simulation program for accurate modelling of SiGe heterojunction bipolar transistors (HBT's). PUPHS2D (Purdue University Program for Heterostructure Simulation in Two Dimensions) was formulated by Paul Dodd [Dod89] as an AlGaAs/GaAs HBT simulation tool. This work describes the extension of this program to the silicon and $Si_{1-x}Ge_x$ material systems. The computer model allows the user to explore internal device physics as well as terminal characteristics of a device. Field-dependent mobility has been added to the program in order to more accurately compute high-field transport phenomena. The simulation tool is used to study the performance of silicon bipolar transistors and Si/SiGe HBT's, and these results are presented in chapter 4.

CHAPTER 1: INTRODUCTION

1.1. Fundamentals of HBT Operation

The idea of a bipolar transistor with a wide-gap emitter is almost as old as the bipolar junction transistor (BJT). In fact, Schockley described the idea in his application for a patent on the junction bipolar transistor [Sho48]. The performance advantages of this type of device, commonly known as the heterojunction bipolar transistor (HBT), have been known for many years. Kroemer first explained the underlying central principle of the HBT as "the use of energy gap variations beside electric fields to control the forces acting on electrons and holes, separately and independently of each other" [Kro57].

Although the performance advantages of HBT's over BJT's were well understood, no fabrication technologies were available to produce high quality heterojunctions until the 1970's. The emergence of two new growth techniques, molecular beam epitaxy (MBE) [Cho75] and metal organic chemical vapor deposition (MOCVD) [Dup79], sparked a thrust in the research of high speed HBT's. Most research has been on the AlGaAs/GaAs system, but many other compound semiconductor heterojunctions have been explored as well.

Despite recent advances in HBT fabrication techniques, silicon devices continue to dominate in today's high-technology fabrication facilities. This is mainly due to the low cost and ease of manufacturability of silicon. Silicon readily forms a high quality oxide which can be used to mask implants, diffusion, and metallization. GaAs and the other III-V semiconductors lack this important property. However, silicon BJT's are reaching their fundamental limits on speed because of physical properties of the semiconductor. High-speed devices will require HBT technology. The highest f_T on record for a silicon BJT is 44 GHz [Sug89]. In comparison, AlGaAs/GaAs HBT's have achieved f_T's of over 170 GHz [Ish90] and have cracked the 200 GHz barrier for maximum frequency of oscillation [Mor90]. A

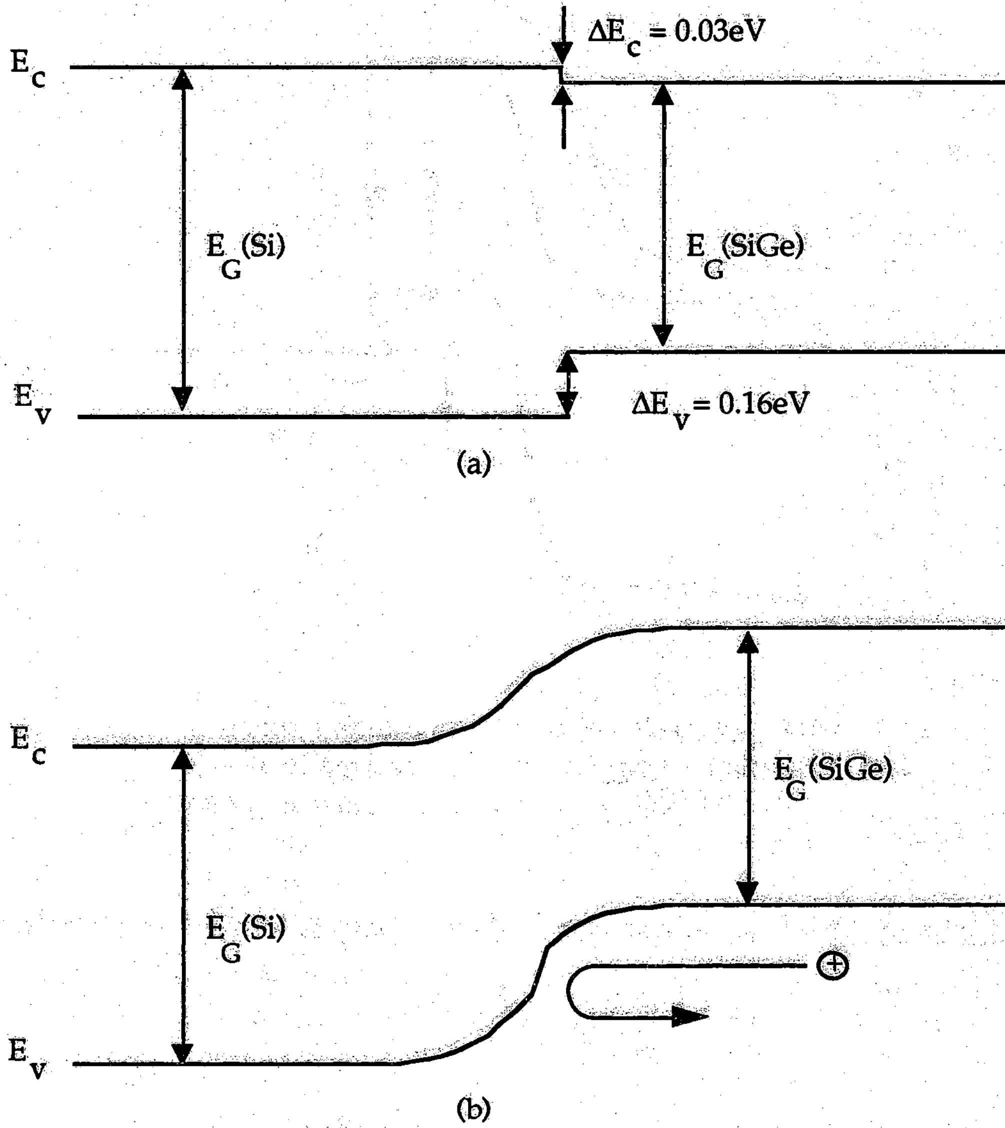

Figure 1.1 np $Si/Si_{0.85}Ge_{0.15}$ heterojunction band diagram. (a) mobile charge has been fixed. (b) carriers are free to cross the junction.

fundamental question arises: Can the performance advantages of an HBT be realized in a cost effective process technology which will enable them to be mass produced? The answer to this question is probably yes, although it may take several years to develop. SiGe HBT's have many of the processing advantages of silicon BJT's, yet they have considerably better high frequency characteristics. A 75 GHz SiGe HBT has already been reported in this relatively new technology [Pat90].

The fundamental design feature of an HBT is the use of a wide bandgap semiconductor in the emitter compared to that of the base. Figure 1.1a shows an idealized $Si/Si_{0.85}Ge_{0.15}$ np heterojunction in which the mobile carriers have been fixed. This heterojunction is representative of the emitter-base junction in a SiGe HBT. Minority carrier electrons are readily injected into the base. However, hole back-injection into the collector is suppressed by the valence band discontinuity since it is on the order of several kT. When the mobile carriers are free to cross the junction, no appreciable conduction band discontinuity or conduction band spiking is observed (figure 1.1b). Conduction band spikes act as a barrier to electron injection into the base, but the discontinuity can be significantly reduced by grading the emitter-base junction.

Some of the advantages of the HBT can be illustrated by analyzing the current components in an npn HBT. Figure 1.2 shows an energy band diagram of an npn HBT in the forward active mode of operation. The following are the major dc current components flowing in the transistor [Kro82]: I_n is the electron current injected from the emitter into the base; a hole current, I_p, is injected from the base back into the emitter; electron-hole recombination in the forward biased emitter-base space charge layer produces a current I_s; and I_r is the current due to injected electrons recombining with holes in the quasi-neutral base. Current components I_p, I_r, and I_s should be minimized in order to maximize device performance. The terminal currents can be expressed in terms of these 4 components:

$$I_e = I_n + I_p + I_s \ , \tag{1.1}$$

$$I_b = I_p + I_r + I_s \ , \tag{1.2}$$

$$I_c = I_n - I_r \, . \tag{1.3}$$

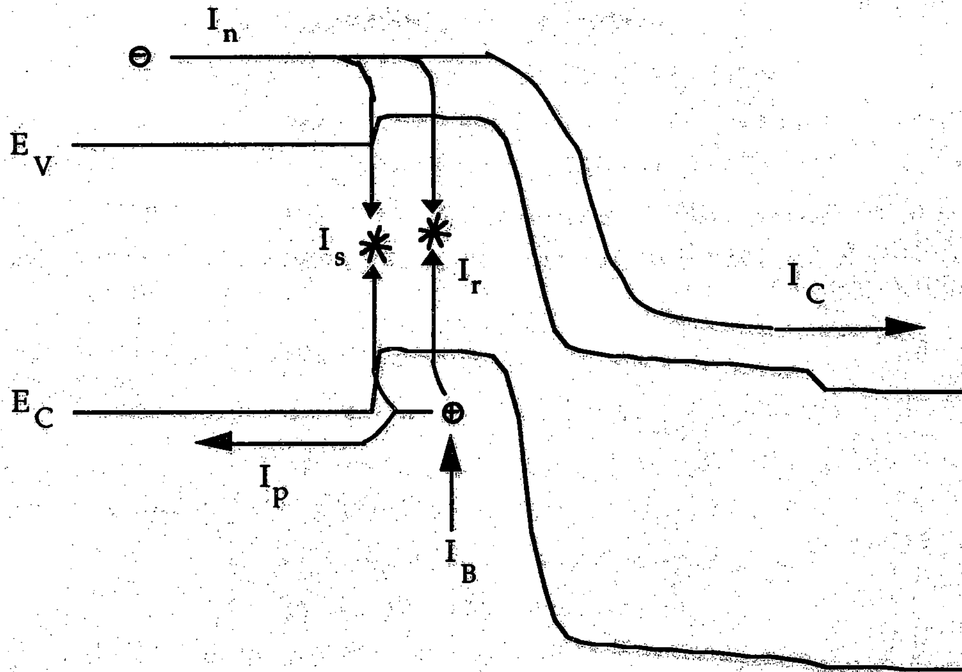

Figure 1.2 Current components in a $Si/Si_{0.8}Ge_{0.2}$ HBT in forward active mode of operation. The relative conduction and valence band energies were calculated by PUPHS2D.

An important figure of merit for bipolar transistors is the dc current gain:

$$\beta = \frac{I_B}{I_C} = \frac{I_n - I_r}{I_p + I_r + I_s} < \frac{I_n}{I_p} \equiv \beta_{max}. \tag{1.4}$$

By definition, β_{max} is the value of current gain for which the recombination currents I_r and I_s are negligible. This is guaranteed to be the highest possible current gain since the recombination currents are positive by convention. The electron and hole injection currents in a forward biased pn junction can be expressed as [Neu83]:

$$I_n = J_n A = \frac{q\, A\, D_{nB}}{L_{nB}}\; n_{p0}\; (\exp\{\frac{qV_{BE}}{kT}\} - 1) \tag{1.5}$$

$$I_p = J_pA = \frac{q\,A\,D_{pE}}{L_{pE}}\ p_{n0}\ (\exp\{\frac{qV_{BE}}{kT}\} - 1), \tag{1.6}$$

where V_{BE} is the applied bias, A is the area of the junction, D_{nB} and D_{pE} are the minority carrier diffusion constants, L_{nB} and L_{pE} are minority carrier diffusion lengths, and n_{p0} and p_{n0} are the equilibrium minority carrier concentrations in the neutral base and emitter. The following substitutions can be made in equations 1.5 and 1.6:

$$n_{p0} = \frac{n_{iE}^2}{N_{DE}} \tag{1.7}$$

$$p_{n0} = \frac{n_{iB}^2}{N_{AB}} \tag{1.8}$$

$$n_{iB}^2 = n_{iE}^2\ \exp\{\frac{\Delta E_G}{kT}\}. \tag{1.9}$$

A bandgap narrowing formulation has been used to relate the intrinsic carrier concentrations in the base and emitter [Lun81]. The current gain expression becomes:

$$\beta = \frac{N_{DE}\ L_{pE}\ D_{nB}}{N_{AB}\ L_{nB}\ D_{pE}}\ \exp\{\frac{\Delta E_G}{kT}\}. \tag{1.10}$$

Assuming

$$\frac{L_{pE}D_{nB}}{L_{nB}D_{pE}} \approx 1, \tag{1.11}$$

the current gain simplifies to

$$\beta \approx \frac{N_{DE}}{N_{AB}}\ \exp\{\frac{\Delta E_G}{kT}\}. \tag{1.12}$$

In homojunction transistors, the current gain reduces to the ratio of emitter to base doping. For a typical gain of 100, the emitter must be doped 100 times as heavily as the base. In HBT's the exponential term in equation 1.12 contributes significantly to the current gain if the bandgap difference is more than a few kT. A consequence is the base in an HBT can be more heavily

doped than in a BJT, and the HBT can achieve a higher current gain than a BJT with a lighter base doping. Better high frequency performance of HBT's over BJT's is a result of heavier base doping since the base resistance and parasitic junction capacitances are reduced. As device dimensions continue to shrink in an effort to increase f_T, heavier base dopings are required to reduce the base width and base resistance. Base resistance is an important parameter in determining f_{max}, the maximum frequency of oscillation.

1.2. Overview of SiGe Technology

The study of SiGe structures began shortly after the initial development of the bipolar transistor. Motivation for development of SiGe devices was the potential to improve device performance by utilizing heterostructures. $Si_{1-x}Ge_x$ alloys have smaller bandgaps than silicon which makes them suitable for the base material in Si/SiGe HBT's. Silicon and germanium are completely miscible over the entire compositional range and give rise to alloys with a diamond crystal structure. However, silicon and germanium have different lattice constants. At room temperature, the lattice constants for silicon and germanium are 5.43Å and 5.65Å respectively (see figure 1.3), a 4.17 percent mismatch [Man82]. The lattice constant of $Si_{1-x}Ge_x$ alloys varies linearly, obeying Vegard's rule

$$a(Si_{1-x}Ge_x) = a_{Si} + x(a_{Ge} - a_{Si}), \tag{1.13}$$

for low fractions of germanium concentration. Due to the relatively large lattice mismatch between SiGe and silicon, commensurate (defect free) SiGe alloy films cannot be grown on silicon substrates without introducing large amounts of strain. Methods were not available to grow high quality strained layers until the early 1980's, and consequently bulk crystal growth was the method of choice in the first studies of SiGe alloys. Band structure data was obtained by cyclotron resonance [Dre55,Fin76]. Compositional dependence of the bandgap of bulk $Si_{1-x}Ge_x$ alloys was investigated by Braunstein [Bra58]. Transport properties of SiGe films were reported as well [Hel76,Med76]. Stress was applied to these samples externally in an effort to study the effects of strain. These studies were instrumental in determining the nature of electronic bandstructures in SiGe alloys. The first SiGe devices to be

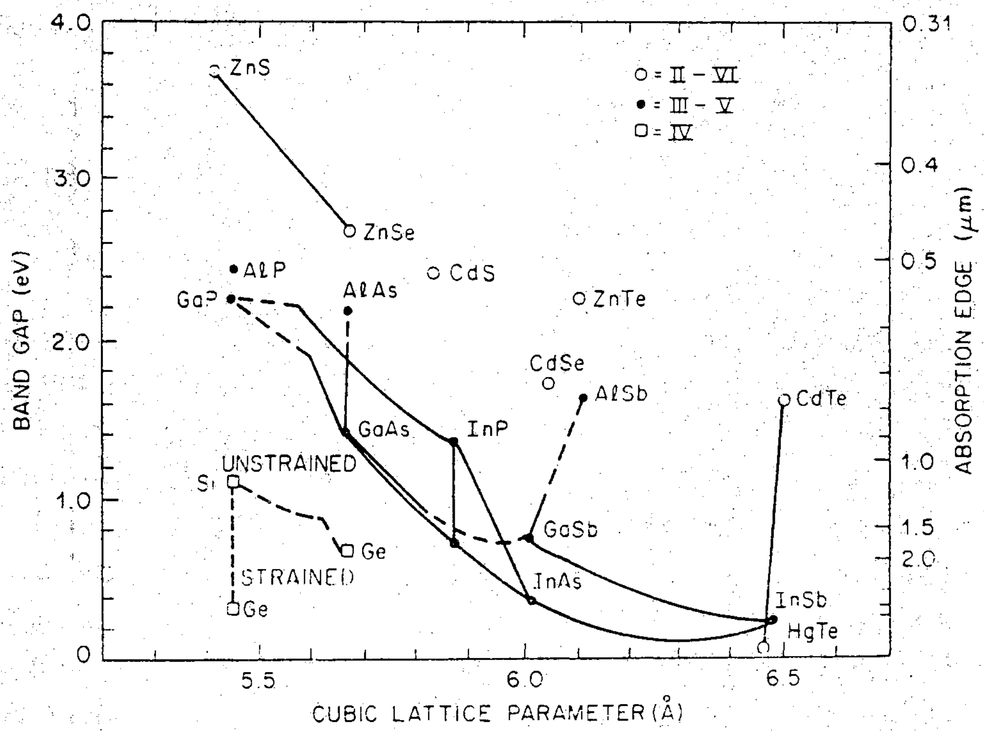

Figure 1.3 Energy bandgap and lattice constant of various semiconductor systems. Figure reprinted from [Pea89].

investigated were amorphous structures in which the presence of misfit dislocations was not important. Until the 1980's, most of the literature on SiGe alloys concentrated on the characterization and development of these materials as amorphous semiconductors.

New growth techniques such as MBE emerged in the early 1980's which enabled the growth of strained SiGe thin films on silicon and germanium substrates. Lattice matched heterostructures can be grown without misfit dislocation defects if the strained layers are grown sufficiently thin. Mismatch is accommodated by uniform lattice strain. Lattice constants of the strained layer parallel to the interface adjust such that the two materials have perfectly matching lattice constants. Strain is compensated by a change in lattice constant perpendicular to the interface which minimizes the elastic energy. Figure 1.4 is a two-dimensional representation of growth of a SiGe film on a Si (100) substrate. Either of two cases may arise: (b) the growth is pseudomorphic with biaxial in-plane compression of the SiGe and extension

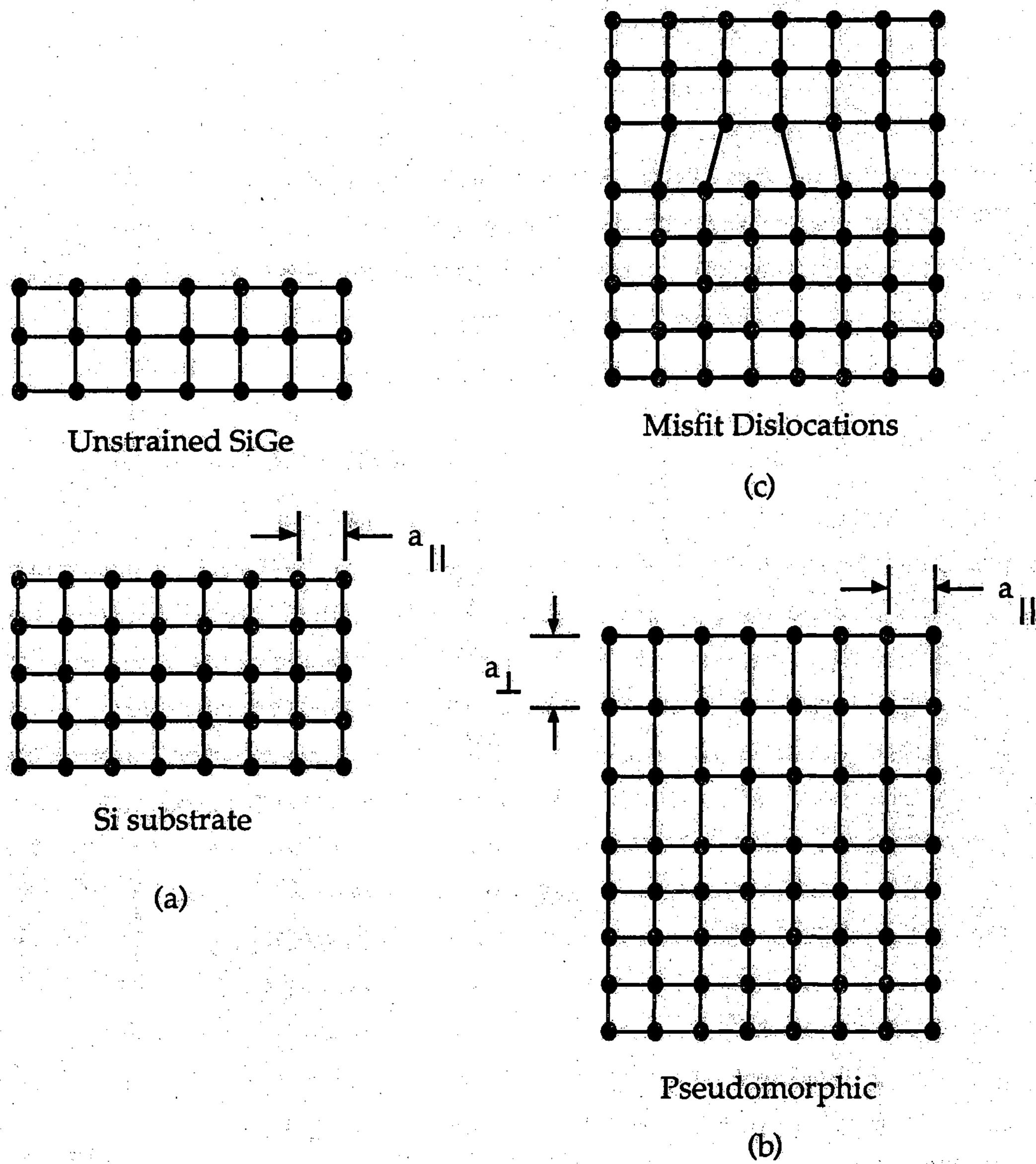

Figure 1.4 Two-dimensional representation of SiGe growth on a Si (100) substrate. (a) unstrained SiGe is grown on a Si substrate. (b) growth is pseudomorphic. (c) growth is non-pseudomorphic.

normal to the interface, or (c) misfit dislocations form at the interface. Misfit dislocations are undesirable as they form efficient recombination-generation centers which degrade device performance and introduce noise. Misfit dislocation generation can be caused by improper growth conditions or strained layer thickness exceeding the critical thickness. For a given Ge mole fraction, there is a critical thickness of the SiGe layer above which dislocations form at the interface. Misfit is accommodated by elastic strain when the film thickness is less than the critical thickness. Misfit is accommodated by both elastic strain and dislocations if the film exceeds the critical thickness. Figure 1.5 shows experimental and theoretical critical thickness data for $Si_{1-x}Ge_x$ alloys grown on Si (100) substrates [Peo86]. Larger germanium mole fractions create more lattice mismatch and hence more strain. Experimental values are from Bean [Peo85] which agree with People's results obtained using energy balance and the self-energy concept for an isolated dislocation [Peo86]. The findings of People and Bean show critical thickness is underestimated using mechanical equilibrium theory [Mat74].

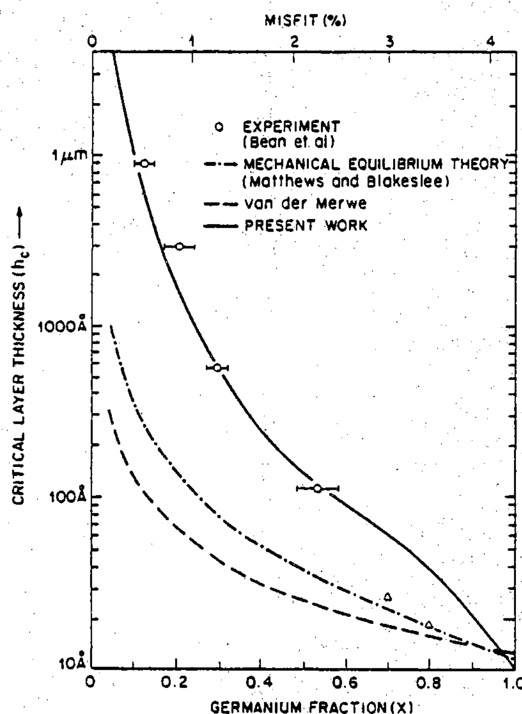

Figure 1.5 Critical thickness of $Si_{1-x}Ge_x$ alloys grown on Si (100) substrates. Figure reprinted from [Peo86].

The electronic properties of SiGe materials depend on the substrate material on which they are grown, the germanium mole fraction in the film, and the quality of the film and interface. PUPHS2D, the computer model on which this thesis is based, assumes devices are of very good quality (negligible number of misfit dislocations and SiGe film thickness does not exceed the critical thickness). The user must beware! Although SiGe can be grown on silicon, germanium or even SiGe substrates, the fabrication of Si/SiGe HBT's requires SiGe growth on silicon substrates. Therefore, the SiGe material models in PUPHS2D assume coherently strained SiGe films are grown on Si (100) substrates.

1.3. History of SiGe HBT's

First generation $Si/Si_{1-x}Ge_x$ heterojunction bipolar transistors were fabricated during 1987-1988 using molecular beam epitaxy by IBM, AT&T and NEC [Pat88,Tem88,Tat88]. These transistors were grown on Si (100) substrates with a constant germanium mole fraction in the base. Processing involved low temperature growth conditions in all of these devices. Low temperature growth of the SiGe base is necessary to deter non-pseudomorphic growth and islanding (three dimensional growth) [Iye89]. The transistor from AT&T utilized a $Si_{0.5}Ge_{0.5}/Si$ superlattice in the base to make it thicker than a pure $Si_{0.5}Ge_{0.5}$ base. This device is an efficient phototransistor. The IBM group fabricated a mesa-etched SiGe base HBT in a process which never exceeds 550° C. The NEC group produced some interesting results. The MBE growth temperature was higher than the other groups (700°C), and the base thickness was 3000Å. The germanium concentration (x) in the base of these samples was constant, and samples were made with x ranging from 10-40%. Their growth temperature is higher than the optimum growth temperature of alloys with more than 10% Ge as shown by Bean *et al.* [Bea84] In addition, 3000Å is the approximate critical thickness of $Si_{0.8}Ge_{0.2}$ grown on Si (100). Misfit dislocations were reported for samples in which x>0.10, and the defect density increased with increasing x. Each of these three groups reported current gains on the order of 10.

Second generation Si/SiGe HBT's were fabricated by chemical vapor deposition (CVD) techniques. CVD has several advantages over MBE. Low

defect density, high purity, flexibility of doping, and throughput capabilities of CVD make these techniques attractive for HBT fabrication. The first reported CVD SiGe HBT's were fabricated using a rapid thermal CVD technique called limited reaction processing (LRP) to grow each layer [Kin89]. LRP relies on rapid changes in substrate temperature to achieve abrupt doping and compositional profiles. High current gains were observed (≈ 400) in $Si_{0.69}Ge_{0.31}$ transistors with 20nm bases and inverted doping profiles (base doping higher than emitter doping).

A low-temperature epitaxial technique called ultra-high-vacuum/chemical vapor deposition (UHV/CVD) has been used to grow graded-base $Si_{1-x}Ge_x$ HBT's [Pat89]. The 75nm SiGe base was graded from 0 to 14% Ge, introducing a built-in drift field of 15kV/cm which reduces the base transit time for electrons. Excellent electrical characteristics were reported for both silicon and SiGe HBT's fabricated using this technique. Current gains as high as 1600 were reported for SiGe HBT's at liquid nitrogen temperature.

Vertical dimensions of SiGe HBT's will continue to shrink in the future. Processing technologies for these devices will utilize many of the same steps as silicon devices, making them more attractive in microwave applications. Low temperature operation of SiGe HBT's is believed to be excellent, as shown by theoretical studies of f_T and f_{max} [Kar90].

1.4. Research Objectives and Thesis Overview

The main objective of this work is to extend the AlGaAs/GaAs HBT simulation program PUPHS2D into an accurate tool for simulation of Si/SiGe HBT's. In addition to SiGe HBT's, the program can simulate silicon BJT's. Chapter 2 discusses the silicon and SiGe material parameters used in the program. Computer model development and field-dependent mobility are discussed in chapter 3. Other research objectives are to assess the computer model accuracy (chapter 3); to assess Si/SiGe HBT performance for microwave applications and compare this to scaled silicon bipolar technology (chapter 4); and finally to examine various HBT design options such as compositionally graded bases (also chapter 4). Chapter 5 presents concluding comments and suggestions for model improvements.

CHAPTER 2: MATERIAL PARAMETERS

2.1. Introduction

PUPHS2D material parameters for both silicon and coherently strained $Si_{1-x}Ge_x$ alloys on Si (100) substrates are presented in this chapter. While silicon has been well-characterized over the past 40 years, not nearly as much is known about strained SiGe. Many simplifying assumptions are made in the SiGe material parameters. Silicon models will simply be presented and referenced. SiGe material parameters will be explained in detail, and the last section in this chapter includes an approach for modelling complex strain-induced effects.

2.2. Bandgap and Bandgap Narrowing

Polynomial fits by Bludau [Blu74] describe the temperature dependence of energy bandgap of pure silicon at or below room temperature (2.1 and 2.2). The high-temperature model is from Sze [Sze81] and is slightly modified to match the room temperature value given by (2.2).

$$E_g(T) = 1.170 + 1.059\times10^{-5}T - 6.05\times10^{-7}T^2 \qquad 0\leq T\leq 170°K \tag{2.1}$$

$$E_g(T) = 1.1785 - 9.025\times10^{-5}T - 3.05\times10^{-7}T^2 \qquad 170\leq T\leq 300°K \tag{2.2}$$

$$E_g(T) = 1.170 - \frac{4.73\times10^{-4}\,T^2}{T + 624.93} \qquad T>300°K \tag{2.3}$$

The bandgap of strained $Si_{1-x}Ge_x$ alloys on Si (100) substrates is given by:

$$E_g(x) = 1.124 - 1.22x + 0.88x^2 \qquad x\leq 0.6 \tag{2.4}$$

$$E_g(x) = \left[1.5 - 2.5E_g(0.6)\right]x + 2.5E_g(0.6) - 0.9 \qquad x>0.6 \tag{2.5}$$

These equations represent a fit to the data by People [Peo86] which is shown in figure 2.1. A linear fit is used for $0.6<x<1.0$ which assumes the bandgap of

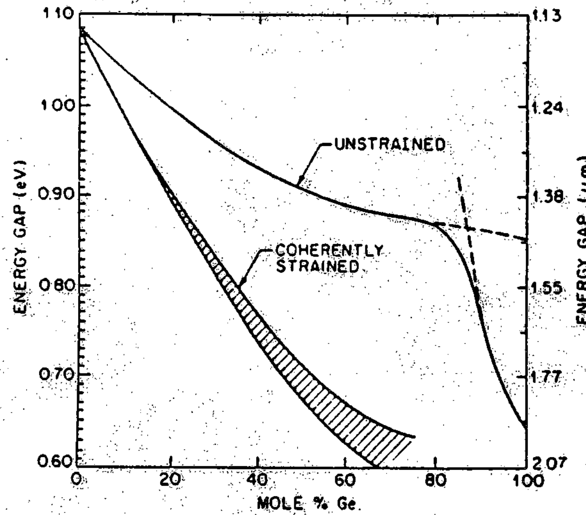

Figure 2.1 Electronic bandgap of strained and unstrained $Si_{1-x}Ge_x$ alloys. Figure reprinted from [Peo86].

strained pure Ge on Si (100) is 0.6 eV. Also shown in figure 2.1 is the bandgap of unstrained $Si_{1-x}Ge_x$ calculated by Braunstein et al. [Bra58]. In the unstrained case, the compositional dependence is weak for x<0.85 where the [100] minima determine the band edge. For x>0.85 the [111] minima are lower in energy and the dependence of bandgap on composition is strong. Note the bandgap of strained SiGe is considerably smaller than that of bulk SiGe. Temperature dependence of bandgap for strained SiGe is assumed to be the same as silicon:

$$E_{gSiGe}(T) = E_{gSiGe}(300K) \times \frac{E_{gSi}(T)}{E_{gSi}(300K)}. \tag{2.6}$$

The effects of heavy doping in both n and p-type silicon can be modelled as an effective shrinkage of the bandgap [Slo76]:

$$\Delta E_g = V_1 \left[\ln\left(\frac{N}{N_0}\right) + \sqrt{\left(\ln\left(\frac{N}{N_0}\right)\right)^2 + C} \right], \tag{2.7}$$

where C=0.5, V_1=9meV, $N_0=10^{17}$ cm^{-3} for p-type silicon [Slo76] and $N_0=1.5\times10^{17}$ cm^{-3} for n-type silicon [Wie80]. No temperature dependence of

bandgap narrowing is assumed since it is believed to be relatively insensitive to temperature [Neu89]. First order effects of heavy doping on the bandgap in strained SiGe have been calculated by Poortmans [Poo89] and Jain [Jai89], however in PUPHS2D bandgap narrowing is assumed to be the same in strained SiGe as in silicon.

2.3. Density of States

The effective conduction and valence band density of states in silicon are given by the well known expressions:

$$N_c = 2M_c\left(\frac{2\Pi m_n^* kT}{h^2}\right)^{3/2} \tag{2.8}$$

$$N_v = 2\left(\frac{2\Pi m_p^* kT}{h^2}\right)^{3/2}, \tag{2.9}$$

where h is Plank's constant, m_n^* and m_p^* are the electron and hole density of states effective masses and M_c=6, the number of equivalent minima in the conduction band. In the conduction band of strained $Si_{1-x}Ge_x$, the bands are "silicon like". The degeneracy of the conduction band is split, and four ellipsoids are shifted down in energy while two are shifted up in energy (see figure 2.2). The effective density of states in the conduction band of strained SiGe can be modelled using an expression equivalent to that of a two-valley system [Sut77]:

$$N_c = 2\left(\frac{2\Pi m_n^* kT}{h^2}\right)^{3/2}\left[M_{c1} + M_{c2}e^{(E_{c1}-E_{c2})/kT}\right], \tag{2.10}$$

where M_{c1} and M_{c2} are the number of valleys shifted down and up in energy. In the case of strained SiGe, M_{c1}=4 and M_{c2}=2. The energy difference between the two sets of valleys is given by E_{c1}-E_{c2} = -0.6x eV [Pej89]. Strain effects are much more complicated in the valence band. The heavy and light hole bands are split, and the nearly spherical constant energy surfaces are distorted into ellipsoids resulting in a highly anisotropic effective mass tensor [Has63]. Assuming light holes do not contribute significantly more to the total number of holes compared to the unstrained case, the silicon valence band density of states can be used for SiGe, independent of strain.

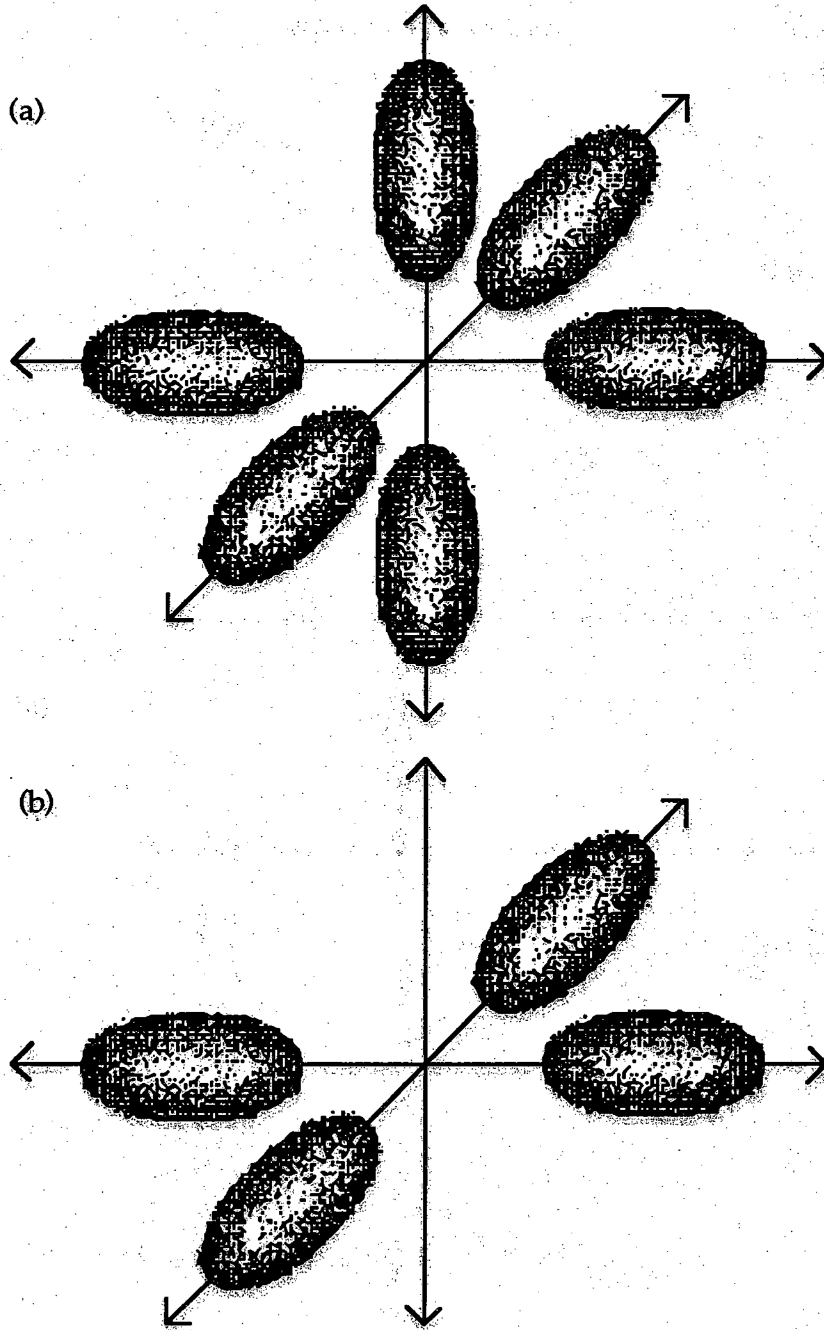

Figure 2.2 Conduction band minima constant energy surfaces for (a) Si, and (b) strained SiGe.

The temperature-dependent effective masses for holes and electrons in lightly doped silicon are given by [Jae80]:

$$m_n^* = 1.045 + 4.5\text{x}10^{-4}T \tag{2.11}$$

$$m_p^* = 0.523 + 1.40\text{x}10^{-3}T - 1.48\text{x}10^{-6}T^2. \tag{2.12}$$

These are polynomial fits to the data by Barber [Bar67]. Equation 2.11 takes into account all six equivalent ellipsoids in silicon and must be modified for use in equations 2.8 and 2.10 by dividing by $6^{2/3}$:

$$m_n^* = 0.3165 + 1.36\text{x}10^{-4}T. \tag{2.13}$$

Equation 2.12 is valid for both silicon and strained SiGe according to the assumptions made earlier.

The intrinsic carrier concentration in an arbitrary semiconductor is

$$n_i = \sqrt{N_c N_v}\, \exp\left(\frac{-E_g}{2kT}\right). \tag{2.14}$$

Figure 2.3 is a graph of n_i versus 1000/T for silicon and three strained $Si_{1-x}Ge_x$ alloys. The value of n_i at 300K predicted by the model is $8.7\text{x}10^9$, which agrees fairly well with the experimental value. n_i is much larger in SiGe than in silicon since the bandgap of SiGe is several kT smaller. A result is better injection properties of the emitter-base junction for Si/SiGe HBT's compared to silicon homojunctions which was shown in chapter 1.

2.4. Dielectric Constant and Electron Affinity

2.4.1. Dielectric Constant

The static dielectric constants of silicon and germanium are 11.8 and 16.0 respectively [Sze81]. Composition-dependent static dielectric constant of SiGe alloys is given by the expression [Sut77]:

$$\varepsilon = \frac{1 + 2[x\cdot f_{Ge} + (1-x)\cdot f_{Si}]}{1 - x\cdot f_{Ge} - (1-x)\cdot f_{Si}} \tag{2.15}$$

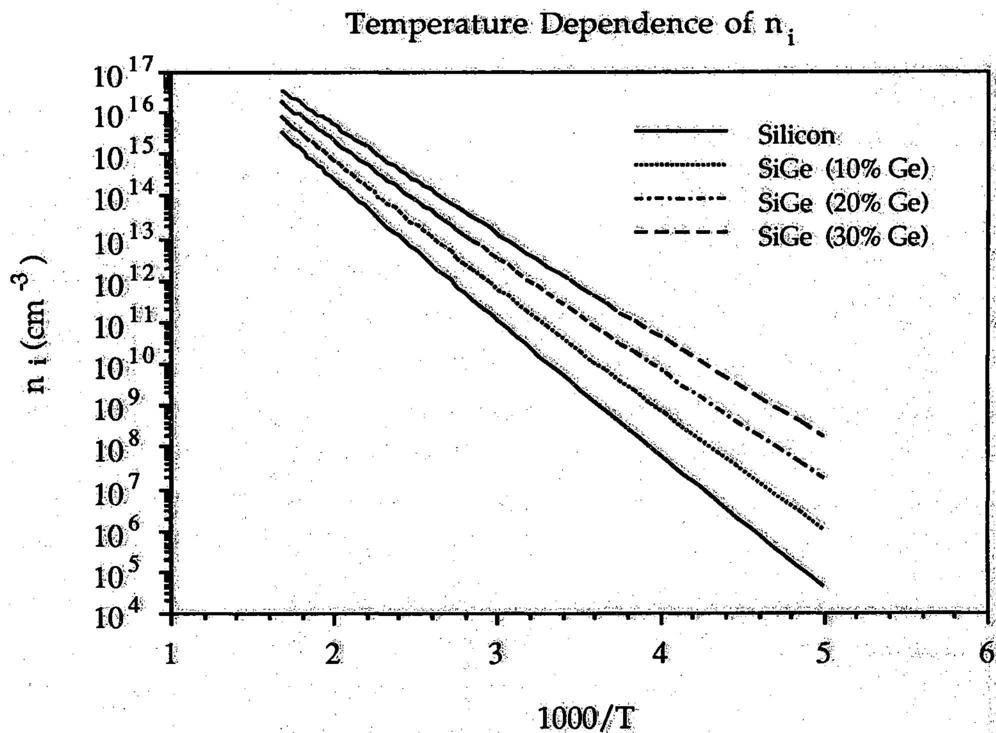

Figure 2.3 Intrinsic concentration vs. 1000/T for Si and three SiGe alloys.

where

$$f_{Si} = \frac{\varepsilon_{Si} - 1}{\varepsilon_{Si+2}} \tag{2.16}$$

and

$$f_{Ge} = \frac{\varepsilon_{Ge} - 1}{\varepsilon_{Ge+2}}. \tag{2.17}$$

No strain dependence is assumed for the dielectric constant.

2.4.2. Electron Affinity

The electron affinity of silicon is 4.05 [Sze81]. The electron affinity of $Si_{1-x}Ge_x$ alloys satisfies the Dingle Rule [Din74]:

$$\chi_{SiGe} = \chi_{Si} - DECFRC^*(E_{gx} - E_{gSi}) + (E_{gx} - E_{gSiGe}), \tag{2.18}$$

where E_{gx} is the X valley bandgap of SiGe and DECFRC is defined in (2.19).

$$\Delta E_c = DECFRC*\Delta E_g \tag{2.19}$$

In equation 2.19, ΔE_g is the bandgap difference between silicon and SiGe. DECFRC is a very important PUPHS2D user-specified variable. DECFRC is on the order of 0.1-0.2 for SiGe alloys (default is 0.15), depending on the germanium mole fraction. The Dingle Rule applies to the X valley, and this value of χ is valid for Ge mole fractions less than 0.85.

2.5. Bulk Recombination and Carrier Lifetimes

The dominant recombination processes in bulk silicon are Shockley-Read-Hall (R-G center) and Auger recombination. Radiative recombination is negligible since silicon is an indirect bandgap semiconductor, and recombination involving excitons and shallow-level traps is only important at low temperatures. The total recombination rate due to radiative, Auger, and Shockley-Read-Hall (SRH) recombination can be written as:

$$R = \left[B_r + A_n n + A_p p + \frac{1}{\tau_n(p+p_1) + \tau_p(n+n_1)}\right](np - n_{ie}^2). \tag{2.20}$$

In (2.20), B_r is the radiative recombination coefficient, A_n and A_p are the electron and hole Auger recombination coefficients and n_{ie} is the effective intrinsic carrier concentration including bandgap narrowing effects. τ_n and τ_p are the minority carrier SRH lifetimes and n_1 and p_1 are constants which depend on the energy of the deep-level traps. Default values for the radiative and Auger recombination coefficients are B_r=0, A_n=5.0x10^{-32} and A_p=9.9x10^{-32} for silicon [Dzi77]. The default trap energy level is the intrinsic level, E_i. Since strained SiGe is similar to silicon in bandstructure, exactly the same recombination model is assumed for SiGe.

The minority carrier lifetimes in silicon are doping dependent. For doping concentrations up to 10^{19} cm^{-3} an empirical fit to experimental data gives

$$\tau(N) = \frac{\tau(0)}{1 + \frac{N}{N_0}} \tag{2.21}$$

for both electrons and holes. $\tau(0)$ is the minority carrier lifetime in lightly doped silicon and N_0 is the reference doping. A good fit to experimental data is achieved by setting $N_0 = 7.1\times10^{17}$ cm^{-3} for both n and p-type silicon, $\tau(0)=3.95\times10^{-4}$ seconds for holes and $\tau(0)=1.70\times10^{-5}$ seconds for electrons [Fos76]. However, $\tau(0)$ is very process-dependent, and $\tau(0)$ values given by Foster may not be accurate in all cases. Default values for the SRH lifetimes are 1μsec for both electrons and holes. The default reference doping is 5×10^{50} cm^{-3} which effectively removes the doping dependence.

Studies on the determination of minority carrier lifetimes in SiGe have been reported [Joh89], however the SiGe samples contained misfit dislocations. The measured SiGe lifetimes in this study were in the sub-nanosecond range which is extremely small and is due to the large number of misfit dislocations. Minority carrier lifetimes in SiGe are believed to be somewhat shorter than silicon minority carrier lifetimes. Until more studies are done on this subject, 0.1μsec lifetimes will be assumed in n and p-type SiGe, independent of doping.

2.6. Carrier Mobilities

Carrier mobilities in semiconductors are determined by a variety of physical mechanisms. Electrons and holes are scattered by thermal lattice vibrations, ionized impurities, neutral impurities, dislocations, and electrons and holes themselves. A further reduction in mobility is due to saturation of the drift velocity of warm and hot carriers. This subject is treated in chapter 3, and the mobility models presented in this section are assumed to be valid for low electric fields. Ionized impurity scattering and phonon scattering are the two dominant mechanisms in silicon devices. Neutral impurity scattering becomes important for temperatures less than about 77 K, since nearly all the impurities are ionized above this temperature. Scattering by dislocations and carrier-carrier scattering are assumed to be negligible in the ensuing discussion. Many models for silicon carrier mobilities have been proposed over the past 25 years. There are two low-field silicon mobility models

available in PUPHS2D from which the user can choose. Mobilities for SiGe are complicated by alloy scattering and anisotropy.

2.6.1. Silicon Mobility

One of the most widely used doping dependent mobility models was developed by Caughy and Thomas [Cau67] and is valid for both electrons and holes. PUPHS2D uses this expression in one of the two total mobility models for silicon. However, for electrons, the constants are taken from [Bac75], and for holes the constants of Plunkett and Stone [Plu77] are used. Temperature dependence of the lattice component is from [Jac77] and temperature dependence for the impurity scattering component is from Sze [Sze81]. Lattice and impurity scattering limited mobilities are combined using Matthiessen's rule. The equations below are valid for holes and electrons.

$$\mu_l = \mu_{max}\left(\frac{T}{300}\right)^{\eta} \tag{2.22}$$

$$\mu_{imp} = \frac{\mu_{max}}{\mu_{max} - \mu_{min}}\left[\left(\frac{N_{ref}}{N}\right)^{\alpha}\mu_{max} + \mu_{min}\right]\left(\frac{T}{300}\right)^{\gamma} \tag{2.23}$$

$$\mu = \left(\frac{1}{\mu_l} + \frac{1}{\mu_{imp}}\right)^{-1} \tag{2.24}$$

N is the doping density, and other constants are given in table 2.1. Both majority and minority mobility are given by (2.24).

The other PUPHS2D model (see Arora [Aro82]) is a modified form of the Caughy-Thomas expression and includes both concentration and temperature dependence. Equation (2.25) is valid for both holes and electrons.

$$\mu = \mu_{min}T_n^{\beta_1} + \frac{(\mu_{max} - \mu_{min})T_n^{\beta_2}}{1 + \left[\frac{N}{N_{ref}T_n^{\beta_3}}\right]^{\alpha T_n^{\beta_4}}}, \tag{2.25}$$

where T_n=T/300 is the normalized temperature, N is the total impurity concentration and the constants for holes and electrons are given in table 2.2.

Table 2.1 Caughy-Thomas silicon mobility constants.

parameter	electrons	holes
μ_{max} (cm^2/V-s)	1360	495
μ_{min} (cm^2/V-s)	92	47.7
N_{ref} (cm^{-3})	1.3×10^{17}	1.9×10^{17}
η	-2.42	-2.20
α	0.91	0.76
γ	1.5	1.5

Majority and minority carrier mobilities are given by (2.25). Majority carrier mobility values are within $\pm$13% of the reported experimental values for impurity concentrations up to about 10^{20} cm^{-3} and over a temperature range of 250-500K.

Table 2.2 Arora silicon mobility constants.

parameter	electrons	holes
μ_{max} (cm^2/V-s)	1340	461
μ_{min} (cm^2/V-s)	88	54.3
N_{ref} (cm^{-3})	1.26×10^{17}	2.35×10^{17}
α	.88	.88
β_1	-.57	-.57
β_2	-2.33	-2.23
β_2	2.4	2.4
β_4	-.146	-.146

In (2.24) and (2.25) the majority and minority carrier mobilities are assumed to be equal. These mobilities are also functions of total impurity concentration. Recent works have investigated the physics of heavily doped silicon. Swirhun reported minority carrier mobilities in silicon are about twice as large as majority carrier mobilities [Swi86a,Swi86b]. Scattering by donors is different from that by acceptors because repulsive potentials scatter less than attractive potentials of the same strength. The following model by Shigyo et al. [Shi90] presents carrier mobility as a function of minority and majority concentrations, not total concentration. The model is not available in PUPHS2D but could be easily added (see chapter 3). Majority mobilities are from Masetti [Mas83] and minority mobilities are from Swirhun for holes and electrons. Matthiessen's rule joins $\mu_{minority}$ and $\mu_{majority}$, considering μ_{phonon} is incorporated into both $\mu_{minority}$ and $\mu_{majority}$.

$$\mu_{p,minority}(N_D^+) = 130 + \frac{\mu_{p,phonon} - 130}{1 + \left[\frac{N_D^+}{8\text{x}10^{17}}\right]^{1.25}}, \tag{2.26}$$

$$\mu_{p,majority}(N_A^-) = \frac{\mu_{p,phonon}}{1 + \left[\frac{N_A^-}{2.23\text{x}10^{17}}\right]^{0.719}} + 44.9\exp\left[-\frac{9.23\text{x}10^{16}}{N_A^-}\right] - \frac{29}{1 + \left[\frac{6.1\text{x}10^{20}}{N_A^-}\right]}, \tag{2.27}$$

$$\mu_{p,phonon} = 470.5\ \text{cm}^2/\text{V-s}, \tag{2.28}$$

and

$$\mu_p^{-1}(N_D^+,N_A^-) = \mu^{-1}{}_{p,minority}(N_D^+) + \mu^{-1}{}_{p,majority}(N_A^-) - \mu^{-1}{}_{p,phonon}. \tag{2.29}$$

Similarly for electron mobility:

$$\mu_{n,minority}(N_A^-) = 232 + \frac{\mu_{n,phonon} - 232}{1 + \left[\frac{N_A^-}{8\text{x}10^{16}}\right]^{0.9}}, \tag{2.30}$$

$$\mu_{n,majority}(N_D^+) = 52.2 + \frac{\mu_{n,phonon} - 52.2}{1 + \left[\frac{N_D^+}{9.68\text{x}10^{16}}\right]^{0.68}} - \frac{43.4}{1 + \left[\frac{3.43\text{x}10^{20}}{N_D^+}\right]}, \tag{2.31}$$

$$\mu_{n,phonon} = 1417 \text{ cm}^2/\text{V-s}, \tag{2.32}$$

and

$$\mu_n^{-1}(N_D^+, N_A^-) = \mu^{-1}_{n,minority}(N_A^-) + \mu^{-1}_{n,majority}(N_D^+) - \mu^{-1}_{n,phonon}. \tag{2.33}$$

Note μ_n reduces to $\mu_{n,minority}$ for $N_A^- >> N_D^+$, and $\mu_{n,majority}$ for $N_A^- << N_D^+$ (and similarly for holes). This model gives good results for heavily doped silicon. Bandgap narrowing in heavily doped silicon is smaller than predicted by Slotboom and Degraaff [Slo76] due to the larger minority carrier mobility. For more details the reader is referred to [Shi90] and [Ala87].

Figures 2.4 and 2.5 are graphs of silicon electron and hole mobility versus impurity concentration. Minority carrier mobility is about twice as large as majority carrier mobility in heavily doped material. Majority carrier mobility is very low in heavily doped material, but it is dependent on the dopant species.

2.6.2. $Si_{1-x}Ge_x$ Mobility

There have been few reports on the measurements of mobility in strained $Si_{1-x}Ge_x$ alloys. However, enhanced low-temperature mobilities have been observed for both holes and electrons [Jor85]. Manasevit et al. [Mae82] reported enhanced electron mobilities at room temperature, but the Ge mole fraction of the samples was not accurately known. Monte Carlo simulations of electron mobility in heavily doped SiGe at room temperature indicate μ_n will be almost 50% higher than for silicon due to the smaller effective mass in SiGe [Smi87]. In addition to phonon, impurity, and alloy scattering mechanisms, strain is expected to play a major role in determining carrier mobility. Due to strain effects, mobilities in SiGe are different for carriers travelling parallel and perpendicular to the direction of growth.

A logical approach to modelling mobility in strained SiGe was proposed by Racanelli [Rac89]. Expressions for phonon and impurity scattering limited mobility as functions of conductivity and density of states effective masses are formulated and fitted to measured silicon mobility. Corrections to these mobilities are made by replacing the silicon effective

masses with SiGe effective masses. Alloy scattering mobility is combined with phonon and impurity scattering mobility using Matthiessen's rule to give the total SiGe mobility. This model takes into account the different mobilities parallel and perpendicular to the direction of growth. Very large hole mobilities are predicted by the model, on the order of several thousand $cm^2/V\text{-}s$ in lightly doped SiGe. Electron mobilities are slightly higher than in silicon. While this model addresses many of the strain effects on mobility, many parameters in the formulation have not been verified by experiment.

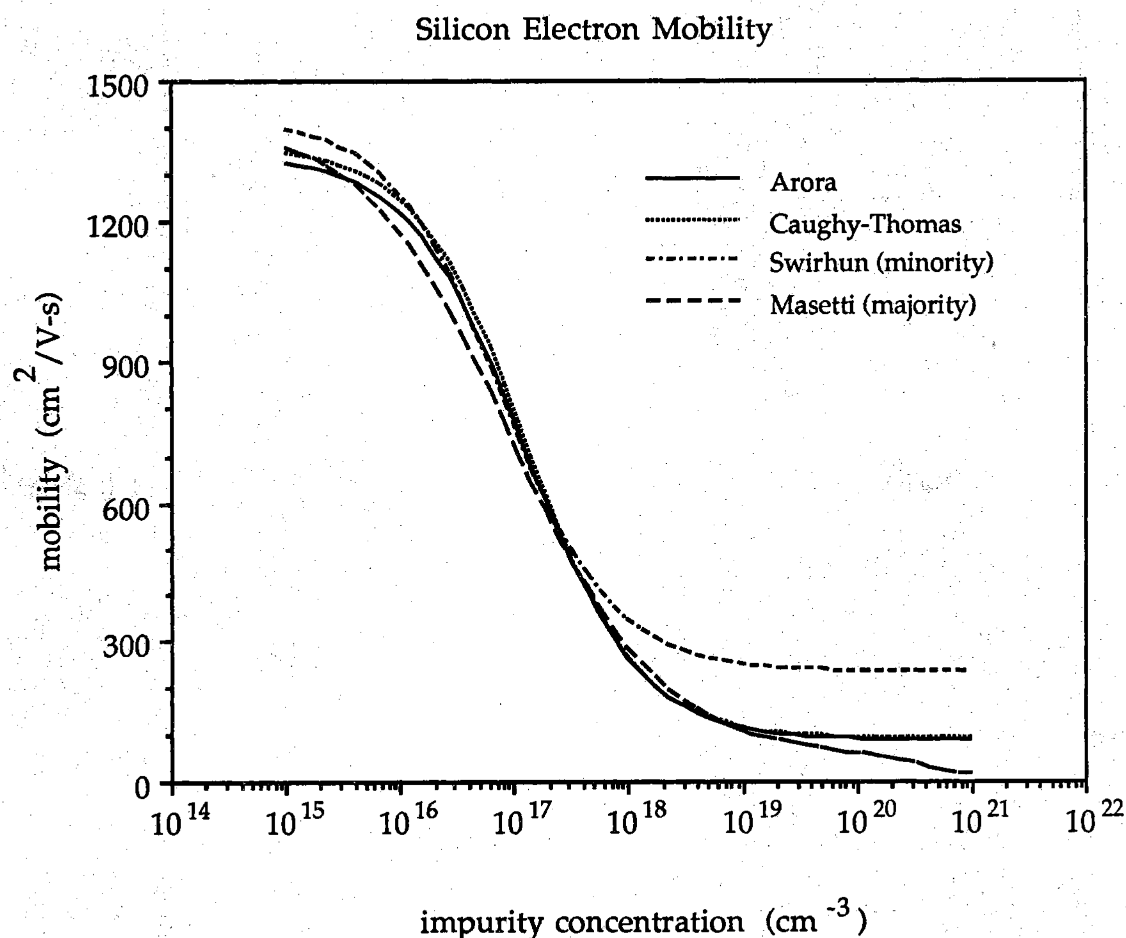

Figure 2.4 Silicon electron mobility versus impurity concentration.

A conservative approach has been taken in the $Si_{1-x}Ge_x$ mobility model used in PUPHS2D. This model will suffice until accurate measurements of carrier mobilities in strained SiGe are published. Impurity and phonon scattering mobilities are assumed to be the same as in silicon. Alloy scattering mobility is combined with impurity and phonon scattering mobilities using Matthiessen's rule as shown in (2.34).

$$\mu_{SiGe} = \left(\frac{1}{\mu_{Si}} + \frac{1}{\mu_{alloy}}\right)^{-1} \tag{2.34}$$

Alloy scattering mobility is taken from Krishnamurthy [Kri85]:

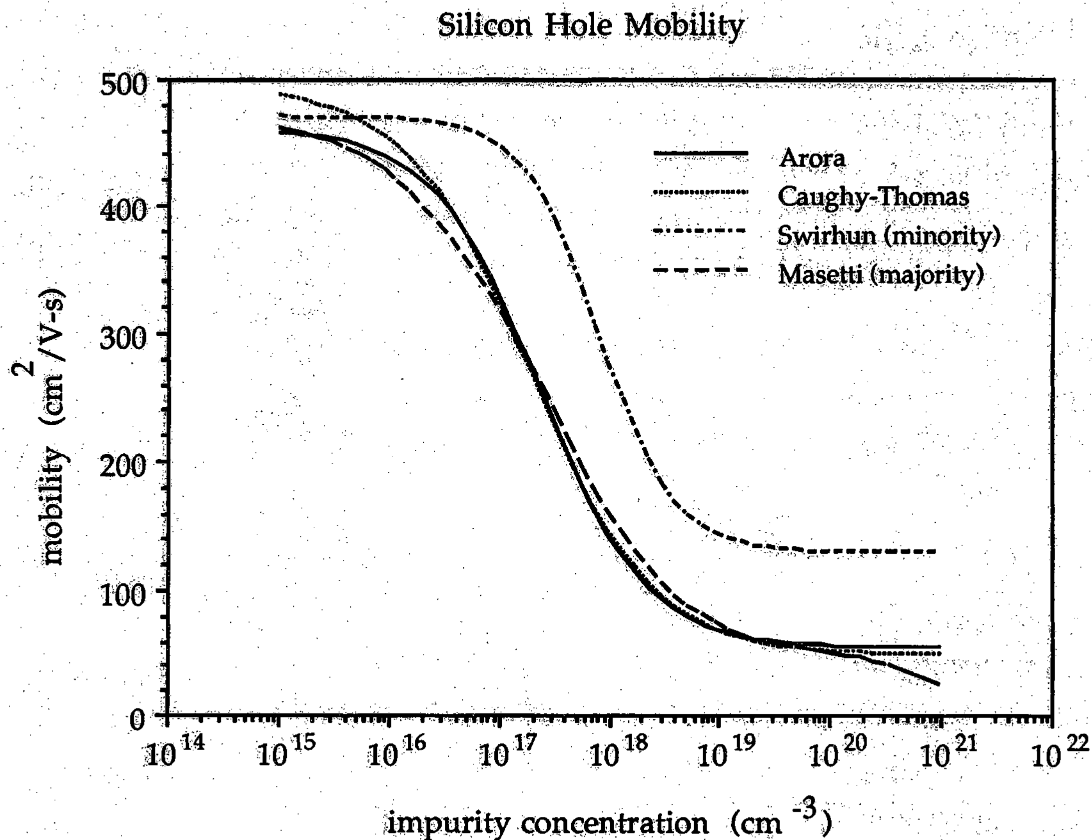

Figure 2.5 Silicon hole mobility versus impurity concentration.

$$\mu_{alloy} = \frac{\sqrt{2\pi}\, q h^4 N}{48\pi^4\, x(1-x)\, m_c^* (m_d^*)^{3/2} (\Delta E)^2 \sqrt{kT}} \quad (2.35)$$

In (2.35), N is the number of atoms per cm^3 in the alloy, x is the Ge mole fraction, m_c^* and m_d^* are the conductivity and density of states effective masses, and ΔE is a material-dependent scattering parameter. In coherently strained $Si_{1-x}Ge_x$ alloys, N can be expressed as:

$$N = \frac{8}{(a_{Si})^2\, a_{SiGe}}, \quad (2.36)$$

where a_{Si} and a_{SiGe} are lattice constants and a_{SiGe} is defined in (1.13). m_d^* was defined for electrons and holes in (2.11) and (2.12) respectively. (2.11) must be redefined for SiGe because there are only four degenerate ellipsoids in the conduction band:

$$m_n^* = 0.7978 + 3.43\text{x}10^{-4}T. \quad (2.37)$$

The conductivity effective masses depend on the direction of travel of the carriers. For electrons,

$$m_{ce}^* = m_t^* \qquad \text{(parallel to growth)} \quad (2.38)$$

$$m_{ce}^* = \left[\frac{1}{2}\left(\frac{1}{m_t^*} + \frac{1}{m_l^*}\right)\right]^{-1} \qquad \text{(perpendicular to growth).} \quad (2.39)$$

where m_t^* and m_l^* are the transverse and longitudinal effective masses of silicon ($.1905m_0$ and $.9163m_0$ respectively). Strain effects in the valence band are more complicated. Hole mobility in strained SiGe is believed to be greater than in silicon, and hole mobility is highest for transport perpendicular to the direction of growth. However, in this conservative approach, hole mobilities are smaller than in silicon, and hole mobilities are assumed to be independent of transport direction.

$$m_{ch}^* = m_{hh}^* \qquad \text{(parallel and perpendicular)} \quad (2.40)$$

where m_{hh}^* is the silicon heavy hole effective mass. Recall only parallel mobilities are used in PUPHS2D at this time. Section 2.7 outlines an

approach for modelling both parallel and perpendicular mobilities. ΔE in (2.35) is approximately 0.35 eV for electrons and 0.2 eV for holes [Rac89].

Figures 2.6 and 2.7 show the predicted electron and hole mobilities of four different SiGe alloys from (2.34). Note these mobilities are less than the corresponding silicon mobilities. The silicon mobility by Arora was used in (2.34) for these calculations.

2.7. Approach for Modeling Strain Effects

Some of the effects of strain on bandgap, density of states, effective masses, and carrier mobilities have already been investigated. There are additional strain effects on the electron and hole mobilities which must be addressed. Issues discussed in this section have not been implemented into PUPHS2D at this time, but they can be important in certain device structures.

Due to the splitting of the degeneracy in the valence and conduction bands, carrier mobilities are different depending on whether transport is parallel or perpendicular to the growth direction. This is an important effect in the calculation of parameters such as f_{max}, in which both lateral and vertical carrier motion must be considered. PUPHS2D currently uses only

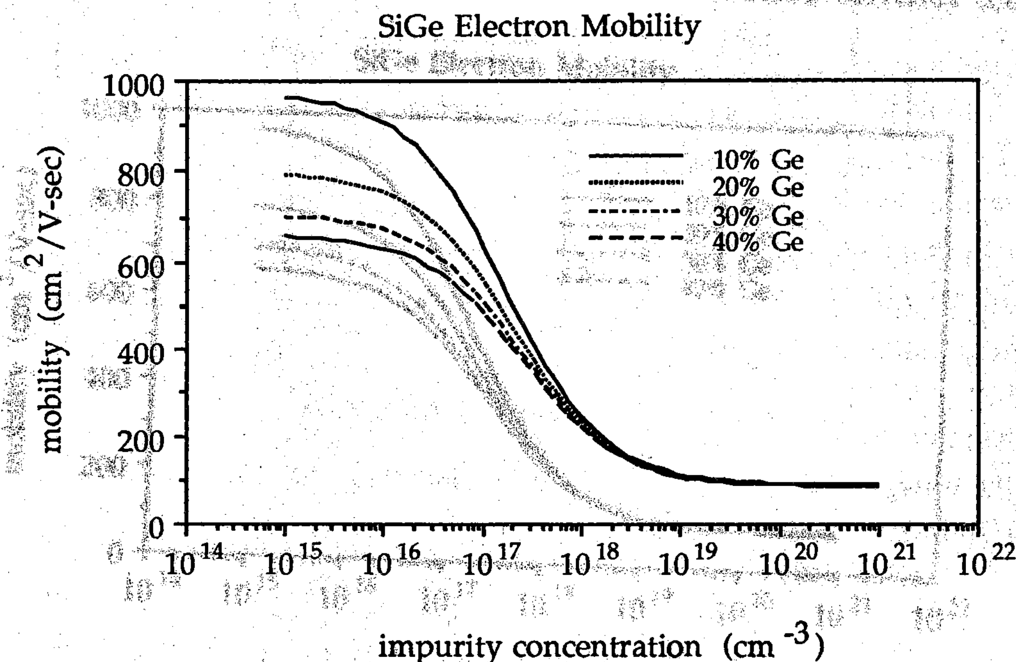

Figure 2.6 PUPHS2D $Si_{1-x}Ge_x$ electron mobilities.

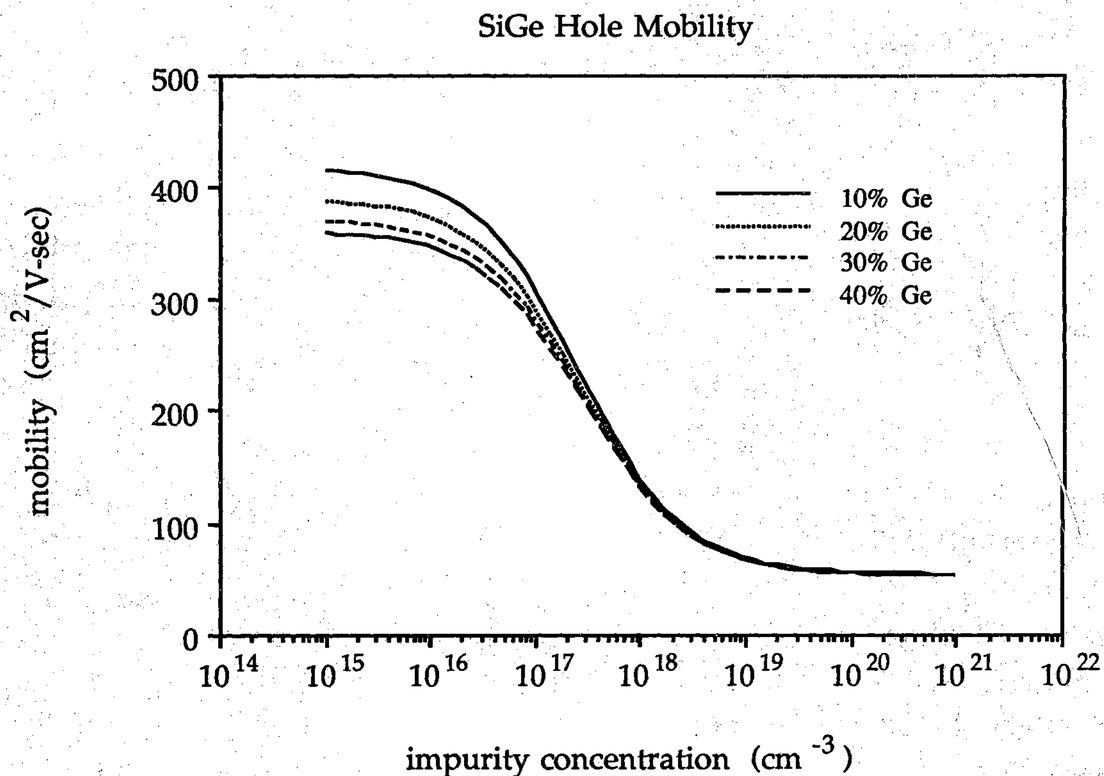

Figure 2.7 PUPHS2D $Si_{1-x}Ge_x$ hole mobilities.

mobilities parallel to the direction of growth, and this is a good approximation for most HBT geometries. Mobilities are defined between adjacent nodes, not at the node itself. PUPHS2D defines mobilities at each node and computes the average mobility between neighboring nodes when mobilities are needed in the discretised equations. The task of converting the code to enable the definition of both a parallel and perpendicular mobility is nontrivial, especially if field-dependent mobilities are used. Different mobility models must be used in the strained alloy for mobility vertically between nodes and mobility horizontally between nodes (see figure 2.8). The mobilities show up in the normalized Scharfetter-Gummel current equations [Sch81]. Hole current densities given by arrows in figure 2.8 are:

$$J_{p\parallel L} = -\mu_{p\parallel L}\frac{\Delta V_L}{h_L}\left(\frac{p_I e^{\Delta V_L} - p_L}{e^{\Delta V_L} - 1}\right) \tag{2.41}$$

$$J_{p\perp T} = -\mu_{p\perp T}\frac{\Delta V_T}{h_T}\left(\frac{p_T e^{\Delta V_T} - p_I}{e^{\Delta V_T} - 1}\right) \tag{2.42}$$

where

$$\Delta V_L = V_I - V_L \tag{2.43}$$

$$\Delta V_T = V_T - V_I. \tag{2.44}$$

Electrostatic potential and carrier concentrations are evaluated at the nodes while mobilities and current densities are evaluated midway between nodes.

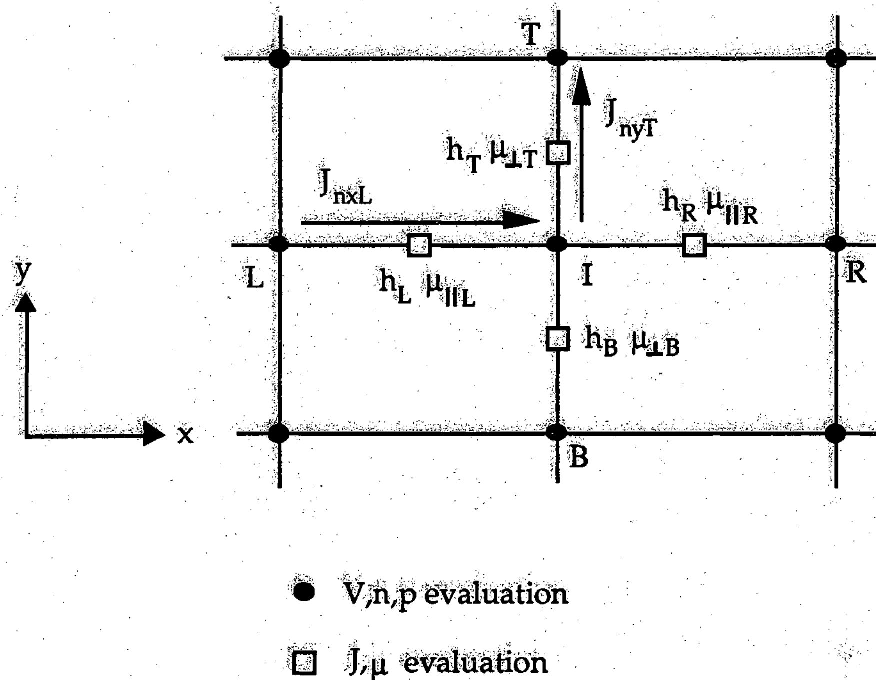

Figure 2.8 Node spacing and evaluation points within a strained alloy for a two-dimensional finite center difference mesh. Mobilities and current densities are evaluated midway between nodes.

2.8. Summary

The PUPHS2D material parameters reflect well established silicon models but rather crude SiGe models in some instances. As more findings are published on transport properties of strained SiGe, materials parameters can be updated in the code. Procedures for updating material parameters is presented in chapter 3. A very conservative approach has been taken in characterizing SiGe strained layers, especially in the carrier mobility models. Although this conservative approach underestimates SiGe mobility, the enhanced injection properties of the Si/SiGe heterojunction over a conventional homojunction are clearly illustrated in the performance advantages of the SiGe HBT versus the silicon BJT. Chapter 4 will address this issue in detail.

CHAPTER 3: MODEL DEVELOPMENT

3.1. Introduction

PUPHS2D is an accurate drift-diffusion model for two-dimensional simulation of compositionally nonuniform structures. The program has evolved over the past 10 years from a solar cell analysis program into an HBT design and analysis tool. A two-dimensional silicon solar cell program called SCAP2D was developed at Purdue in the early 1980's [Lun80,Gra82]. PUPHS1D, a one-dimensional drift-diffusion program for the evaluation of heterostructures, was completed by Schuelke in 1984 [Sch84]. Paul DeMoulin combined the solution techniques of the two-dimensional code with the heterostructure formulation into a program called PUPHS2D [DeM88], originally developed for the analysis of GaAs solar cells. Heterojunction bipolar transistor capability and transient analysis were added by Paul Dodd [Dod89]. Most recently, the $Si/Si_{1-x}Ge_x$ material system and field-dependent mobility have been added, and these additions are the subject of this chapter.

This chapter discusses the present structure of the code and two recent changes to PUPHS2D. First, the $Si_{1-x}Ge_x$ material system has been added. Procedures for changing existing material parameters and adding new material systems are discussed. Second, the addition of field-dependent mobility to the code is examined in detail.

3.2. PUPHS2D Code Structure

3.2.1. General Structure

PUPHS2D consists of seven files plus a library of files containing the material-dependent subroutines. Two additional files comprise the data retrieval program. There are only two material systems in the library at the present time, $Si/Si_{1-x}Ge_x$ and $Al_{1-x}Ga_xAs/GaAs$. Other materials can be easily

added to the library (see section 3.2.3). PUPHS2D is written in FORTRAN 77. A brief description of each of the files in PUPHS2D is given below.

puphs2d.f: This file is the main program.

input.f: This file contains subroutines which read in and check each card of the input deck.

basis.f: basis.f contains the main routines which are called during during each execution of PUPHS2D, regardless of the type of analysis. These routines include the doping definition, mesh setup, nonuniform material parameter definitions, equilibrium solver, data table printing routines, data dump routines, and many others.

options.f: Control code for each specific analysis type in in options.f. The type of analysis is specified on the compute card of the input deck.

solver.f: The nonequilibrium solution routines are in this file.

linpack.f: This file contains the banded matrix factoring and solution routines.

vector.f: vector.f contains vectorized versions of IMSL routines called in the linpack solver. If vector processing is not available, do not compile vector.f since these routines will be picked up by inclusion of the IMSL library. PUPHS2D uses the IMSL math library, version 10.0 or newer.

The material library consists of two files:

sigelib.f: Material-dependent subroutines for the $Si/Si_{1-x}Ge_x$ system are in this file. These routines include control code for field-dependent mobility, material parameters, a block of all default values and variable initializations, and a subroutine to check that the appropriate material system file has been compiled.

gaaslib.f: gaaslib.f is similar to sigelib.f. It contains material-dependent subroutines for $Al_{1-x}Ga_xAs/GaAs$.

The data retrieval program consists of two files:

retrieve.f: This is the data retrieval main program.

massage.f: Routines used by the main program to massage the data into a useful format are stored in this file.

Figure 3.1 summarizes the PUPHS2D code structure. When compiling PUPHS2D, one and only one of the material files must be compiled with the seven segments of PUPHS2D. A new character variable called SEMI has been defined on the MATTER card to ensure the proper material system file has been compiled. A disadvantage of this structure is a new material file must be created for devices comprised in a complex semiconductor system. For example, a new material file must be created to simulate an HBT which contains both silicon and GaAs layers.

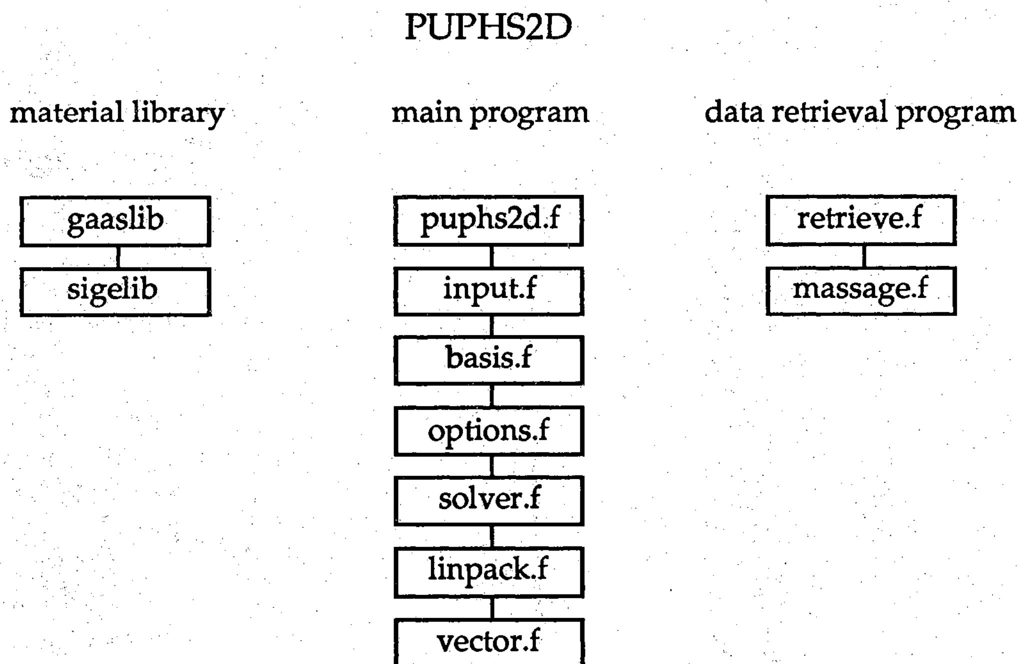

Figure 3.1 PUPHS2D code structure.

3.2.2. Material Dependent Subroutines

The subroutines which comprise the material library files will be discussed in this section. As mentioned previously, there are only two material files in the library at this time, defining the Si/SiGe and the AlGaAs/GaAs systems. Although both files contain the same basic subroutines, emphasis will be on the Si/SiGe system.

Material-dependent subroutines serve many different purposes. Among these are the definition of material parameters, setting low-field carrier mobilities, and providing control code for field-dependent mobility. A subroutine called CHSEMI checks the string in the variable SEMI in the input deck against that set in CHSEMI to ensure the user has compiled the correct material file. SEMI is set to GESI for silicon and Si/SiGe structures and ALGAAS for AlGaAs/GaAs devices. The subroutine BANDX defines most of the semiconductor material parameters as a function of mole fraction. These parameters are bandgap, electron affinity, density of states, bandgap narrowing and dielectric constant. Changing models for material parameters is as easy as finding the subroutine BANDX. Low-field carrier mobilities are set in SETMOB. Two silicon mobility models are available (see section 2.6.1). The character variable MOBSI on the ENERGY card determines which model is used. Subroutines defining the Caughy-Thomas and Arora models are called in SETMOB. These subroutines are MOBCT and MOBAR respectively, and the variable MOBSI should be set to CT for the Caughy-Thomas model or AR for the model by Arora. Additional mobility models can be used by writing a new subroutine to define the mobility, altering SETMOB to accommodate the new model, and adding a new definition for the character variable MOBSI in the subroutine RENRGY (located in input.f). Control code for field-dependent mobility is in LOCALE. Expressions for electron and hole mobility as a function of effective electric field are defined. A subroutine for damping the changes in mobility between iterations is included as well. Finally, a block of all PUPHS2D global variables is in each material file. Defaults for the appropriate material system are set, and each global variable in PUPHS2D is initialized. Defaults can be changed as deemed necessary.

3.2.3. Addition of Material Systems

New material systems can be added to the material library. The easiest way to add a new material system is to copy one of the existing material files and change the material parameters, field-dependent mobility expressions, variable defaults, and semiconductor check subroutine. A new option must be added to the variable SEMI in the subroutine RDEVICE (in input.f) for checking that the proper material system file has been compiled. Accuracy of the new material parameters must be assessed. Some experimentation will be required on field-dependent mobility to achieve convergence in as few iterations as possible. The remainder of this chapter discusses issues related to field-dependent mobility.

3.3. Field-Dependent Mobility

3.3.1. Introduction

The carrier mobilities presented in chapter 2 displayed dependence on doping and material composition. These low-field models must be considered incomplete since they do not model a very important effect. High electric fields present in the base-collector junction region of a bipolar transistor are likely to saturate the carrier drift velocity. Velocity saturation is an important effect since carrier transit time across the base-collector space charge region and through the collector influences the high frequency performance characteristics of heterojunction bipolar transistors. The magnitude of drift velocity is the product of mobility and the force which drives the carriers, and so saturation of drift velocity can be accounted for by a reduction of the effective carrier mobility.

As device dimensions continue to shrink, the drift-diffusion approximation becomes less valid and hot carrier effects more important. Although the use of a field-dependent mobility model allows velocity saturation to be modeled, other hot electron effects such as velocity overshoot and ballistic transport are not predicted. Monte Carlo techniques and hydrodynamic models have become very popular for the simulation of hot carrier effects. An alternative method for modeling velocity overshoot has been incorporated in a drift-diffusion model. In augmented drift-diffusion

[Tho82], an additional term in the current density equations is used to model the effects of spatially varying electric fields. This formulation is not ready for use, however, because accurate evaluation of coefficients in the model has not been completed.

A full energy and momentum balance equation solution is necessary to provide the best mobility model. The consequence for solving the energy and momentum balance equation in addition to the basic semiconductor equations is additional computing time. Simple field-dependent mobility expressions are used in PUPHS2D to model hot carrier effects. The formulation of this model, its implementation into PUPHS2D and convergence of solutions will be discussed in the following sections. Simulation results are presented at the end of the chapter. SiGe field-dependent mobility is assumed to be the same as in silicon.

3.3.2. Model Formulation

Caughy and Thomas [Cau67] developed one of the first field-dependent mobility models for silicon. This model includes an expression to fit measured data of carrier drift velocity dependence on electric field strength [Nor67]. The following expression fits these results well:

$$v_{n,p} = v_m \frac{\frac{E_{n,p}}{E_{crit}}}{\left[1+\left(\frac{E_{n,p}}{E_{crit}}\right)^{\beta}\right]^{\frac{1}{\beta}}} . \tag{3.1}$$

In (3.1), E_n and E_p are the effective electric fields acting on electrons and holes respectively and v_m, β, and E_{crit} are constants. Table 3.1 gives values of these constants for both holes and electrons. Field-dependent mobility is the ratio of velocity to electric field strength

$$\mu_{n,p} = \frac{\mu_0}{\left[1+\left(\frac{E_{n,p}}{E_{crit}}\right)^{\beta}\right]^{\frac{1}{\beta}}} , \tag{3.2}$$

where values for E_{crit} and β are given in table 3.1. Low-field mobility is given by

$$\mu_0 = \frac{v_m}{E_{crit}} \tag{3.3}$$

and is consistent with measured values. (3.2) is a widely used expression for field-dependent mobility, and many different numerical values for E_{crit} and β have been published. Table 3.2 summarizes these findings.

Table 3.1 Caughy-Thomas velocity-field constants.

parameter	electrons	holes
v_m (cm/sec)	1.1×10^7	9.5×10^6
E_{crit} (V/cm)	1.95×10^4	8.0×10^3
β	2	1

Table 3.2 Field-dependent mobility constants used in (3.3).

E_n^{crit} (V/cm)	E_p^{crit} (V/cm)	β_n	β_p	reference
8.57×10^3	1.8×10^4	1.11	1.21	Can75
8.7×10^3	1.2×10^4	2.9	2.6	Coe80
7.396×10^3	2×10^4	1	1	DAv79
8×10^3	1.95×10^4	2	1	Hei73,Man75

Temperature dependence of these constants has been investigated as well. Equation (3.3) can be rewritten to express mobility as a function of saturation velocity by making use of the relation

$$v_{sat} = \mu\, E_{crit}\,. \tag{3.4}$$

This is not a physical relation since saturation velocity is not a function of impurity or phonon scattering. The new expression is:

$$\mu_{n,p} = \frac{\mu_0}{\left[1+\left(\frac{\mu_0 \cdot F_{n,p}}{v_{n,p}{}^{sat}}\right)^{\beta}\right]^{\frac{1}{\beta}}}\,. \tag{3.5}$$

Note E in (3.3) has been replaced by F, which is defined as the driving force of the carriers in (3.5). This will be elaborated on later. Numerical values for v_{sat} and β are summarized in table 3.3.

Table 3.3 Field-dependent mobility constants used in (3.5).

v_n^{sat} (cm/sec)	v_p^{sat} (cm/sec)	β_n	β_p	reference
$1.1\text{x}10^7$	$9.5\text{x}10^6$	2	1	Eng81
$1.0\text{x}10^7$		1		Dan80,Kot79

PUPHS2D uses (3.5) to model velocity saturation of holes with β=1. A slightly different expression for field dependence of electron mobility is implemented in PUPHS2D [Jag69].

$$\mu_n = \frac{2\,\mu_{n0}}{1+\sqrt{1+\left(\frac{2\,\mu_{n0}\,F_n}{v_n^{sat}}\right)^2}}\,, \tag{3.6}$$

with temperature dependent saturation velocities given by:

$$v_n^{sat} = 1.45\text{x}10^7 \sqrt{\tanh\left(\frac{155K}{T}\right)} \text{ cm/s} \tag{3.7}$$

and

$$v_p^{sat} = 9.05\text{x}10^6 \sqrt{\tanh\left(\frac{312K}{T}\right)} \text{ cm/s.} \tag{3.8}$$

The well known device simulator MINIMOS uses (3.5-3.8) with energy balance to model hot carrier effects. Temperature dependent saturation velocities are from [Ahm86] and represent fits to experimental data [Can75,Ahm86]. Carrier mobility and carrier velocity versus driving force are plotted in figures 3.2 and 3.3. Field dependence of electron mobility is given by (3.6), and hole field-dependent mobility is given by (3.5). $v_n{}^{sat}$ and $v_p{}^{sat}$ are given in (3.7) and (3.8) respectively. Silicon low-field mobility is approximately 1340 cm^2/V-s for electrons and 460 cm^2/V-s for holes. Carrier velocity is simply the product of mobility and driving force:

$$|\vec{v}_n| = -\mu_n \cdot F_n \tag{3.9}$$

$$|\vec{v}_p| = \mu_p \cdot F_p \,. \tag{3.10}$$

Mobility versus driving force curves given by (3.3), (3.5) and (3.6) are very similar in shape. The crucial parameter in these expressions is F.

Nothing has been said about the driving force of carriers, but this is an extremely important parameter. The simplest interpretation is that the driving force is the component of electric field in the direction of current flow:

$$F_{n,p} = \frac{\vec{E}_{n,p} \cdot \vec{J}_{n,p}}{|\vec{J}_{n,p}|} \tag{3.11}$$

If (3.11) defines the driving force, carrier velocities given by (3.9) and (3.10) may be inaccurate. (3.9) and (3.10) hold true only if the diffusion current component is negligibly small. This assumption is violated in the base and base-emitter space charge regions of a bipolar transistor where diffusion of carriers dominates over drift. Also, a non-trivial problem arises when the dot

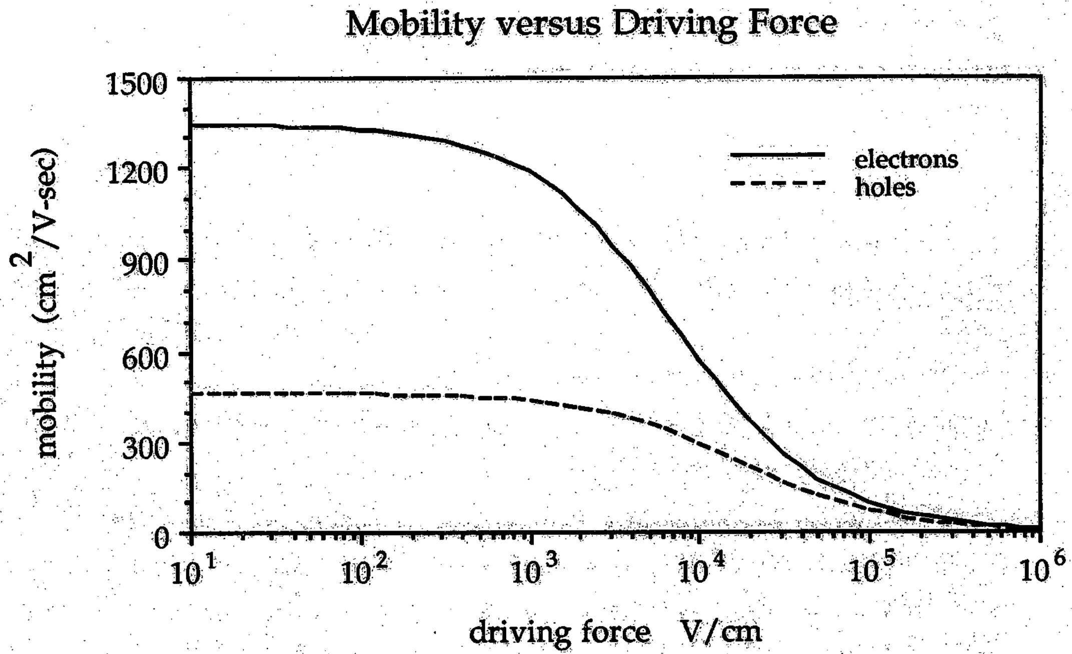

Figure 3.2 Mobility versus driving force.

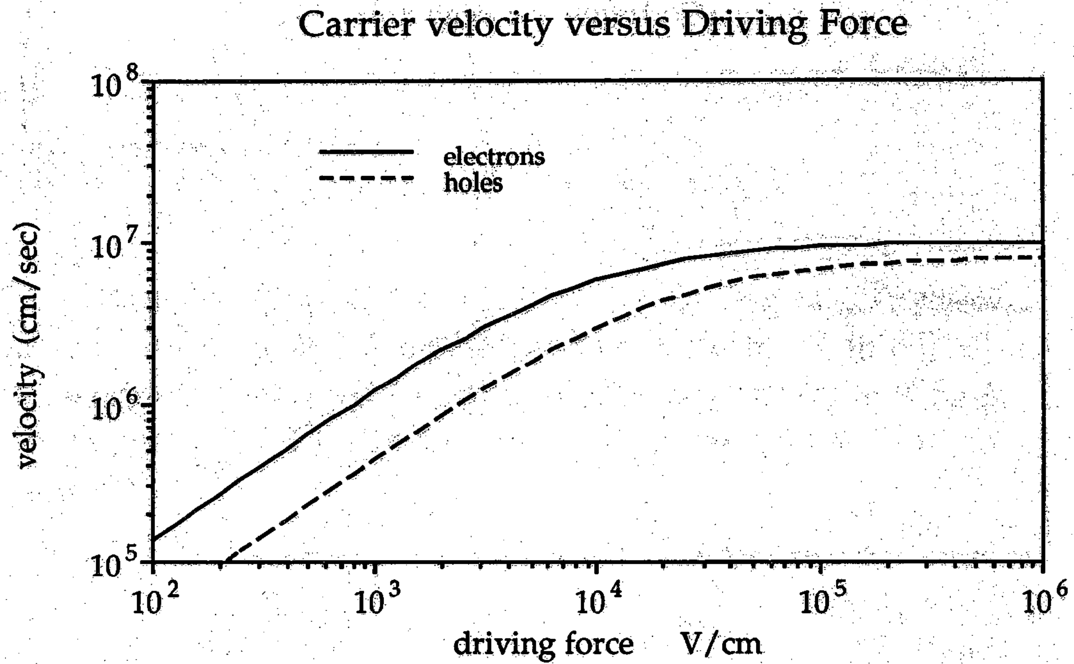

Figure 3.3 Carrier velocity versus driving force.

product of current density and electric field is positive in (3.9) or negative in (3.10). Such a situation can arise locally when the diffusion current component dominates the drift component. Device simulators have avoided the latter problem by defining the driving force as:

$$F_{n,p} = \frac{\max\left(0, \vec{E}_{n,p} \cdot \vec{J}_{n,p}\right)}{\left|\vec{J}_{n,p}\right|} \tag{3.12}$$

but this interpretation may give inaccurate field-dependent mobilities in areas of the device where diffusion dominates. The gradient of the quasi-Fermi potential is more appropriate to use as the driving force. This idea was first proposed by Gokhale. [Gok70]:

$$F_{n,p} = -\nabla\phi_{n,p} \, . \tag{3.13}$$

A simple derivation of (3.13) is in order. The derivation is presented for electrons, and a similar process can be repeated for holes. Assumptions are the lattice temperature, T, is constant and the Einstein relationship holds. Electron current density can be expressed as:

$$\vec{J}_n = q\mu_n n\vec{E}_n + qD_n\nabla n \, . \tag{3.14}$$

where

$$D_n = \frac{KT}{q}\mu_n \, , \tag{3.15}$$

Electron concentration in terms of the quasi-Fermi potential is:

$$n = n_i \exp\left[\frac{q\left(V - \phi_n\right)}{KT}\right] . \tag{3.16}$$

$$\nabla n = \frac{q}{KT} n_i \exp\left[\frac{q\left(V - \phi_n\right)}{KT}\right]\left(\nabla V - \nabla\phi_n\right). \tag{3.17}$$

but

$$\vec{E} = -\nabla V \tag{3.18}$$

and (3.16) can be rewritten making use of both (3.16) and (3.18):

$$\nabla n = \frac{-q}{KT} n\left(\vec{E} + \nabla\phi_n\right). \tag{3.19}$$

Substitution of (3.19) back into (3.14) gives:

$$\vec{J}_n = -q\mu_n n \nabla\phi_n . \tag{3.20}$$

For holes,

$$\vec{J}_p = -q\mu_p p \nabla\phi_p . \tag{3.21}$$

The gradient of the quasi-Fermi potential always points in the direction of current flow. Clearly, this is the appropriate driving force since both drift and diffusion are accounted for.

A full energy and momentum balance equation solution is necessary to provide the best possible mobility model. MINIMOS 4 uses an energy balance with field-dependent mobility to model hot carrier effects. Hansch and Miura-Mattausch [Han86a] developed an approximate solution of the energy and mobility equations which was feasible to use in conventional code. Their rationale was based on the observation that the classical current equation is rigorously valid in the limit of low fields. High-field effects enter through the saturation of drift velocity. The model uses a local field-dependent mobility and thermal voltage U_T in the modified current relationship:

$$\vec{J}_n = q\mu_n n\vec{E}_n + q\mu_n \nabla(nU_T) . \tag{3.22}$$

(3.5) and (3.6) are used to model hole and electron mobility, and the thermal voltage is given by:

$$U_T = U_{T0} + \frac{2}{3}\tau_e\, v_{sat}^2 \left(\frac{1}{\mu_{LIF}} - \frac{1}{\mu_{LI}}\right), \tag{3.23}$$

where U_{T0}=3KT/2, τ_e is the energy relaxation time, μ_{LI} is the low-field mobility, and μ_{LIF} is the field-dependent mobility. T is not the lattice temperature but the effective carrier temperature. (3.23) is valid for both electrons and holes. The driving forces for electrons and holes are:

$$F_n = \left|\vec{E}_n - \frac{1}{n}\nabla(nU_T)\right| \tag{3.24}$$

and

$$F_p = \left|\vec{E}_p + \frac{1}{p}\nabla(pU_T)\right|, \tag{3.25}$$

which reduce to the gradient of the quasi-Fermi potentials in the limit τ_e=0. Hot electron effects modify conventional carrier transport in submicron

devices. This is clearly evident in the MINIMOS simulation results of a short-channel MOSFET by Hansch and Selberherr [Han86b].

To summarize, equations (3.26) and (3.27) give the PUPHS2D field-dependent mobility expressions for electrons and holes respectively.

$$\mu_n = \frac{2\,\mu_{n0}}{1 + \sqrt{1 + \left(\frac{2\,\mu_{n0}\,F_n}{v_n^{sat}}\right)^2}} \tag{3.26}$$

$$\mu_p = \frac{\mu_{p0}}{1 + \frac{\mu_{p0} \cdot F_p}{v_p^{sat}}}. \tag{3.27}$$

Saturation velocities are given in (3.7) and (3.8). Users have two options for the carrier driving force; the magnitude of electric field, $|E_{n,p}|$, or the gradient of the quasi-Fermi potential in the direction of current flow (3.28). The former is invoked by setting the variable FORCE in the ENERGY card to EFIELD and the latter by setting FORCE to GRDQFL. (3.28) is used instead of (3.13) since the direction of the gradient of the quasi-Fermi potential may be slightly altered in the discretisation. The default of FORCE is the gradient of the quasi-Fermi potential in the direction of current, which is recommended.

$$F_{n,p} = \frac{-\nabla\phi_{n,p} \cdot \vec{J}_{n,p}}{|\vec{J}_{n,p}|} \tag{3.28}$$

In areas of the device where current density is very small, (3.28) is replaced by (3.13). The Einstein relationships have been assumed to hold true thus far (3.29 and 3.30), with T defined as the lattice temperature.

$$D_n = \frac{kT}{q}\,\mu_n \tag{3.29}$$

$$D_p = \frac{kT}{q}\,\mu_p \tag{3.30}$$

Since the lattice temperature is fixed, the carrier diffusion coefficients given by the Einstein relations show a very strong dependence on electric field. In actuality, the diffusion coefficients show a dependence on electric field but not

nearly as strong as the Einstien relations predict. Figure 3.4 shows measured results and Monte Carlo predictions of the electron diffusivity in silicon as a function of electric field. However, the Einstien relations are valid everywhere in the device if T is interpreted as the carrier temperature due to high fields. Energy balance approaches use this definition of T in the Einstien relations to compute the carrier diffusion coefficients. An option is left to the user as to whether the carrier diffusivities are to be updated using (3.29) and (3.30). The logical variable UPDIFF on the ENERGY card should be set to TRUE to update the diffusion coefficients. UPDIFF defaults to TRUE.

3.3.3. Solution of the Semiconductor Equations

Before jumping into the details of implementing field-dependent mobility in PUPHS2D, a brief review of the semiconductor equations and method of solution is presented. For more details, see [Dod89]. Poisson's equation and the current continuity equations describe the behavior of

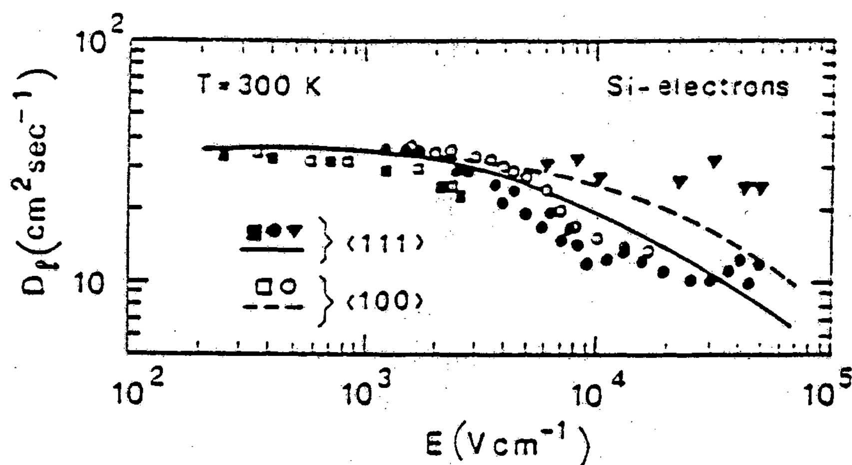

Figure 3.4 Electron diffusivity in lightly doped silicon as a function of field at 300K. Figure reprinted from [Jac89].

carriers in a device. The basic semiconductor equations under steady-state conditions are:

$$\nabla^2 V = \frac{q}{\varepsilon}(N_A - N_D + n - p) \tag{3.31}$$

$$\nabla \cdot \vec{J}_n = q(R - G) \tag{3.32}$$

$$\nabla \cdot \vec{J}_n = q(R - G) \tag{3.33}$$

In (3.31-3.33), $\vec{J}_n$ and $\vec{J}_p$ are the electron and hole current densities and R and G are the recombination and generation rates per unit volume. The current densities in compositionally non-uniform devices are given by:

$$\vec{J}_n = -qn\mu_n\nabla(V + V_n) + qD_n\nabla n \tag{3.34}$$

$$\vec{J}_p = -qp\mu_p\nabla(V - V_p) - qD_p\nabla p \,. \tag{3.35}$$

V_n and V_p are the band parameters defined by:

$$qV_n = \chi - \chi_{ref} + kT \ln\left[\frac{N_C}{N_{Cref}}\right] \tag{3.36}$$

$$qV_p = -(\chi - \chi_{ref}) - (E_g - E_{g\,ref}) + kT \ln\left[\frac{N_V}{N_{Vref}}\right], \tag{3.37}$$

where χ is the electron affinity, N_C and N_V are the conduction and valence band density of states, E_g is the energy bandgap of the semiconductor, and the subscript "ref" indicates that parameter is evaluated in some reference material. PUPHS2D assumes Boltzmann statistics, and the Einstein relations are assumed to hold true.

The semiconductor equations are discretised and written in terms of the current densities, electrostatic potential, carrier concentrations, and generation and recombination rates.

$$f_v = f(V,n,p) = 0 \tag{3.38}$$

$$f_n = f(\vec{J}_n,R,G) = 0 \tag{3.39}$$

$$f_p = f(\vec{J}_p, R, G) = 0 \tag{3.40}$$

Current densities are discretised using the well-known Scharfetter-Gummel discretisation, but the Einstein relation is removed from the current equations since it is not valid in regions of high electric field [Bea88]. The appropriate boundary conditions are applied at the contacts.

This set of nonlinear equations must be solved analytically. The Newton iterative technique linearizes the problem. In matrix form, the Newton technique is expressed as:

$$\bar{J}(\bar{u}^k)\,\Delta\bar{u}^{k+1} = -\bar{F}(\bar{u}^k) \tag{3.41}$$

where $\bar{F}$ is the vector of equations (3.38)-(3.40) and $\bar{u}^k$ is the vector of the unknowns at each node after the kth Newton iteration.

$$\bar{F} = \begin{bmatrix} f_{v\ 1,1} \\ f_{n\ 1,1} \\ f_{p\ 1,1} \\ \vdots \\ f_{v\ m,n} \\ f_{n\ m,n} \\ f_{p\ m,n} \end{bmatrix}, \quad \bar{u}^k = \begin{bmatrix} v_{1,1} \\ n_{1,1} \\ p_{1,1} \\ \vdots \\ v_{m,n} \\ n_{m,n} \\ p_{m,n} \end{bmatrix} \tag{3.42}$$

$\bar{J}$ is the Jacobi matrix which contains derivatives of of each of the nodal equations with respect to the nodal variables. For improved convergence, the matrix equation is formulated in terms of the electron and hole quasi-Fermi potentials, ϕ_n and ϕ_p. The correction vector $\Delta\bar{u}^{k+1}$ consists of corrections to the variables v, ϕ_n and ϕ_p. Carrier concentrations are computed from:

$$n = n_{i\,ref} \exp\left[\frac{q(V + V_n - \phi_n)}{kT}\right] \tag{3.43}$$

$$p = n_{i\,ref} \exp\left[\frac{-q(V - V_p - \phi_p)}{kT}\right] \tag{3.44}$$

The problem is a linear system of equations of the form $Ax = b$ at each Newton iteration, where A is the Jacobi matrix, x is the vector of corrections,

and b is the vector of equations to be solved evaluated at the last iteration. Each iteration solves the matrix equation for the correction vector $\Delta\bar{u}^{k+1}$. $\bar{u}^k$ is updated prior to the next iteration. After several iterations, hopefully $\Delta\bar{u}^{k+1}$ approaches the zero vector and the solution has converged. However, due to the highly nonlinear nature of the problem, the solution may diverge.

3.3.4. Model Implementation

Solution of the basic semiconductor equations simultaneously with the field-dependent mobility expressions (3.26 and 3.27) is sought. Users also have the option of not solving the field-dependent mobility equations. An iterative, uncoupled method of solution is employed. A separate subroutine controls the field-dependent mobility. The partial derivatives of the mobilities with respect to the unknowns, namely electrostatic potential and the quasi-Fermi potentials, are not included in the Jacobian. A simulation study in two dimensions [Fra83] has shown no significant loss in the rate of convergence when the partial derivatives are left out of the Jacobian. There are advantages to solving the problem with an uncoupled technique. Computing the partial derivatives of mobility to use in the Jacobian is time consuming, and these must be evaluated separately for each different material system. The flowchart in figure 3.5 describes the field-dependent mobility solution algorithm.

The solution algorithm proceeds as follows. Unknowns V, ϕ_n and ϕ_p are solved for, and the effective carrier driving force in the direction of current flow is computed. PUPHS2D allows one to choose either the magnitude of the electric field or the gradient of the quasi-Fermi potential in the direction of current as the effective carrier driving force. Field-dependent mobilities are computed after each iteration. A check is performed to see if the electron mobility has converged to within a user-specified tolerance in percent. The default is 5 percent. Only the electron mobility is checked for convergence. If the electron mobility has not converged, the change in electron mobility is damped and both electron and hole mobility are updated. When the electron mobility converges, FINISH is set to TRUE and mobilities are no longer updated. The lower loop of the flowchart is effectively removed, and iteration proceeds until the solution has converged.

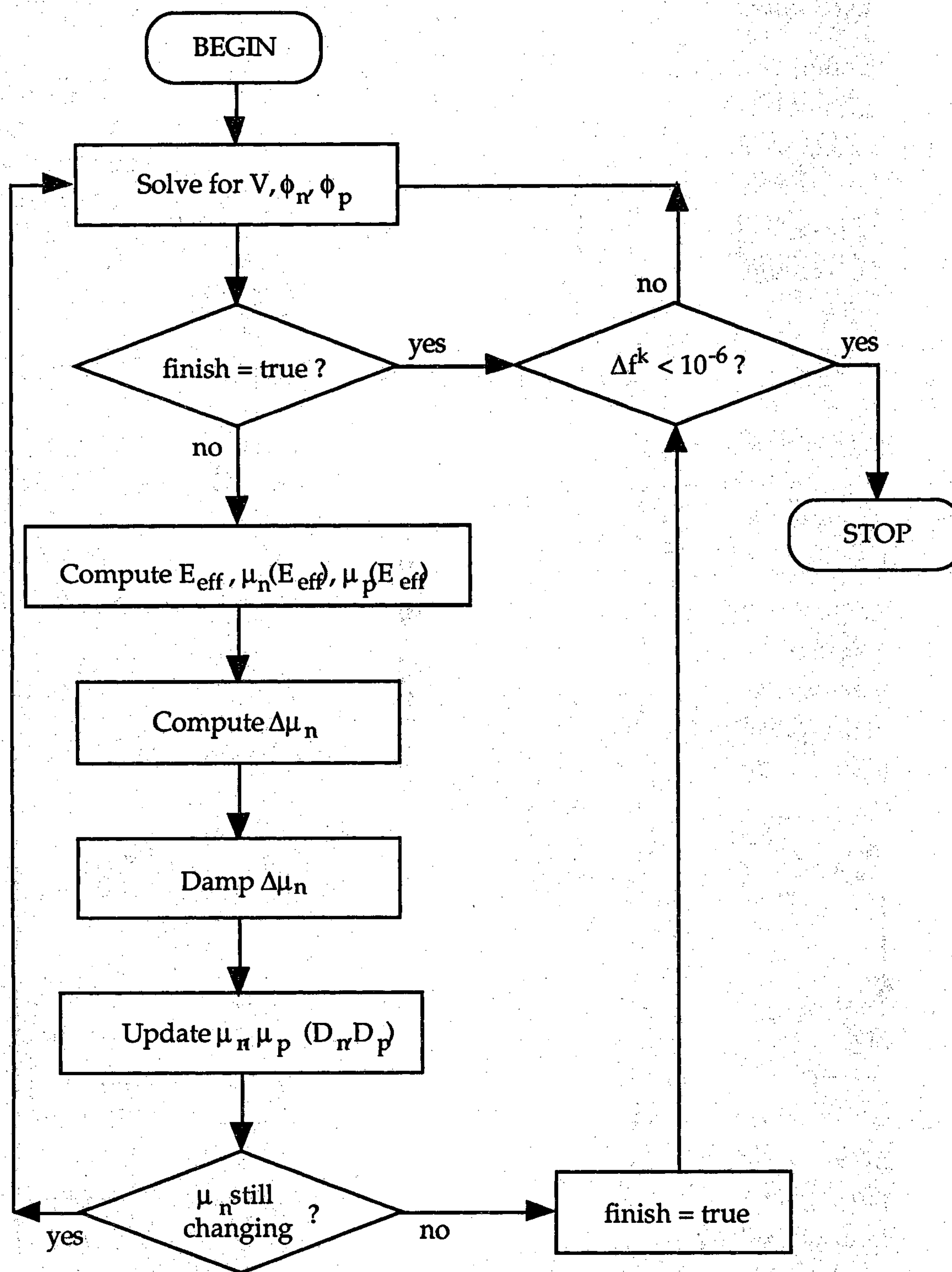

Figure 3.5 Field-dependent mobility algorithm flowchart.

Several options for damping the changes in mobility are available. Any combination of the options is allowed, and damping can be omitted by allowing the damping variables assume their default values. Mobility change is calculated by:

$$\Delta\mu_n = \frac{\mu_{new} - \mu_{old}}{\mu_{old}} \times 100\% \qquad (3.45)$$

The variable ALPHA damps the change in electron mobility by the power ALPHA:

$$\Delta\mu_n = \left(\Delta\mu_n\right)^{\alpha} \qquad \left(0 \leq \alpha \leq 1\right) \qquad (3.46)$$

In (3.46), $\Delta\mu_n$ is in percent. The default value for ALPHA is 1.0. GAMMA specifies the maximum allowable change in electron mobility (in percent) between iterations. The default value for GAMMA is 1000%. DAMPMU is a logical variable which, if true, computes the new electron mobility using (3.47):

$$\mu_n = \mu_n\left(1 \pm \Delta\mu_n\right). \qquad (3.47)$$

Mobility change is added if $\mu_{new} > \mu_{old}$. The default value of DAMPMU is FALSE.

Convergence of the solution depends on the device structure. Nonrectangular geometry devices (devices with insulator regions) tend to have problems with convergence when field-dependent mobility is activated and UPDIFF=FALSE. The solution converges if the diffusivities are updated with the mobilities, but these values of diffusivity are known to underestimate the actual values in silicon. High frequency characteristics such as f_T are more accurate when field-dependent mobility is activated. The solution for most devices converges quickly without damping the changes in mobility. The magnitude of electric field is an option for FORCE rather than the component of electric field in the direction of current flow since the latter has problems with convergence. Figure 3.6 shows how the residual norm decreases for both constant and field-dependent mobility in a non-planar

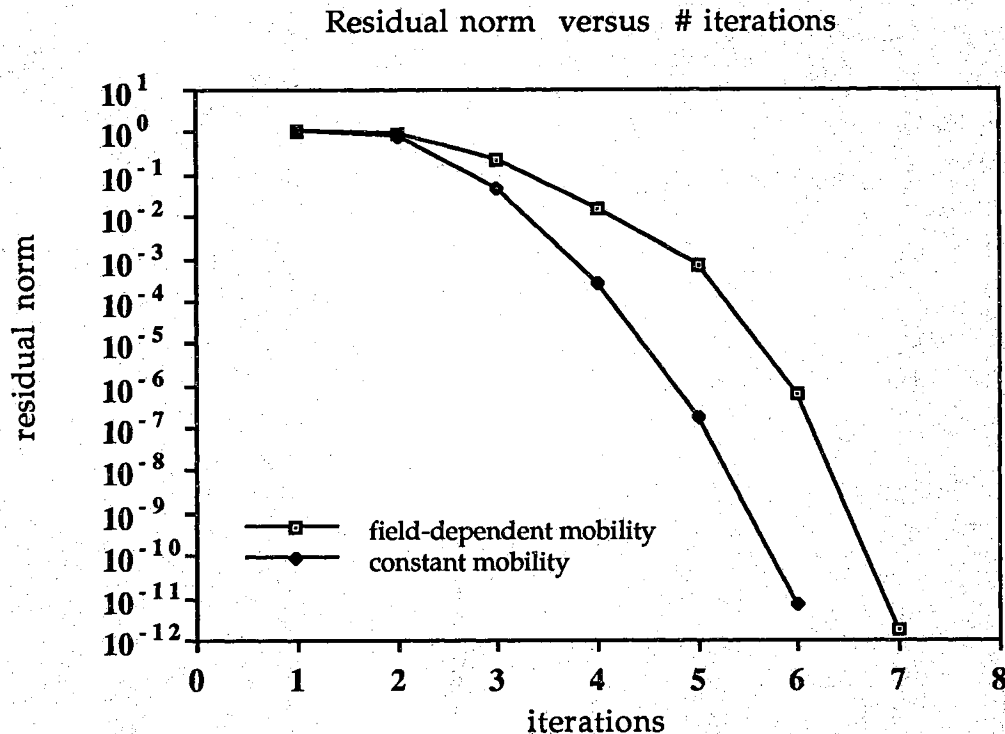

Figure 3.6 Convergence of solution for field-dependent mobility and constant mobility models.

bipolar transistor with MMXPCT=1 (the maximum percent change in electron mobility allowed for self-consistency), UPDIFF=TRUE, and bias steps of 0.1 volt. In general, field-dependent mobility requires 1-3 additional iterations per bias point which amounts to less than 20 percent more CPU time.

3.4. Model Verification

3.4.1. Introduction

Two significant changes have been made to PUPHS2D; the addition of both field-dependent mobility and the Si/SiGe material system. In order to assess the accuracy of the numerical model, two test cases will be examined.

In each of the test cases, a device structure with variation in only one dimension is simulated in two dimensions due to the lack of simple analytic solutions for two-dimensional problems. Simulation results for a silicon NIN diode are presented, and qualitative arguments are used to verify the accuracy of the field-dependent mobility models. Simulation results of a silicon homojunction diode and a $Si/Si_{0.8}Ge_{0.2}$ heterojunction diode are compared with analytical solutions to verify the accuracy of the SiGe material parameters.

3.4.2. NIN diode

The silicon NIN diode in figure 3.7 is the structure for simulations in this section. The device is basically a one-dimensional structure, and simulation results are presented in one dimension since there is no variation in the other. This device was simulated with and without field-dependent mobility. Figures 3.8 through 3.11 are results for a simulation with field-dependent mobility. In this example, UPDIFF=TRUE (diffusion coefficients are updated using the Einstien relationship) and FORCE=GRDQFL (the driving force of the carriers is the gradient of the quasi-Fermi potential in the direction of current flow). Plots of electron concentration, electric field, electron mobility and electron velocity versus position are shown for several

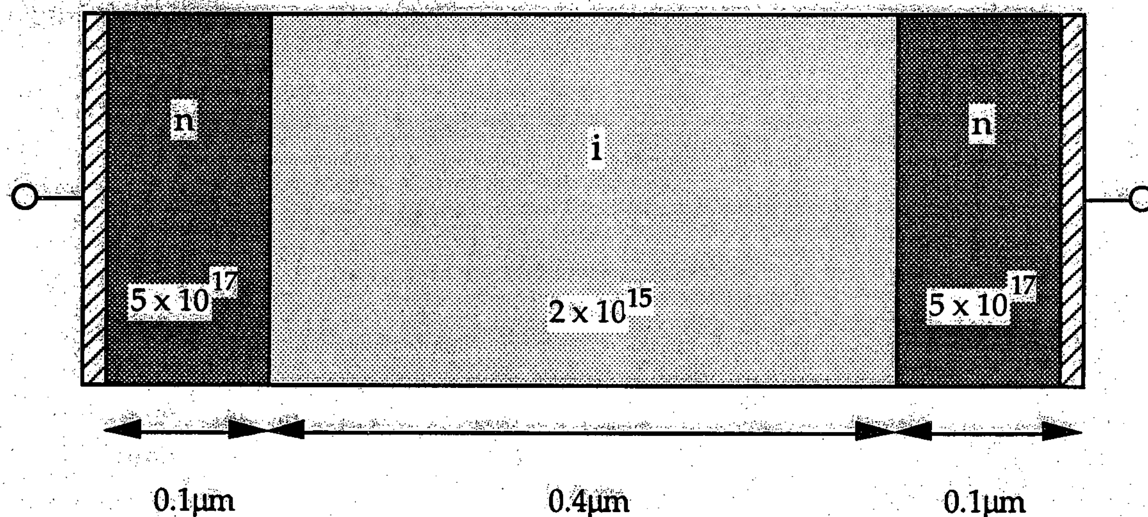

Figure 3.7 NIN diode device structure.

biases. Positive bias is applied to the right side of the device (x=0.6μm). As the bias increases, the electric field in the intrinsic region increases. Electron mobilities in the intrinsic region decrease with increasing bias and are well below their equilibrium values. In the n^+ regions, the electron mobility is low due to heavy doping effects. Some nonphysical results are evident in the electron concentration and electron velocity plots. As the bias increases, a sharp valley in electron concentration forms near the boundary of the intrinsic and n^+ regions (x=0.5μm). This leads to a spike in the electron velocity since velocity is proportional to electron current density divided by electron concentration (the spike disappears when the diffusion coefficients are not updated as illustrated in figure 3.13). Clearly these results are nonphysical. They are a consequence of updating the electron diffusion coefficient using the Einstien relation. The extremely low electron diffusivity prevents electrons in the n^+ region from diffusing into the intrinsic region at x=0.5μm. Current voltage characteristics for the NIN diode are given in figure 3.12 for simulations with and without field-dependent mobility. Current is considerably lower with field-dependent mobility due to low electron mobility. Updating the diffusion coefficients has little effect on the IV characteristics. The electron velocity curves (v=1.5 volts) in figure 3.13 demonstrate the most important effect of field-dependent mobility, velocity saturation. Electrons have excessive velocities if velocity saturation is not modelled. Electrons are faster in the N^+ regions for the case of no field-dependent mobility since the electron current density is higher. Since the electron diffusion coefficient is dependent on electric field (see figure 3.4), the actual electron velocity versus position curve would resemble the update=true curve in figure 3.13 without the spike.

3.4.3. SiGe Heterojunction Diode

The accuracy of the SiGe material parameters will be demonstrated by simulation of a one-dimensional heterojunction diode. Figure 3.14 shows the device structure. Simulation results for a homojunction and heterojunction diode are compared in order to show the superior injection properties of the heterojunction. The heterojunction diode consists of an N^+

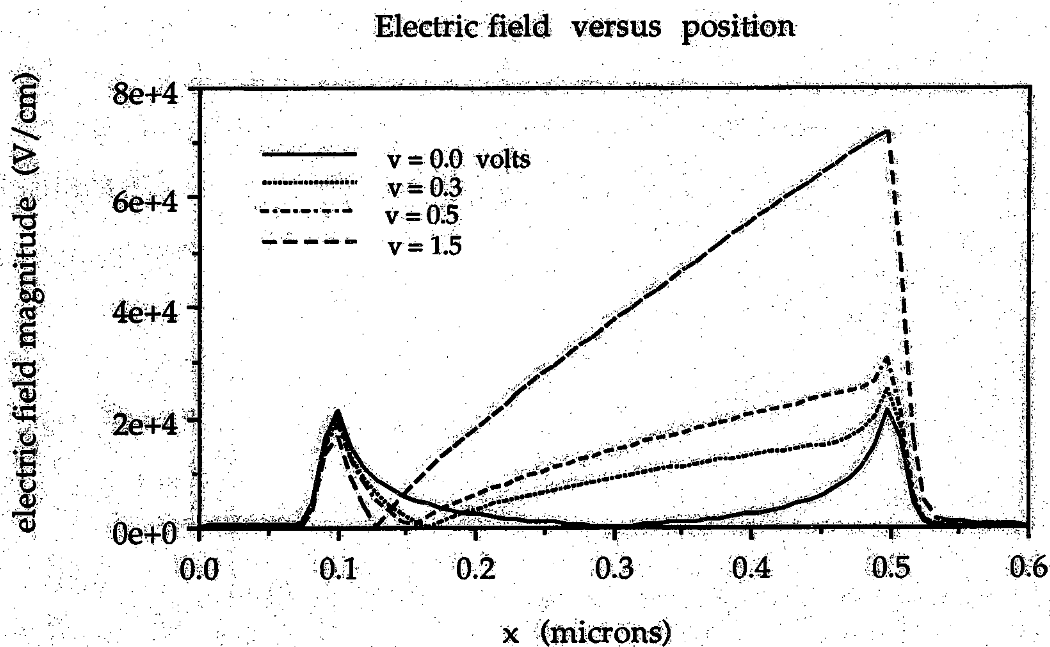

Figure 3.8 Electric field magnitude in an NIN diode.

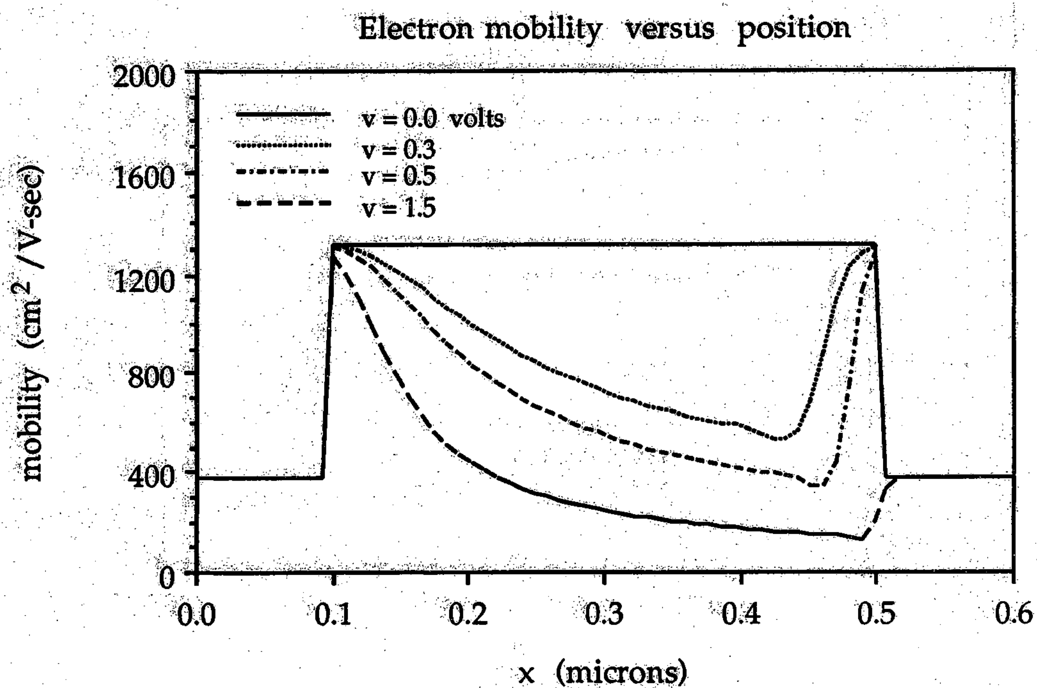

Figure 3.9 Electron mobility in an NIN diode.

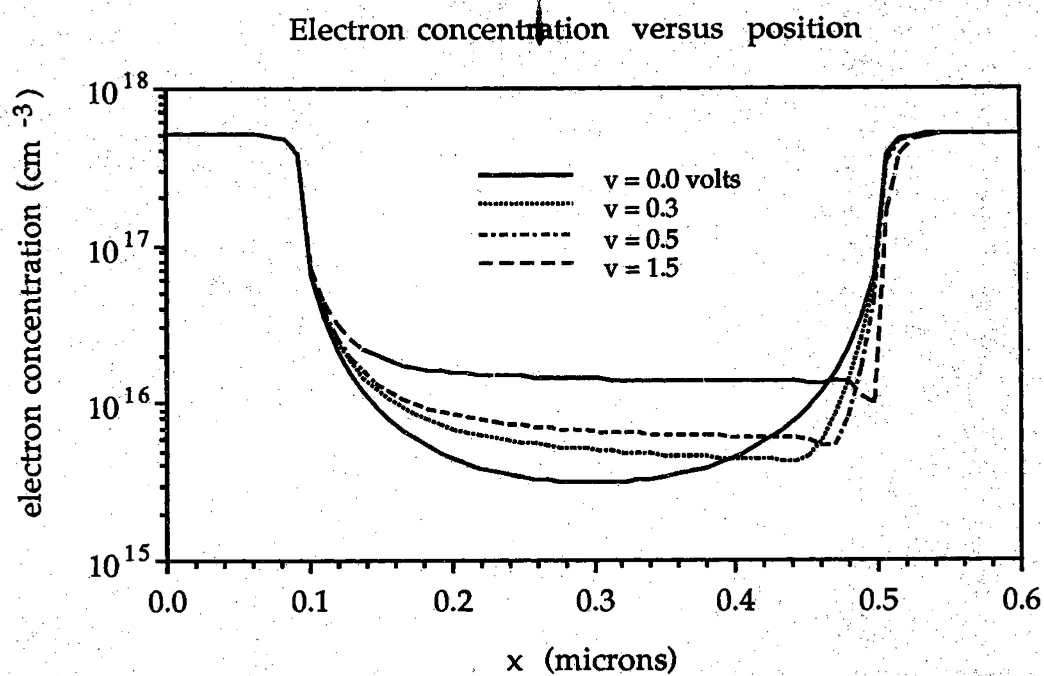

Figure 3.10 Electron concentration in an NIN diode.

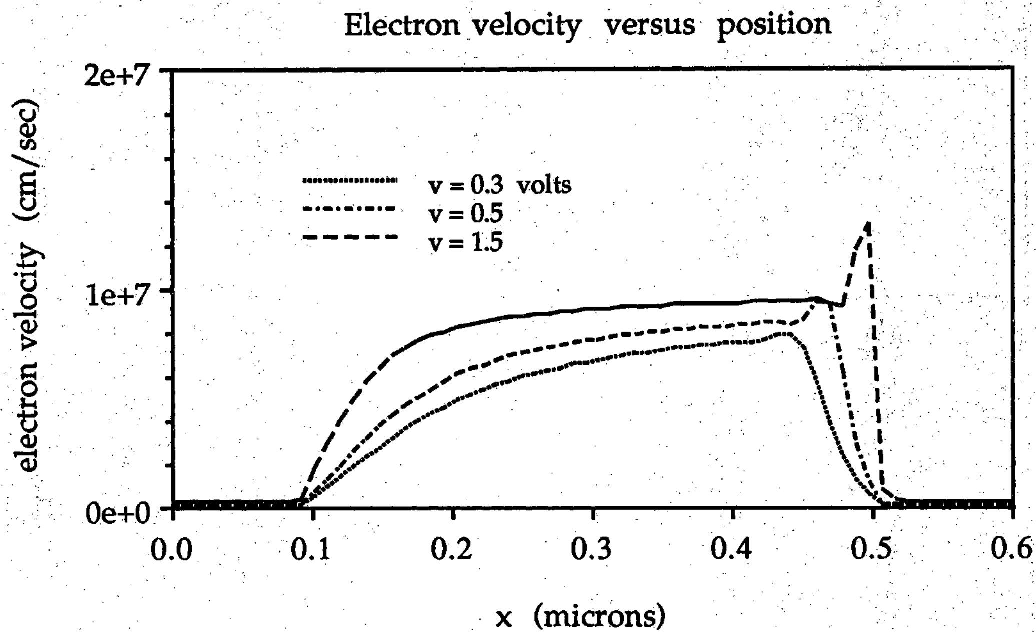

Figure 3.11 Electron velocity in an NIN diode.

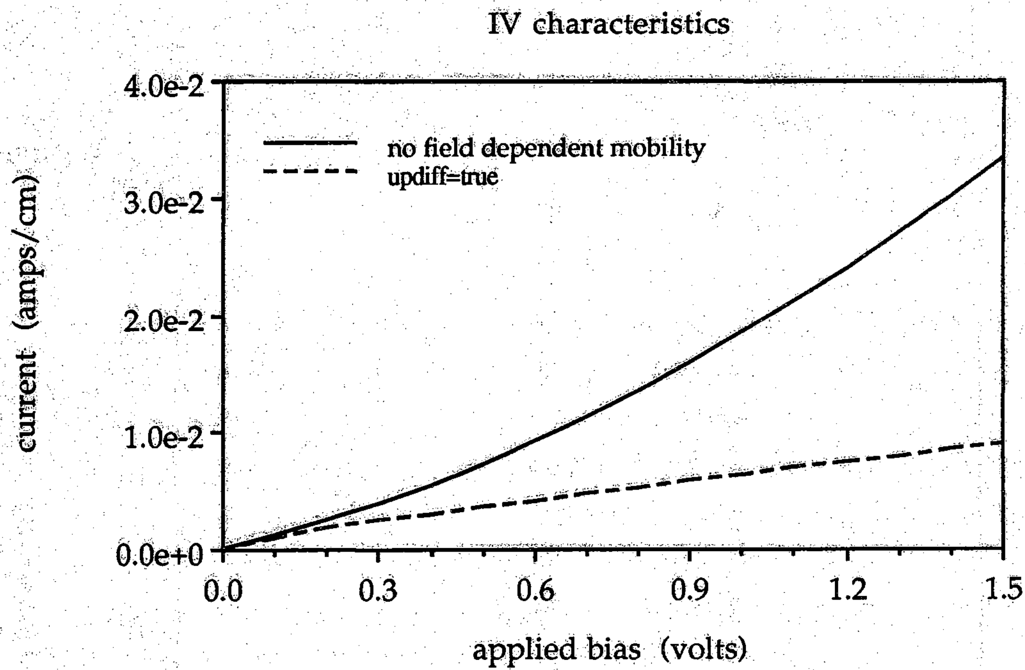

Figure 3.12 IV characteristics for the NIN diode.

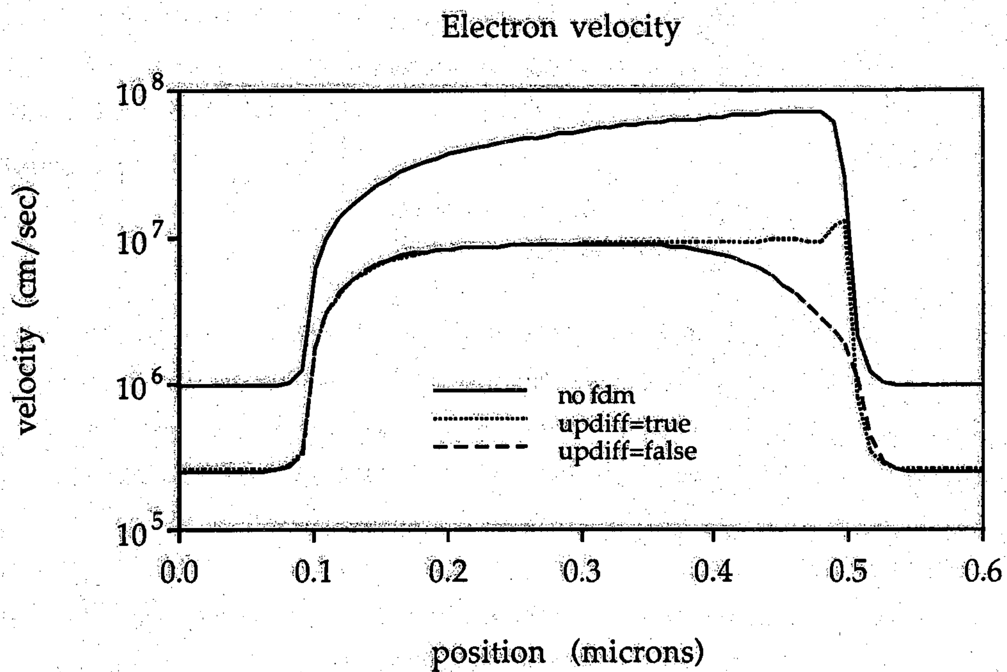

Figure 3.13 Electron velocity in the NIN diode at a bias of 1.5 volts.

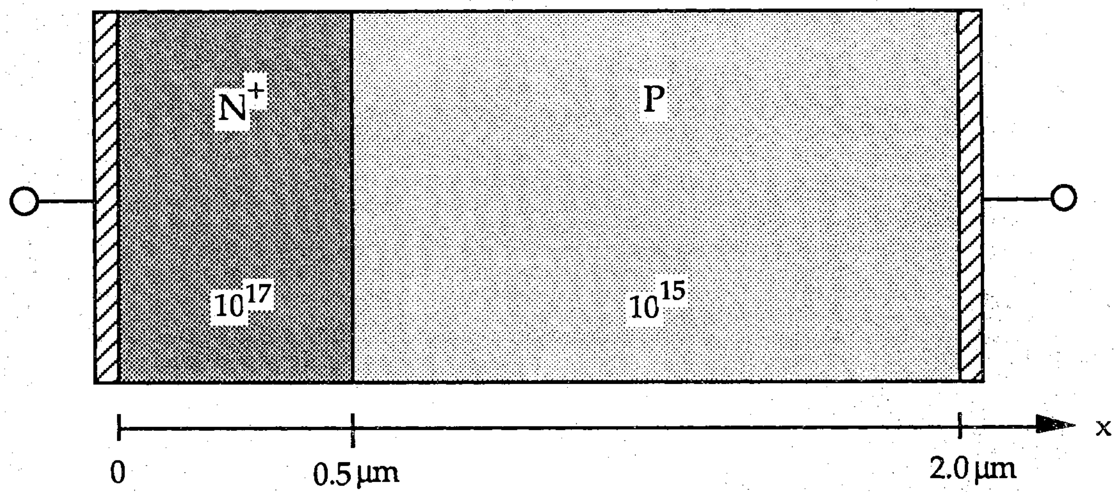

Figure 3.14 N+P diode simulation structure.

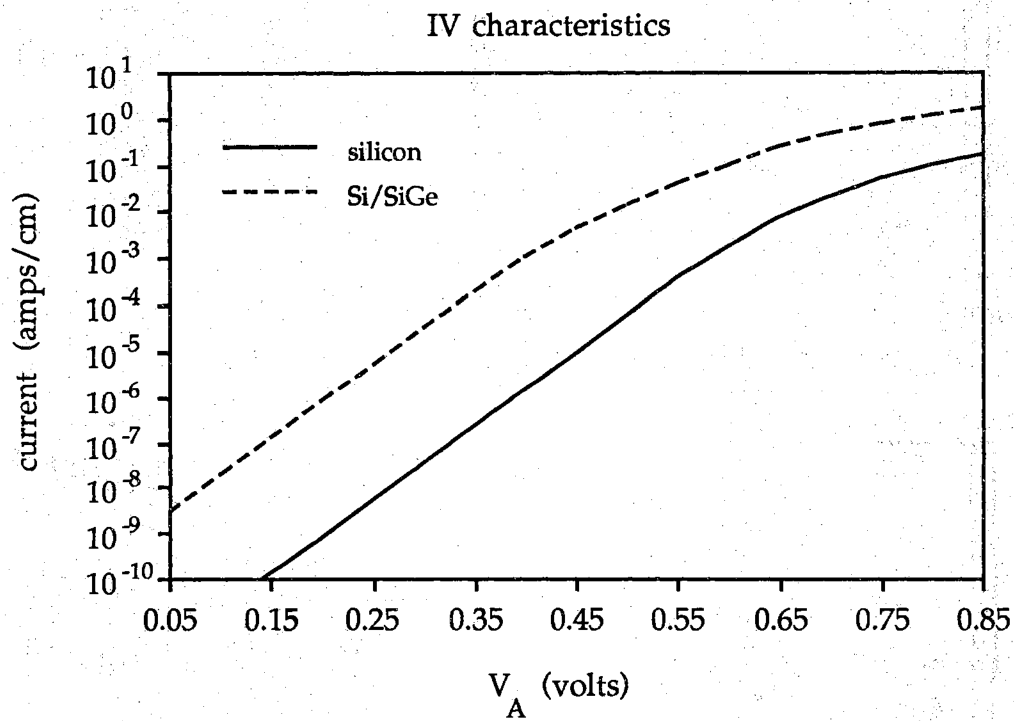

Figure 3.15 IV characteristics of the silicon homojunction diode and $Si/Si_{.8}Ge_{.2}$ heterojunction diode.

silicon region and a short-base $Si_{.8}Ge_{.2}$ P region. This junction is similar to the base-emitter junction of an HBT.

IV characteristics are illustrated in figure 3.15. Under moderate forward bias conditions the current in an N+P diode can be expressed as:

$$I = qA\left[\frac{D_n n_{ip}^2}{WN_A}\right]\exp\left(\frac{qV_A}{nkT}\right) \tag{3.48}$$

where A is the area of the junction, D_n is the minority carrier electron diffusion coefficient, W is the width of the quasi-neutral base (P region), N_A is the acceptor concentration, n_{ip} is the intrinsic concentration in the p region, V_A is the applied bias, and n is the ideality factor. Both diodes exhibit regions of ideal current, the linear portion of each curve for which n=1, in forward bias. The actual values of n from figure 3.15 are 1.04 for the silicon diode and 1.05 for the Si/SiGe diode. As the junction is biased further, the ideality factor increases due to high level injection, and series resistance further increases n at even higher bias. The onset of high level injection occurs at a lower bias in the heterojunction diode which is expected since there is considerably more current flowing than in the homojunction diode. A quick examination of (3.48) shows the current is proportional to $n_i^2 D_n$ in the P region. Hence the ratio of current in the heterojunction diode to that in the homojunction diode at a given bias in the n=1 region should be:

$$\frac{I_{hetero}}{I_{homo}} \approx \frac{n_{i\,(SiGe)}^2 D_{n(SiGe)}}{n_{i\,(Si)}^2 D_{n(Si)}} \tag{3.49}$$

where n_i is evaluated in the P region. Using PUPHS2D calculations of intrinsic concentrations and diffusion coefficients, this ratio is about 1200. Data from figure 3.15 shows this ratio to be about 1000. The conduction band discontinuity was specified to be 15% by setting DECFRC=0.15 on the MATTER card in this simulation. However, the above analysis is valid only for ΔE_c=0. Simulation shows the current ratio increases slightly when ΔE_c=0.

The superior injection properties of the heterojunction are obvious from the electron concentration plot in figure 3.16. A forward bias of 0.7 volts

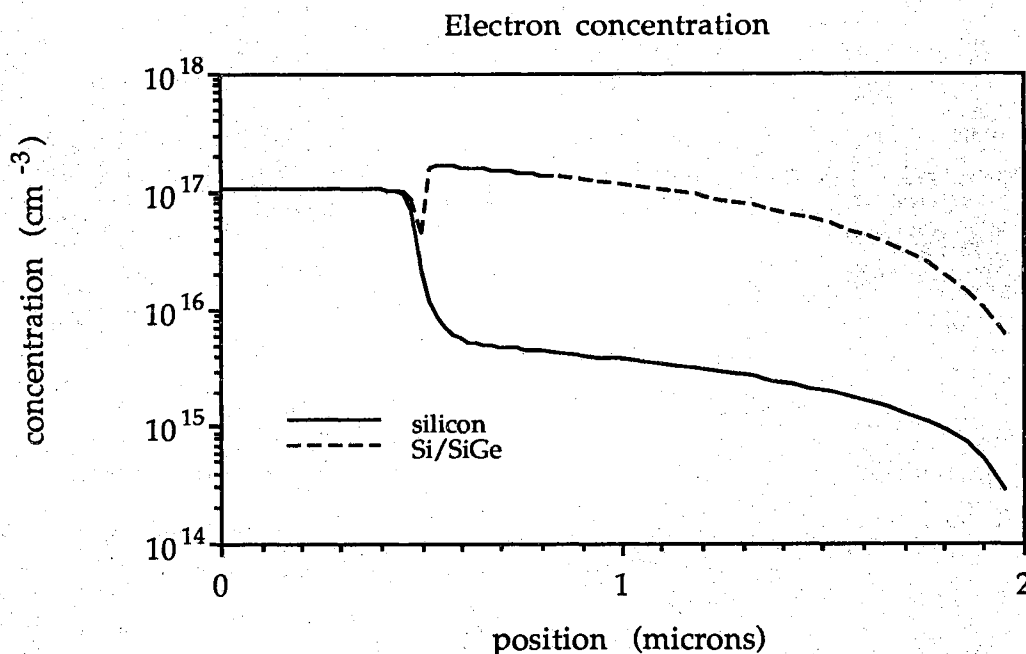

Figure 3.16 Electron concentration in the silicon homojunction diode and Si/SiGe heterojunction diode for V_A=0.7 volt.

is applied to the device which results in high-level injection since the electron concentration in the P region is much greater than the hole concentration in the base. Far more electrons are injected into the P region if it is $Si_{0.8}Ge_{0.2}$ rather than silicon. The valley in electron concentration near the heterojunction is due to the small conduction band discontinuity, about 0.02eV, in a $Si/Si_{.8}Ge_{.2}$ heterojunction. Excess electron concentration in each diode is plotted in figures 3.17 and 3.18. Current in an N^+P diode is proportional to the slope of the excess electron concentration in the P region (see [Neu83]), and from these figures, it is obvious that the gradient is much larger in the case of the heterojunction diode.

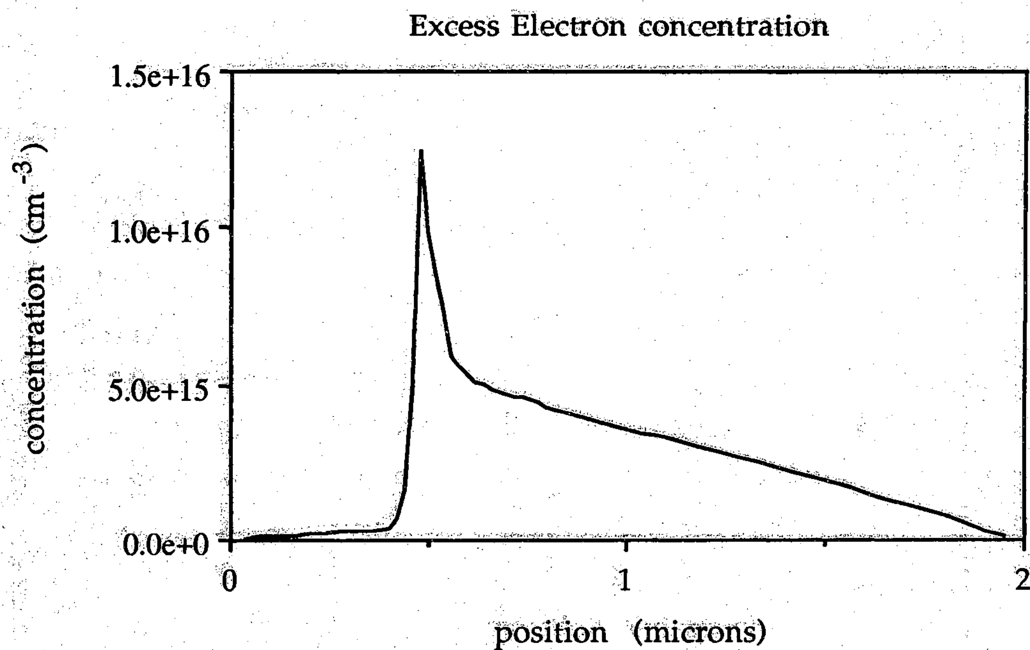

Figure 3.17 Excess electron concentration in the silicon diode for V_A=0.7V.

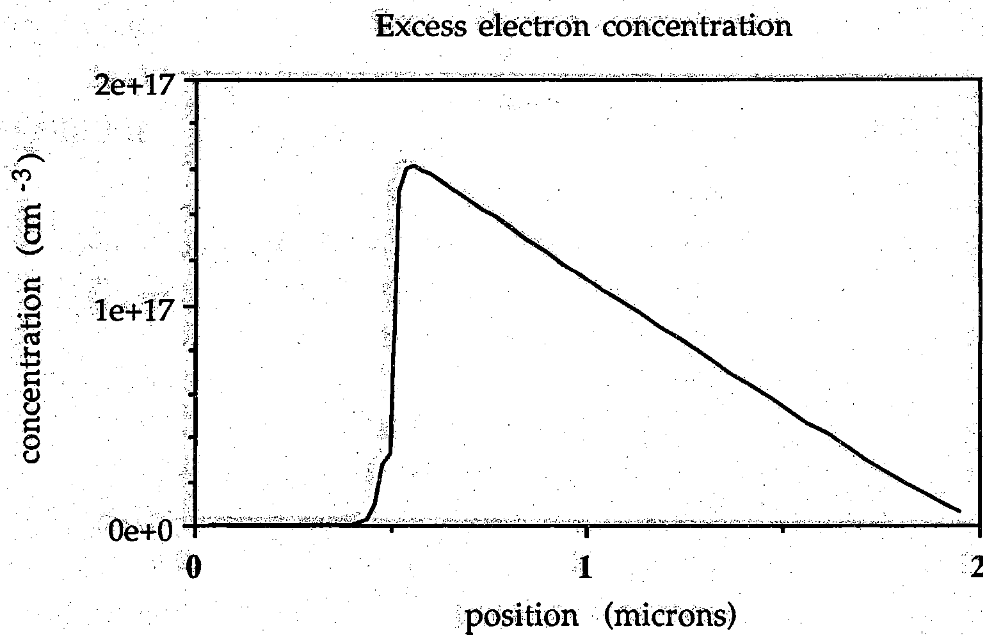

Figure 3.18 Excess electron concentration in the Si/SiGe diode for V_A=0.7V.

3.5. Summary

PUPHS2D has undergone two major changes recently. The Si/SiGe material system has been added, and the code structure has been altered to easily accommodate additional material systems as well. The addition of field-dependent mobility allows accurate simulation of hot carrier effects. Two one-dimensional structures have been simulated to asses the accuracy of the field-dependent mobility model and the SiGe material parameters. The results indicate the models do indeed predict physical findings. Some interesting physical phenomena have been investigated in these one-dimensional examples. However, PUPHS2D is a two-dimensional device simulation tool. In chapter 4, results of two-dimensional simulation of BJT's and HBT's are presented and studied.

CHAPTER 4: A SIMULATION STUDY OF HIGH-SPEED BIPOLAR TRANSISTORS

4.1. Introduction

High-speed bipolar transistors have important applications in digital circuits and as microwave devices. Semiconductor manufacturing technology has become very sophisticated in recent years to meet the demand for such high performance devices. With all of its processing advantages, silicon is by far the most cost-effective material in which devices can be fabricated. Bipolar transistors with room temperature unity current-gain cutoff frequencies (f_T) of nearly 50 GHz have been fabricated in silicon [Sug89,Cra90]. However, limitations imposed by breakdown voltage, base resistance, and punchthrough limit the applications of these devices. Silicon BJT's are reaching fundamental limits imposed by the nature of the semiconductor. Si/SiGe heterojunction bipolar transistors offer the improved performance of heterojunction technology and many of the processing advantages of silicon.

The goal of this chapter is to give some insight into the future performance of high-speed bipolar transistors fabricated in silicon and SiGe technologies. Computer simulation of both silicon and Si/SiGe transistors will allow some predictions of the future of SiGe technology and its advantages over silicon. Field-dependent mobility is modeled in the simulations in order to more accurately model high field transport. The chapter begins with a simulation of a conventional NPN silicon bipolar transistor. This will give the reader confidence in PUPHS2D as an accurate two-dimensional transistor simulation tool. Shortcomings of the design will be discussed, and an improved design is presented along with simulation results. Next, advanced SiGe HBT's are studied beginning with a SiGe HBT with a constant SiGe mole fraction in the base. Various design options such as base grading and junction grading are investigated, and their effects on

performance are presented. Finally, a study on possible improvements to the advanced devices for higher f_T's is presented. A brief summary of the results concludes this chapter.

4.2. Conventional Silicon Bipolar Transistors

Conventional silicon bipolar transistors typically have diffused or implanted regions in a lightly doped epitaxial layer. A heavily doped subcollector provides a good ohmic contact and a low resistance path for carriers as they are collected. The transistor which is examined in this section is similar to the conventional 20 GHz homotransistor presented by Ugajin [Uga89]. By making use of symmetry, the device structure can be made very simple. Figure 4.1 gives the conventional BJT device structure used in the PUPHS2D simulations for this section. The emitter is 1000 Å wide with a complementary error function doping profile. In order to model the effects of a polysilicon emitter, a hole recombination velocity of 10^5 cm/sec is set at the n-type contacts. The base is 1000 Å wide with a Gaussian doping profile and a peak doping of 10^{18} cm^{-3}. The collector doping is 5×10^{16} cm^{-3}. Prominent features of the design are the 1000 Å base width, lightly doped collector, and relatively large surface features such as the two micron base contact. Simulations were performed with and without field-dependent mobility for V_{CE}=1 volt and V_{BE} biases ranging from 0 to 1.2 volts.

The aforementioned design features are very important to the operation of the device. Three important issues in the design of bipolar transistors are base resistance, base-collector junction breakdown, and base punchthrough. Low base resistance is desired in most applications. However, breakdown and base punchthrough are undesirable. Punchthrough will not occur since this particular device has a relatively wide base and moderate base doping. The base and collector are not highly doped, and the collector-base reverse bias is small enough that the junction will not break down. As the base width is scaled down in transistors, these factors become increasingly more important. The relatively large feature sizes make for large parasitics, which in turn add to the electron transit time and decrease f_T. The base transit time is the largest delay time in this device due to the large base width. Faster devices can be realized by considering these issues.

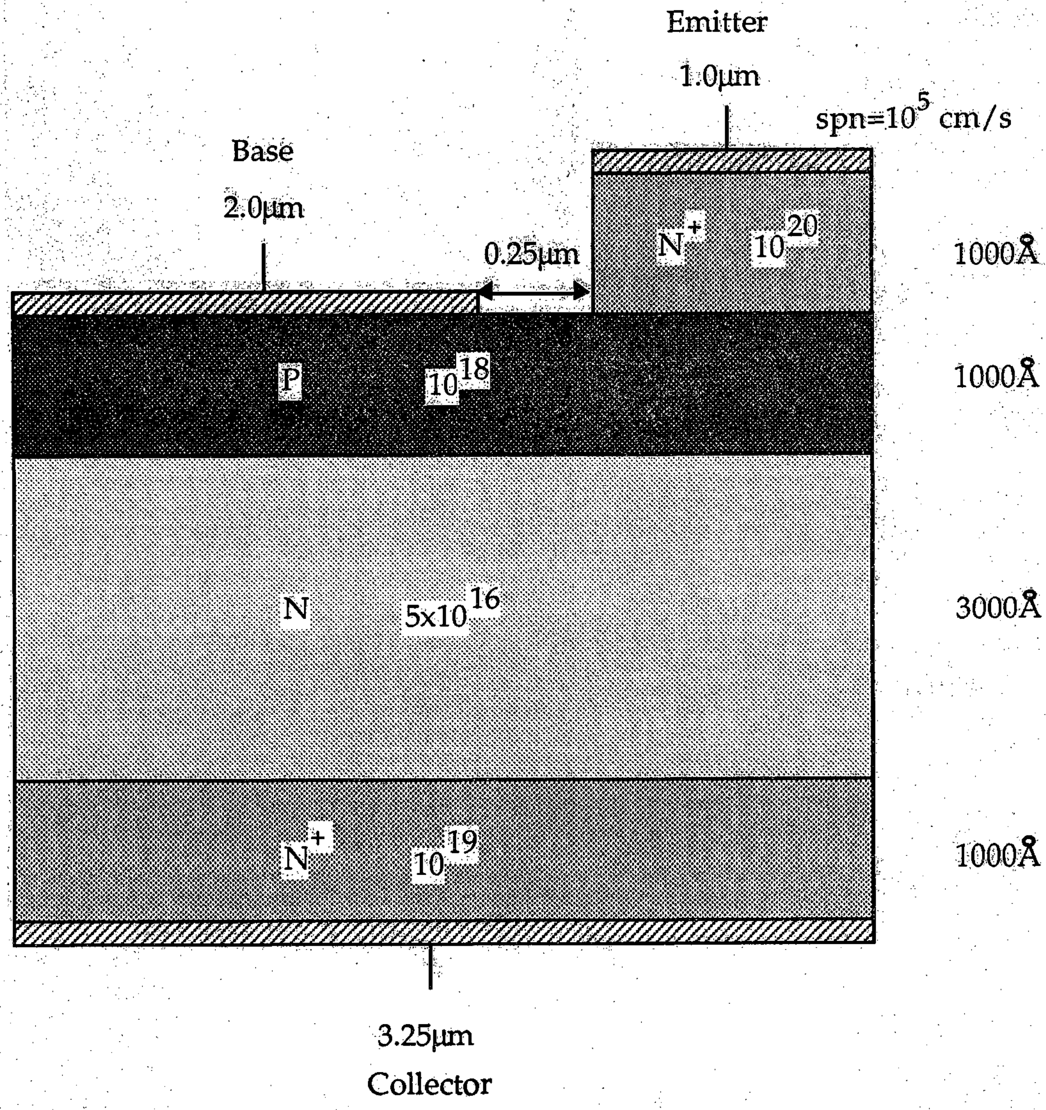

Figure 4.1 Conventional silicon bipolar transistor device structure.

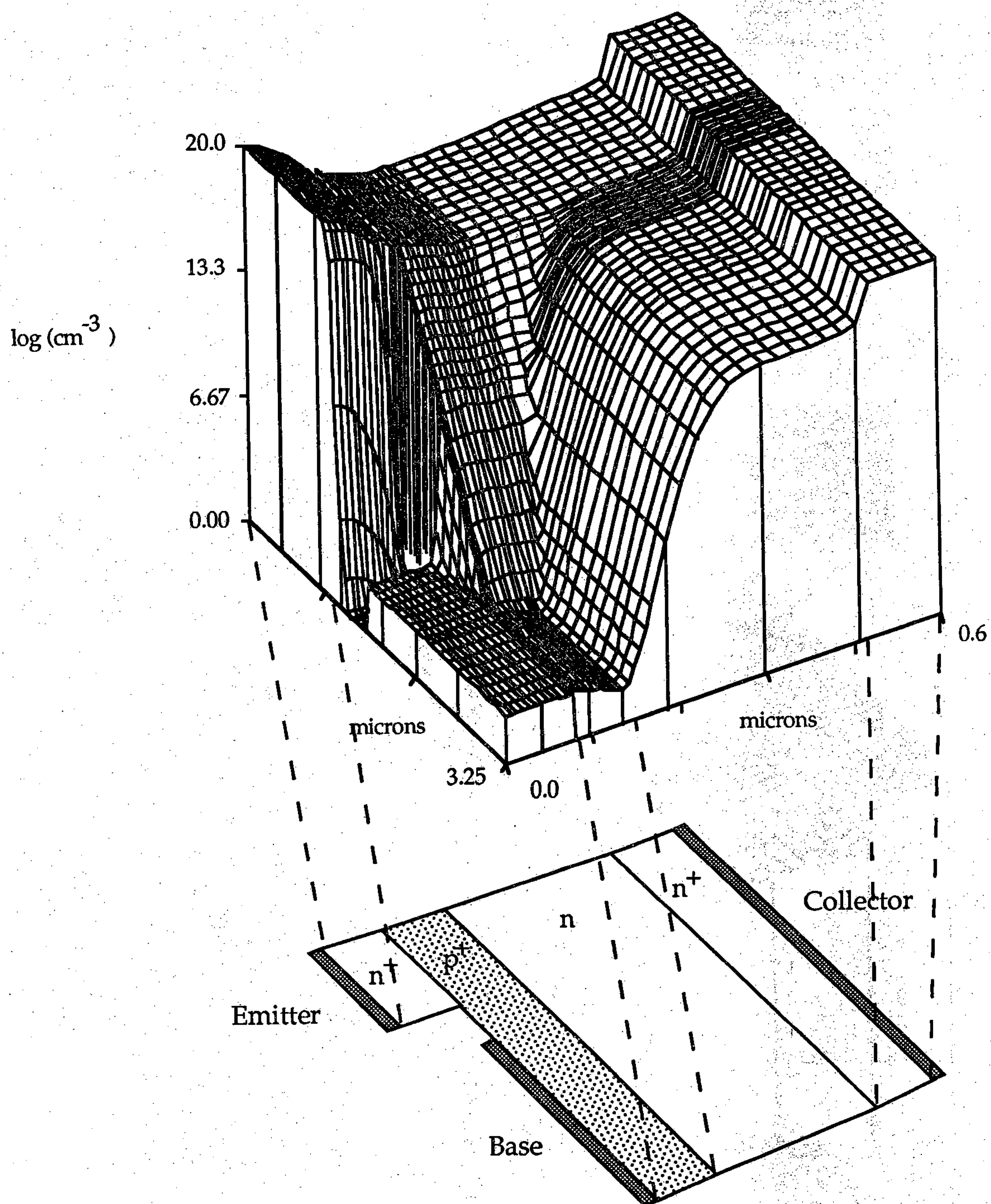

Figure 4.2 Electron concentration in the conventional silicon BJT at a bias of V_{BE} = 0.9 volt, V_{CE} = 1.0 volt.

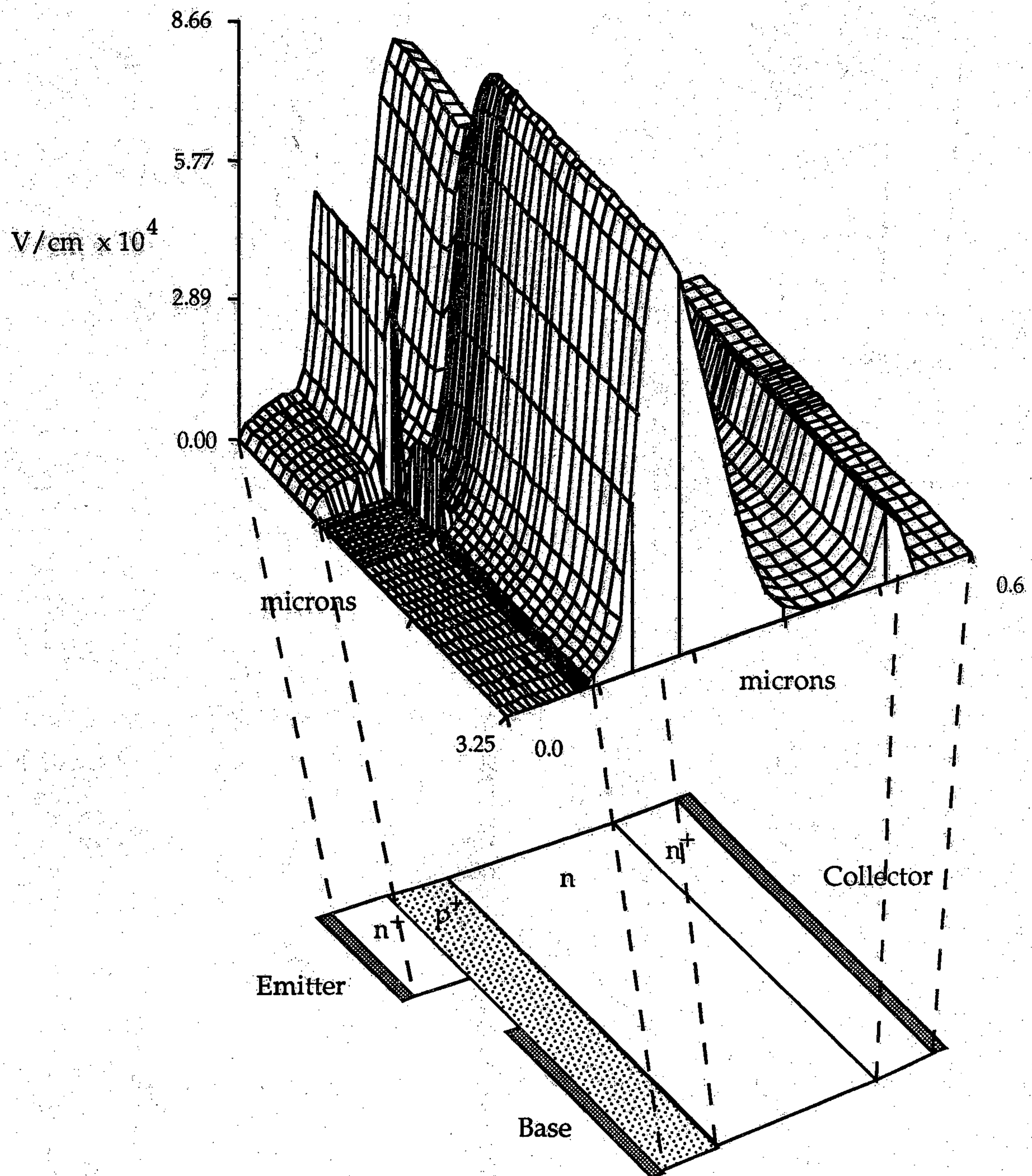

Figure 4.3 Electric field magnitude at V_{BE} = 0.9 volt, V_{CE} = 1.0 volt.

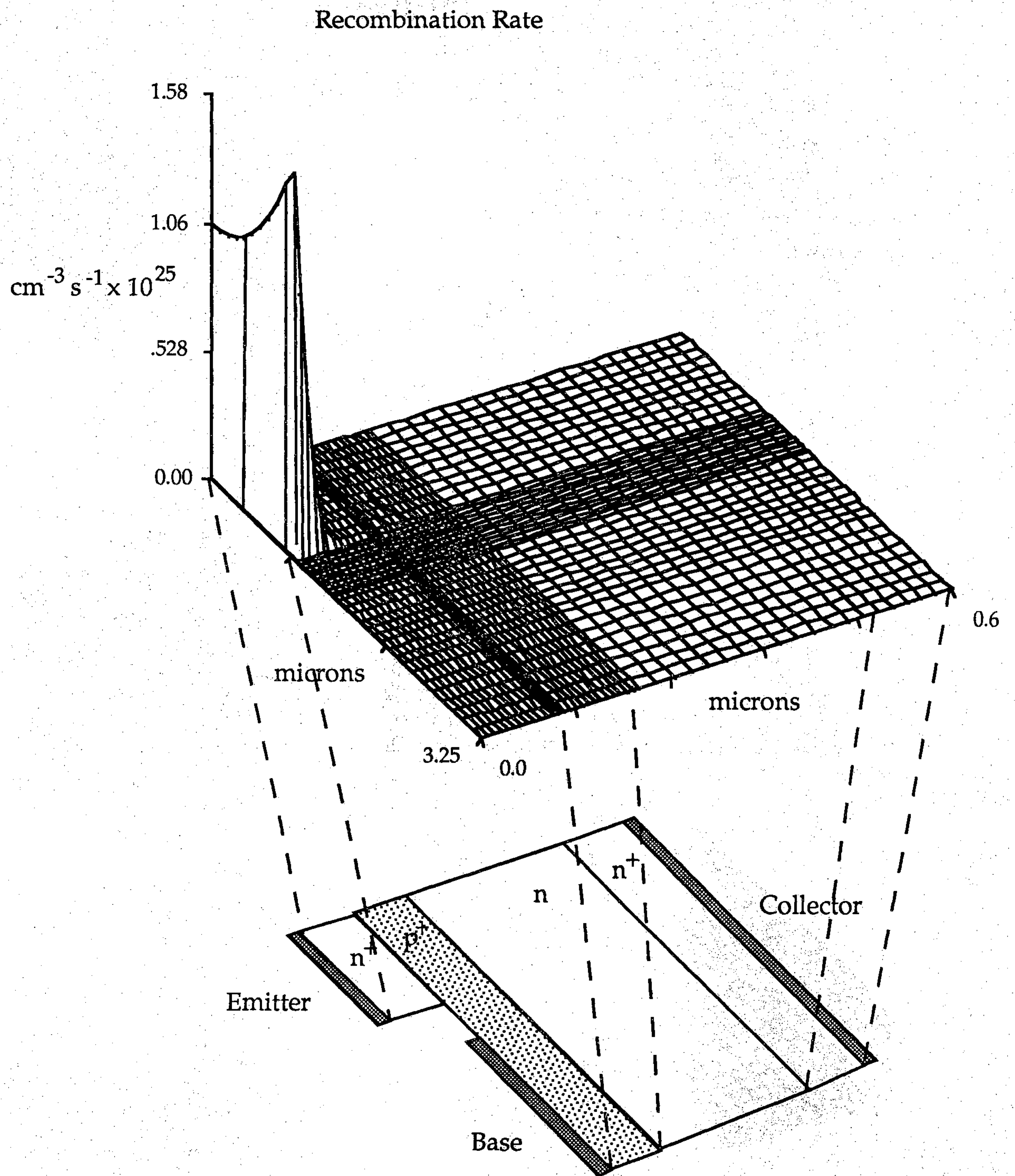

Figure 4.4 Recombination rate at V_{BE} = 0.9 volt, V_{CE} = 1.0 volt.

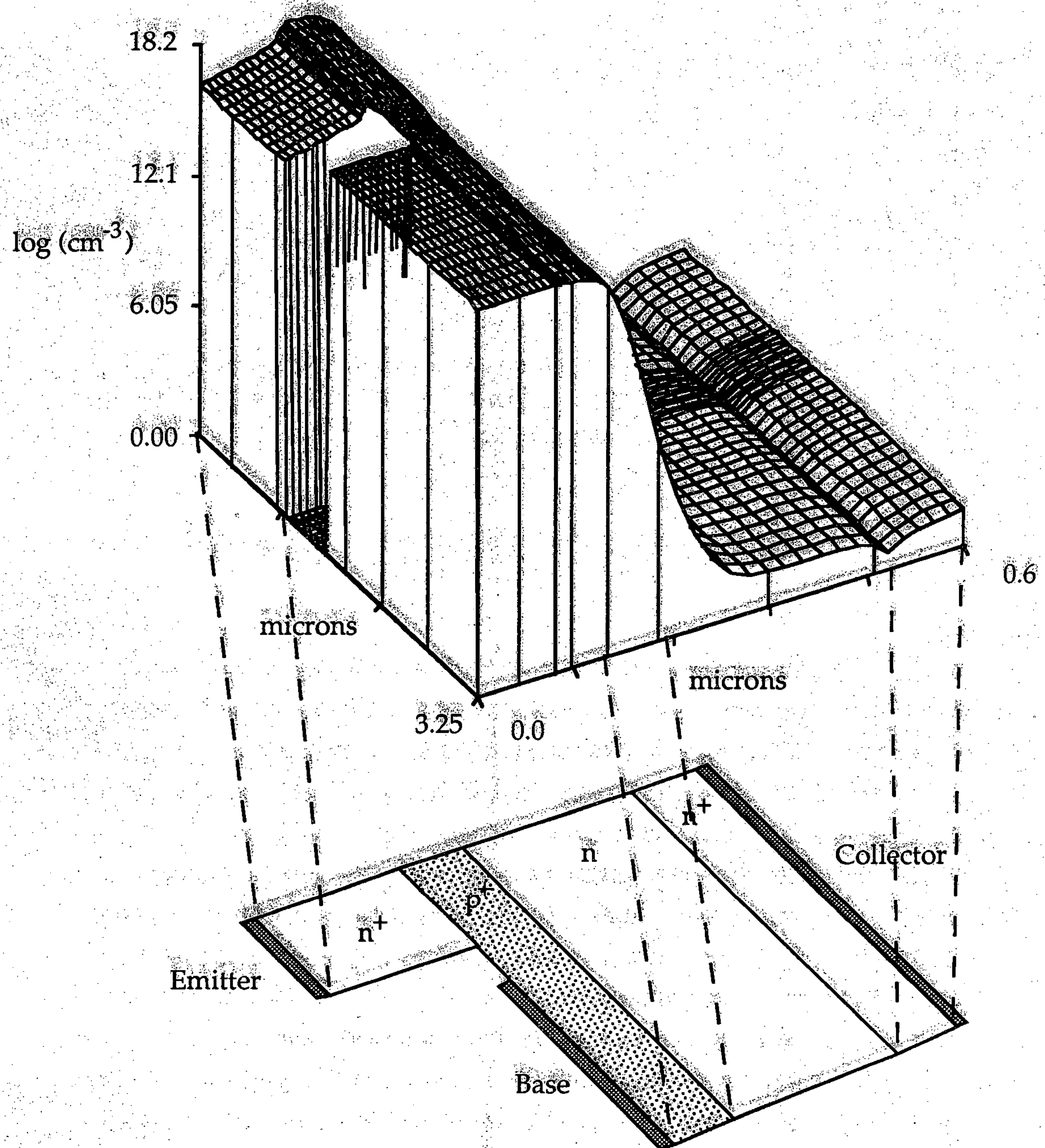

Figure 4.5 Hole concentration at V_{BE} = 0.9 volt, V_{CE} = 1.0 volt.

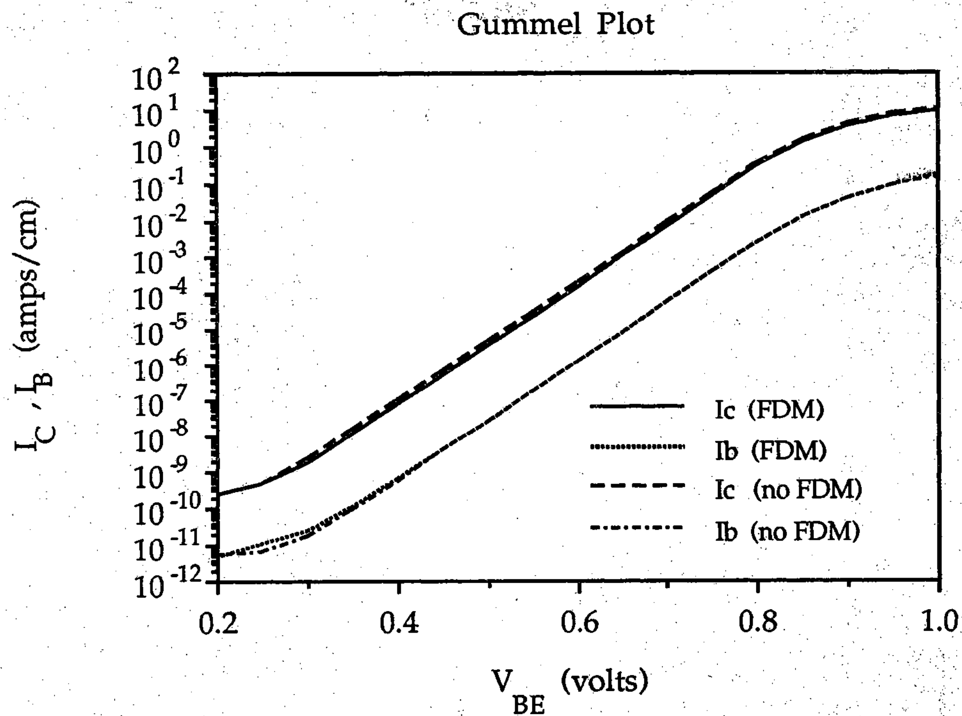

Figure 4.6 Conventional silicon bipolar transistor Gummel plot.

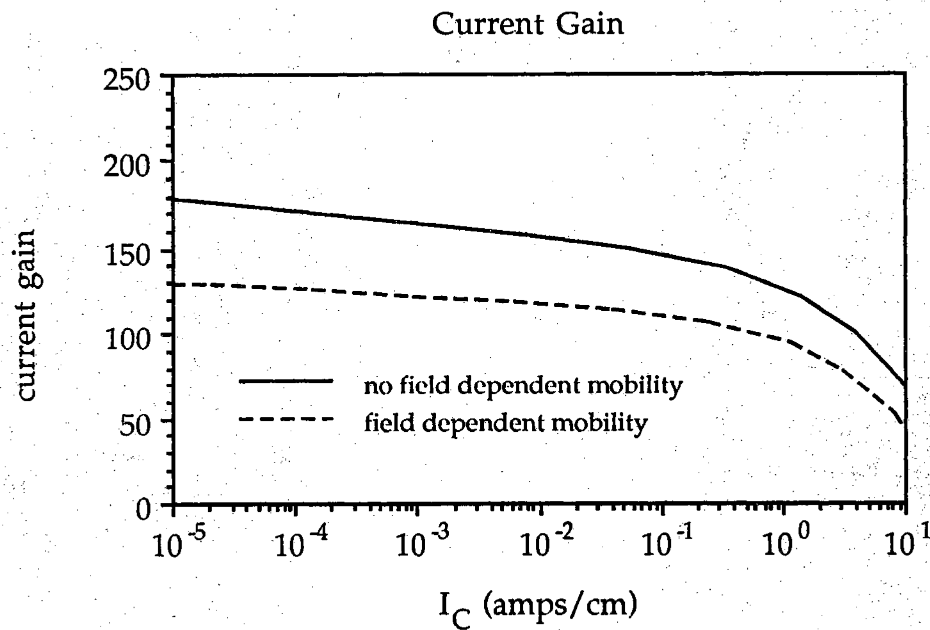

Figure 4.7 Current gain of the conventional silicon bipolar transistor.

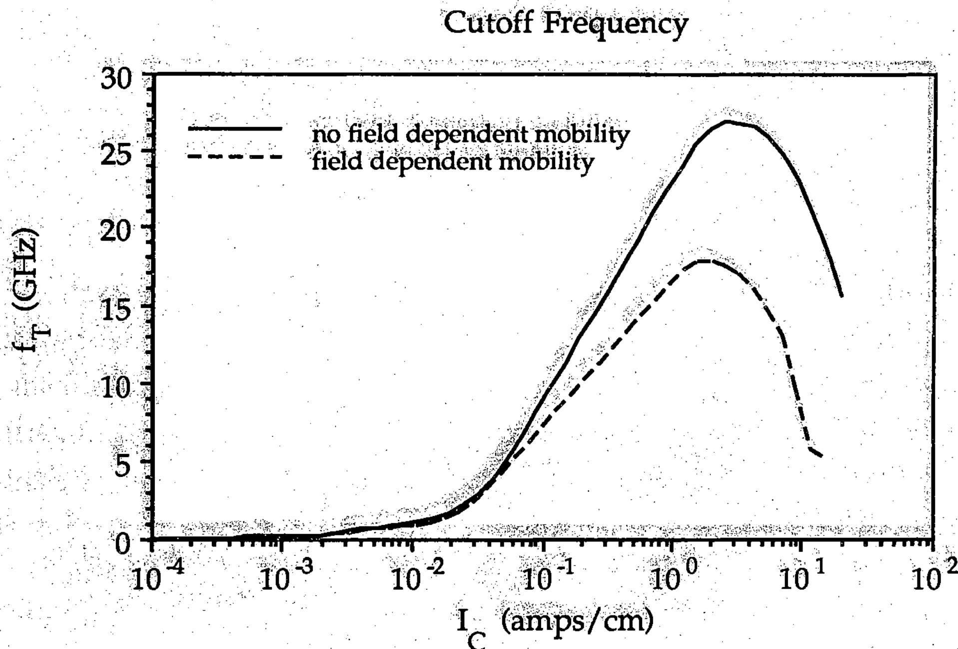

Figure 4.8 Unity gain cutoff frequency for the conventional transistor.

Figures 4.2 through 4.5 illustrate some of the internal device physics of the transistor. The bias of V_{CE}=1.0 volt, V_{BE}=0.9 volt corresponds to the bias at maximum f_T. A log plot of electron concentration (figure 4.2) shows lateral diffusion of electrons in the quasi-neutral base and depleted collector. The transistor is operating at a high injection level at this base-emitter bias. The insulator region is very effective in preventing carriers from crossing its boundaries. The electric field magnitude plot shows the electric field is strong in the base-collector depletion region. The collector-base depletion region in this device is over 2000 Å wide. The plot of recombination rate in the device (figure 4.4) reveals recombination is dominant at the emitter contact where holes are recombining. This is due to the hole recombination velocity set at the n-type contacts. Each of the devices in this section are modeled with a polysilicon emitter contact. A plot of hole concentration (figure 4.5) shows considerable injection of holes into the emitter. This should not happen in an HBT.

Terminal characteristics in the form of a Gummel plot, current gain versus collector current, and f_T versus collector current are shown in figures 4.6 through 4.8 respectively. The Gummel plot shows both I_B and I_C have a region of ideal current, and, at high bias, the current decreases due to high level injection. In the low bias region, some recombination is occurring in the base as evidenced by the small slope of the base current curve. Transistor current gain is behaves as it should. Current gain is relatively constant until high injection effects degrade the collector current and current gain. Simulations were run with and without field-dependent mobility. Field-dependent mobilities decrease both f_T and current gain. This is due to the smaller I_C which results from velocity saturation effects. Figure 4.8 shows f_T as a function of collector current. f_T reaches a maximum of 26.6 GHz without field-dependent mobility and 17.1 GHz with field-dependent mobility. This result is consistent with the internal physics since electrons traverse the collector-base space charge region, which is relatively wide, with lower velocities due to velocity saturation.

4.3. Advanced Silicon Bipolar Transistors

Sophisticated silicon bipolar transistors fabricated in modern research labs have very small base widths. The bipolar transistor in figure 4.9 [Sug90]

has a base width of only 450 Å, less than half that of the conventional transistor. This has a sizable impact on f_T. The base doping has to be increased in order to prevent punchthrough. But increasing the base doping will degrade current gain, so the emitter can be doped more heavily to offset this effect. The emitter junction is graded 32 nm with a complementary error function to reduce the junction capacitance. Again, the hole recombination velocity at the emitter contact is set to 10^5 cm/sec in order to model a polysilicon contact. The collector of this device is also heavily doped to prevent the Kirk effect, but not so heavily doped that junction breakdown occurs for V_{CE}=1 volt. This device was simulated with field-dependent mobility. Figures 4.10 through 4.12 characterize the performance of this device. f_T for this device is about 44 GHz, more than double that of the conventional transistor! This result is in good agreement with the perform-

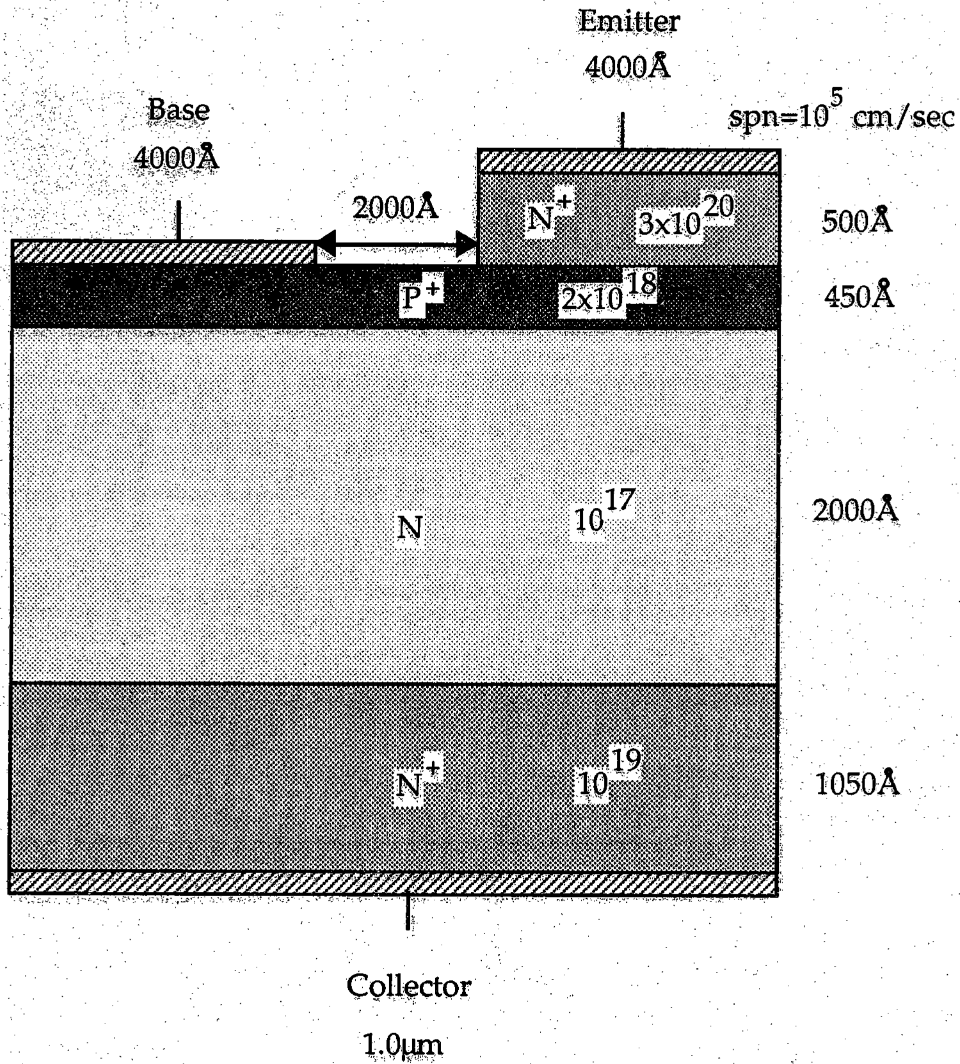

Figure 4.9 Advanced silicon bipolar transistor device structure.

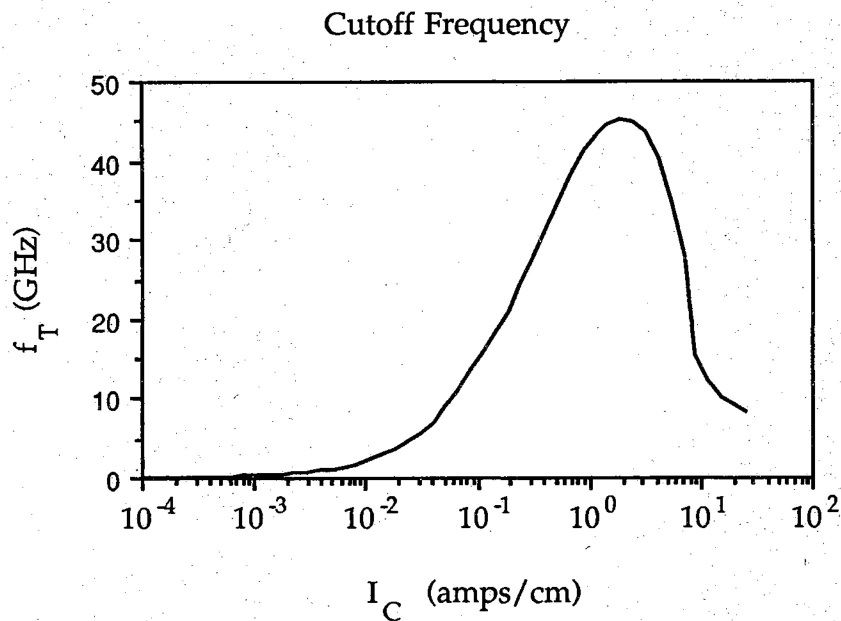

Figure 4.10 Unity gain cutoff frequency for the advanced bipolar transistor.

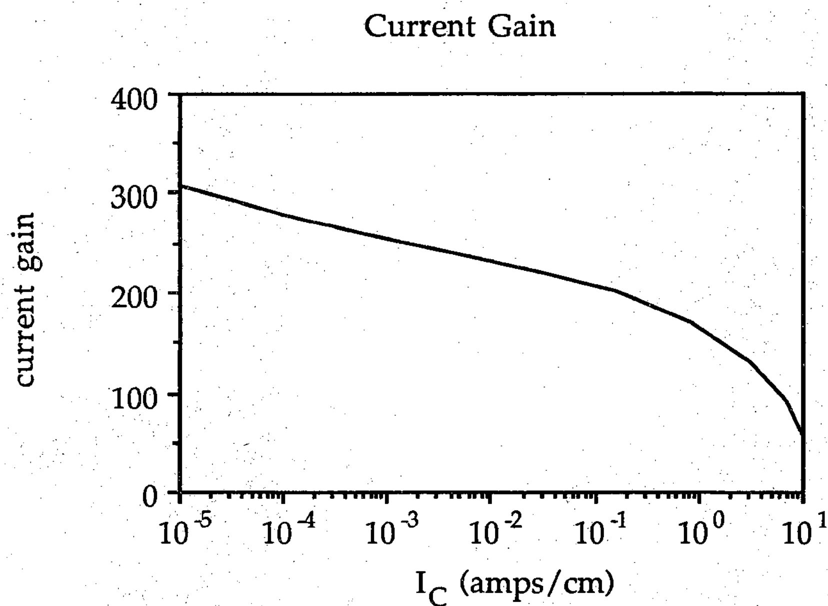

Figure 4.11 Current gain of the advanced silicon bipolar transistor.

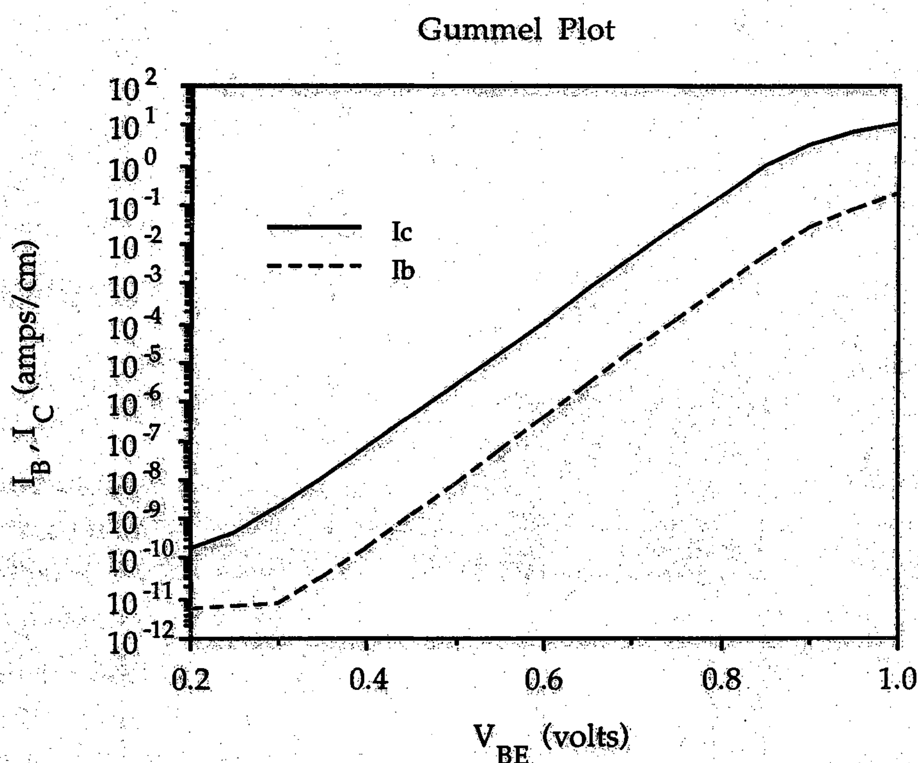

Figure 4.12 Gummel plot for the advanced silicon bipolar transistor .

ance of similar devices presented in [Sug89,Cra90]. The large difference in f_T is accountable in the smaller base width and heavier collector doping of the advanced silicon BJT. The current gain of this transistor falls off rapidly at high bias due to current crowding effects. Improvements are limited for silicon devices with f_T's approaching 50 GHz due to constraints imposed by base resistance, breakdown, and base punchthrough. Before proposing possible improvements to the device, analyses of the delay components in advanced bipolar transistors must be studied (section 4.6).

4.4. Conventional SiGe HBT's

The first modern Si/SiGe HBT's were fabricated about four years ago [Pat88,Tem88,Tat88]. Attempts to fabricate Si/SiGe HBT's prior to 1988 were

were not as successful because of the relatively immature strained layer HBT growth technology. However, the HBT's referenced above displayed advantages of the heterojunction such as higher collector currents than silicon devices at the same bias. Current gains for these HBT's were on the order of 10. The base of these early SiGe HBT's consisted of SiGe with a constant germanium mole fraction in the base, and base widths were on the order of 800 Å. In this section, the performance advantages of a SiGe HBT will be demonstrated. The transistor structure is given in figure 4.13, and the device is similar to the advanced silicon BJT. The emitter doping is lower than that of the silicon BJT (10^{20} cm^{-3} versus $3x10^{20}$ cm^{-3}), and the base has a constant germanium mole fraction of 8%. Carrier lifetimes in the SiGe base are set to 10^{-7} seconds (silicon lifetimes are 10^{-6} seconds). Carrier lifetimes in SiGe are believed to be smaller than silicon carrier lifetimes. Although lifetimes are somewhat doping dependent, the values quoted above are used in all of the simulations in this chapter independent of doping. The reason for this is lack of a simple model for carrier lifetimes in heavily doped material.

Again, the device was simulated with field-dependent mobility. The fraction of bandgap difference in the conduction band (DECFRC) is specified to be 15%. Figures 4.14 through 4.17 summarize device performance. Looking at the SiGe HBT Gummel plot, two important features stand out. First, there is substantial recombination in the base at low bias, and second, I_C is nearly two orders of magnitude higher than that of the advanced silicon BJT for the same V_{BE} bias. Current gain is substantially enhanced since no holes are back-injected into the emitter. Figure 4.15 displays low current gain for low bias due to the recombination in the base, and the Kirk effect lowers I_C and thus current gain at high biases. Maximum f_T is over 61 GHz for this device, about 17 GHz higher than for the advanced silicon BJT. Figure 4.17 illustrates the reduction of hole injection into the emitter due to the heterojunction (compare to 4.5). Although V_{BE} is different for these two hole concentration plots, I_C is about the same. Less hole back injection translates to more current gain for the same I_C. The superior injection properties of the heterojunction have been demonstrated one more time.

Conventional SiGe Bipolar Transistor

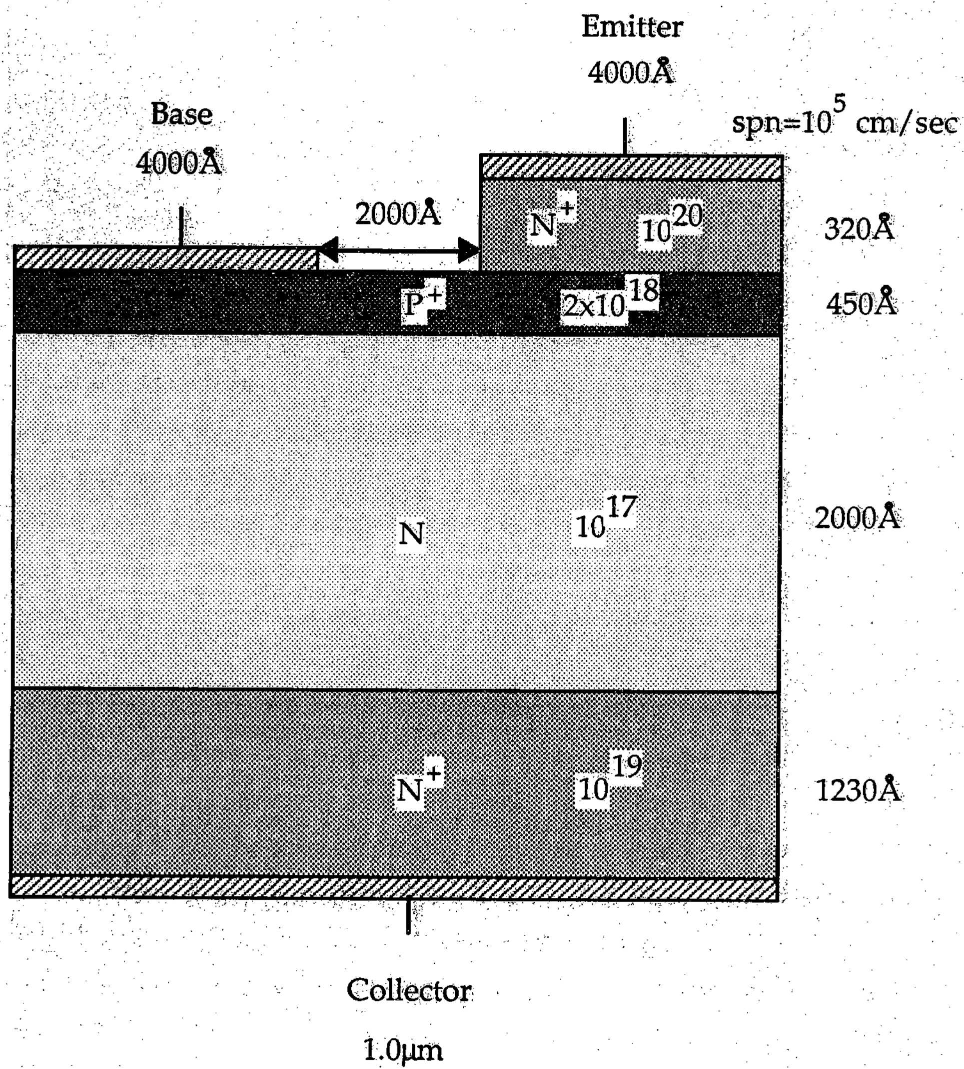

Figure 4.13 Conventional SiGe HBT device structure.

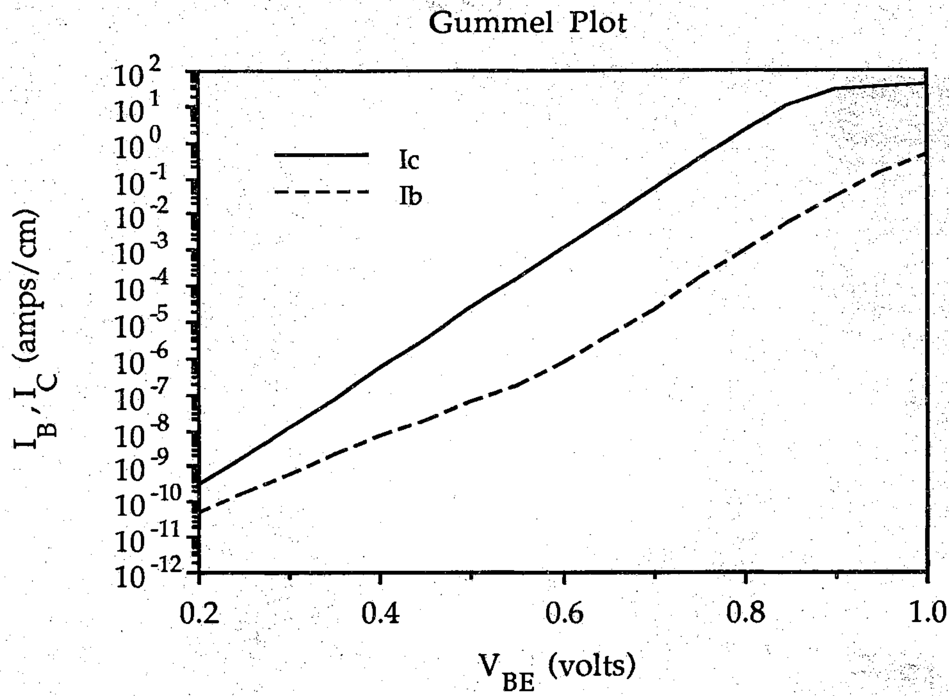

Figure 4.14 Conventional SiGe HBT Gummel plot.

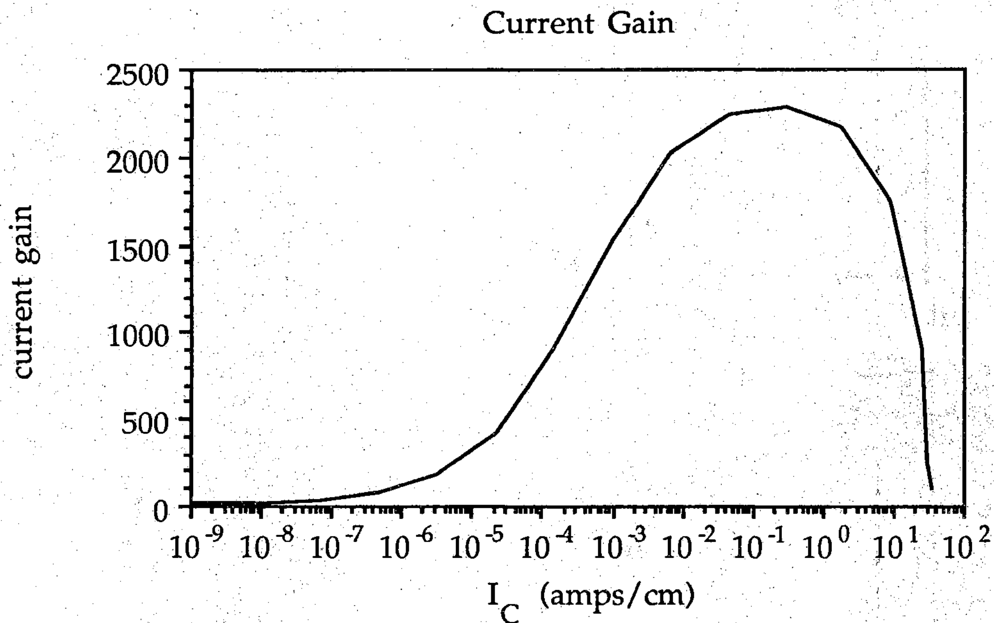

Figure 4.15 Current gain of the conventional SiGe HBT.

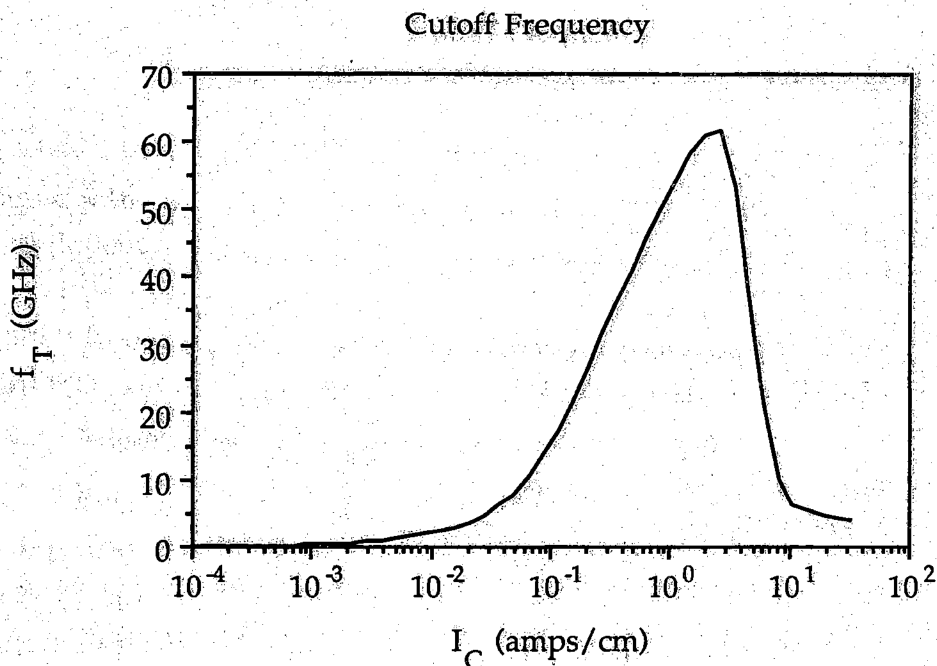

Figure 4.16 Cutoff frequency of the conventional SiGe HBT.

4.5. Advanced SiGe HBT's

Very high performance SiGe HBT's have been fabricated recently by a group from IBM [Pat90]. f_T's of 75 GHz were reported for these devices. The devices have a graded bandgap base formed by ultrahigh-vacuum/chemical vapor deposition (UHV/CVD) low-temperature epitaxy [Mey86]. Bandgap grading in the base reduces the transit time of electrons across the neutral base because a built-in electric field accelerates the electrons. A device very similar to that presented in [Pat90] (figure 4.18) was simulated using PUPHS2D with field-dependent mobility. The 450Å base has a uniform doping concentration of $2x10^{18}$ cm^{-3}, and the germanium concentration in the base is linearly graded from 0 percent at the emitter-base junction to 8 percent at the collector-base junction. The germanium concentration is linearly graded 300Å into the

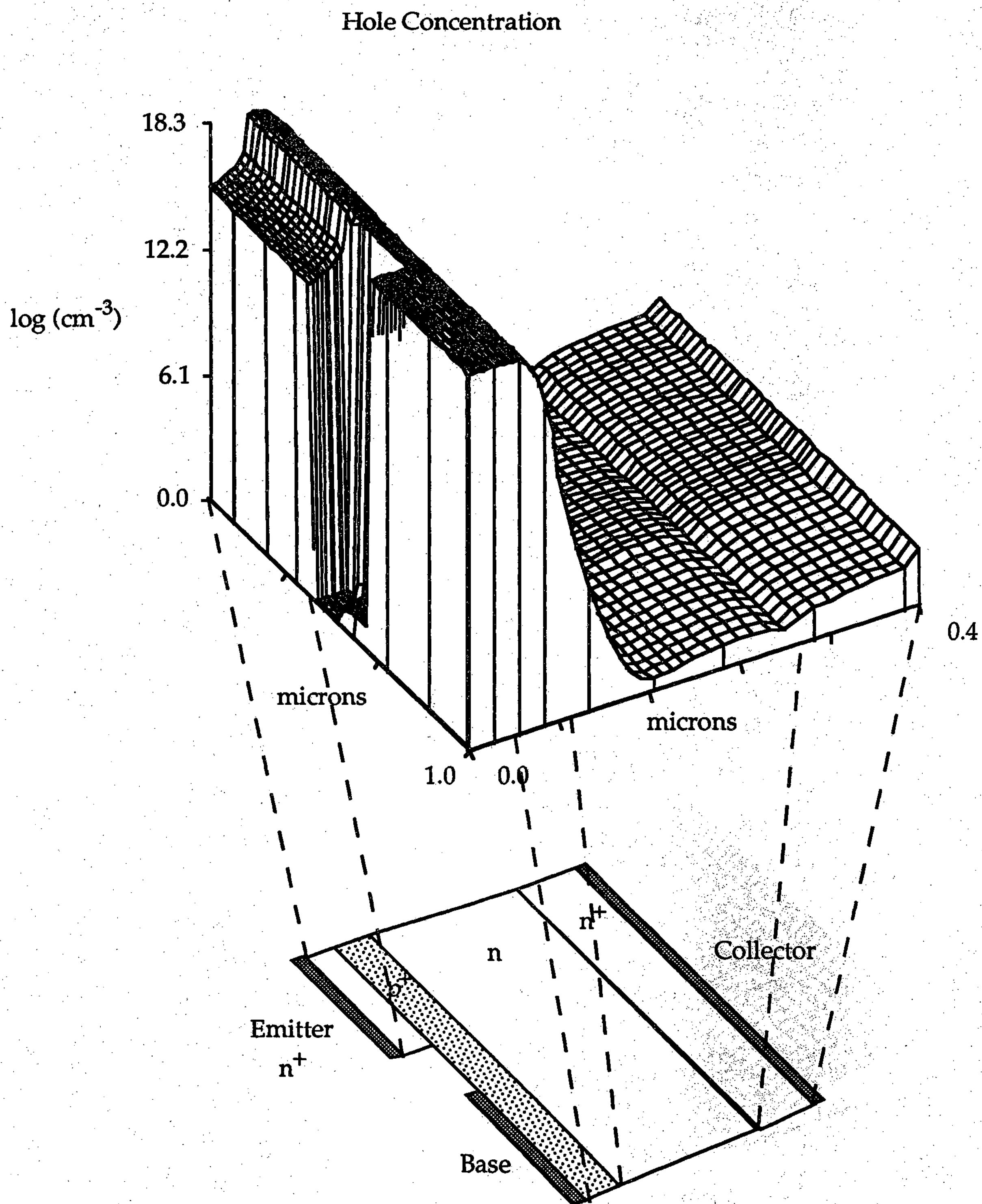

Figure 4.17 Hole Concentration in the conventional SiGe HBT at V_{CE}=1V, V_{BE}=0.8V.

collector so that electrons do not encounter a conduction band barrier. Grading the base creates a drift field of over 20kV/cm. The emitter has a complementary error function doping profile with a peak concentration of 3×10^{20} cm^{-3}. The collector is heavily doped at 6×10^{17} cm^{-3}. The high collector doping suppresses the Kirk effect but reduces the base-collector breakdown voltage of the device (a BV_{CE0} of 2.0 V was reported by Patton).Hole recombination velocity at the emitter contact is set to 10^5 cm/second in order to model a polysilicon contact.

Figures 4.19 through 4.21 summarize the performance of the graded base SiGe HBT. Some recombination in the base at low bias is evident from the Gummel plot. The current gain is not as high as the SiGe HBT without the graded base. Two contributing factors to the lower current gain are the higher average bandgap in the graded base device, and holes do not encounter a large abrupt barrier in graded base structures. f_T for this device is over 80 GHz. Patton reported a measured value of 75 GHz for a similar device [Pat90]. Lower base resistance can be traded for decreases in current gain and f_T, depending on the application of the device. This device represents the fastest transistor to date fabricated in a SiGe process.

4.6. Future Microwave Bipolar Transistors

Design constraints imposed by punchthrough, base resistance, the Kirk effect, and junction breakdown limit the performance of bipolar transistors. The unity gain cutoff frequency and total emitter to collector carrier transit time (τ_{EC}) in a bipolar transistor are given by [Uga89]:

$$f_T = \frac{1}{2\pi\,\tau_{EC}} \tag{4.1}$$

$$\tau_{EC} = \tau_E + \tau_{EB} + \tau_B + \tau_{BC} + \tau_C \tag{4.2}$$

where τ_E is the hole charge storage time in the emitter, τ_{EB} is the emitter-base junction capacitance charging time, τ_B is the neutral base transit time, τ_{BC} is the base-collector junction charging time, and τ_C is the collector delay time. Each of the five delay components in (4.2) can be calculated in order to determine the maximum delay component in a device using (4.3) - (4.7):

Advanced SiGe Bipolar Transistor

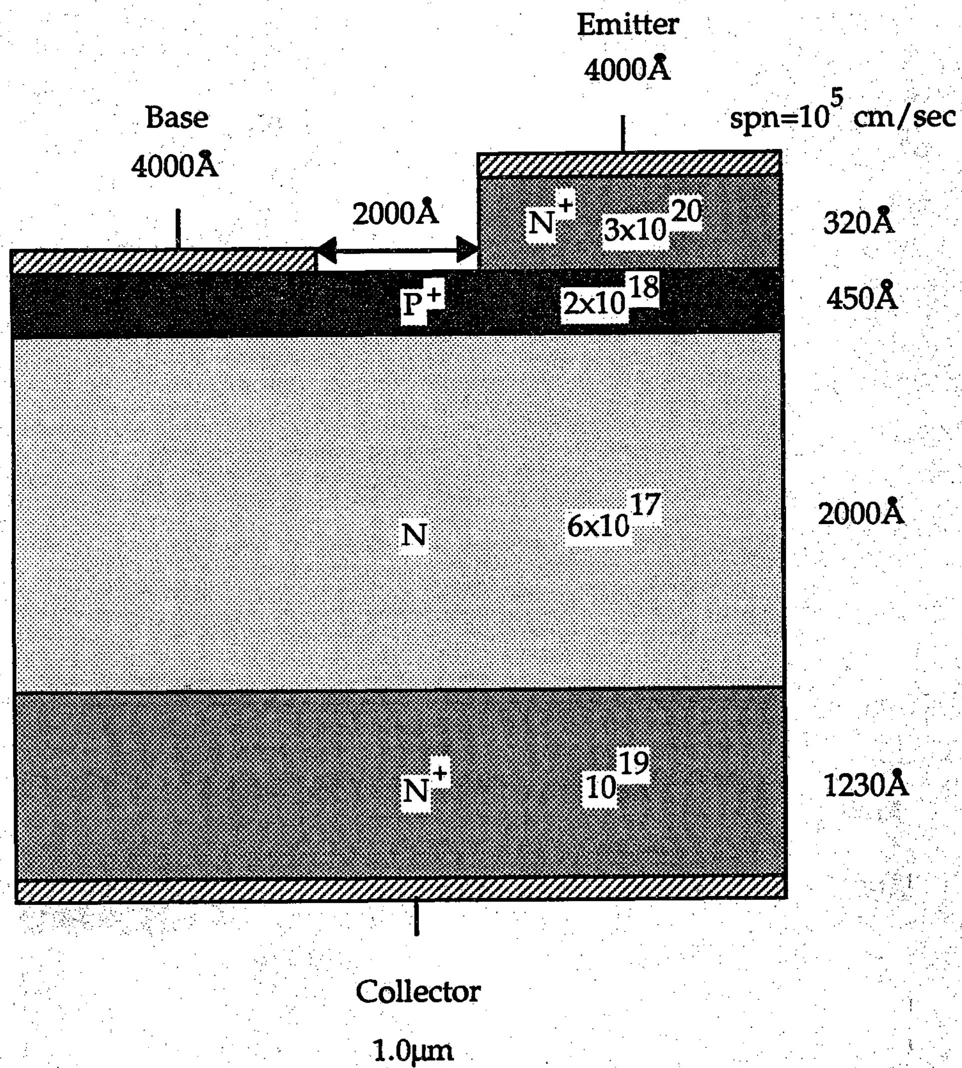

Figure 4.18 Graded base SiGe HBT device structure.

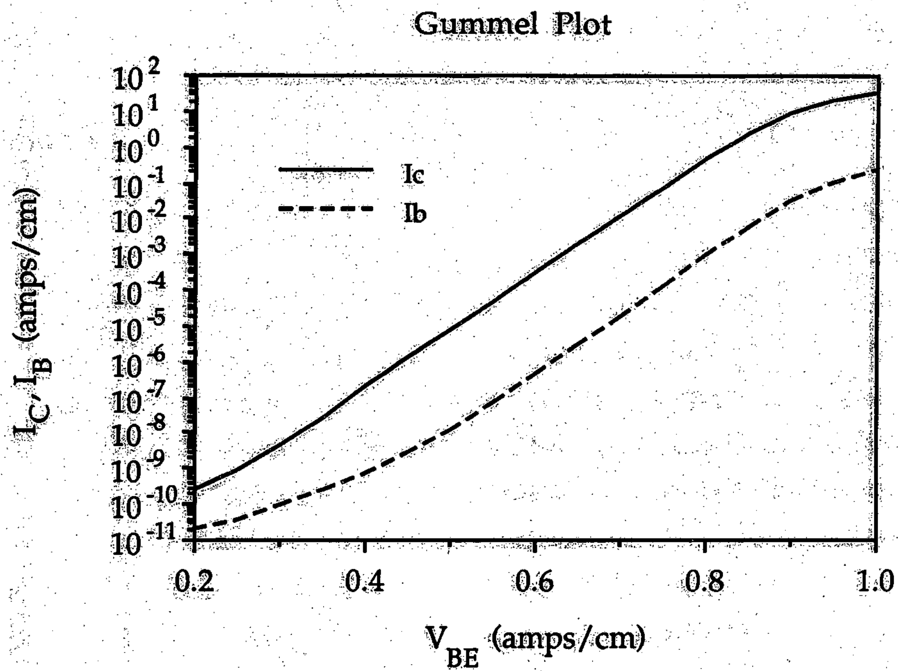

Figure 4.19 Gummel plot for the graded base SiGe HBT.

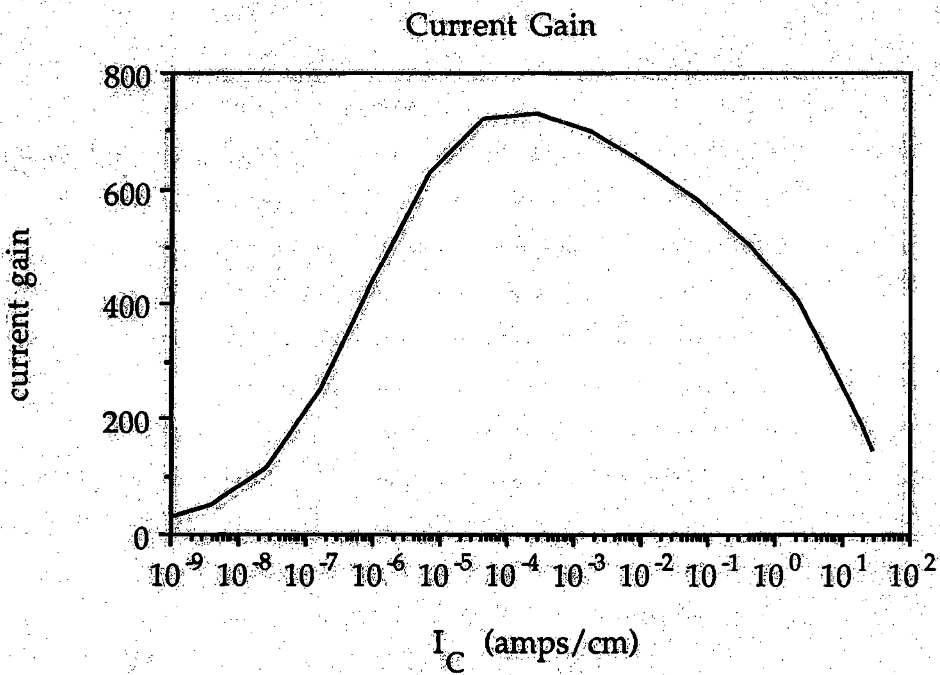

Figure 4.20 Current gain of the graded base SiGe HBT.

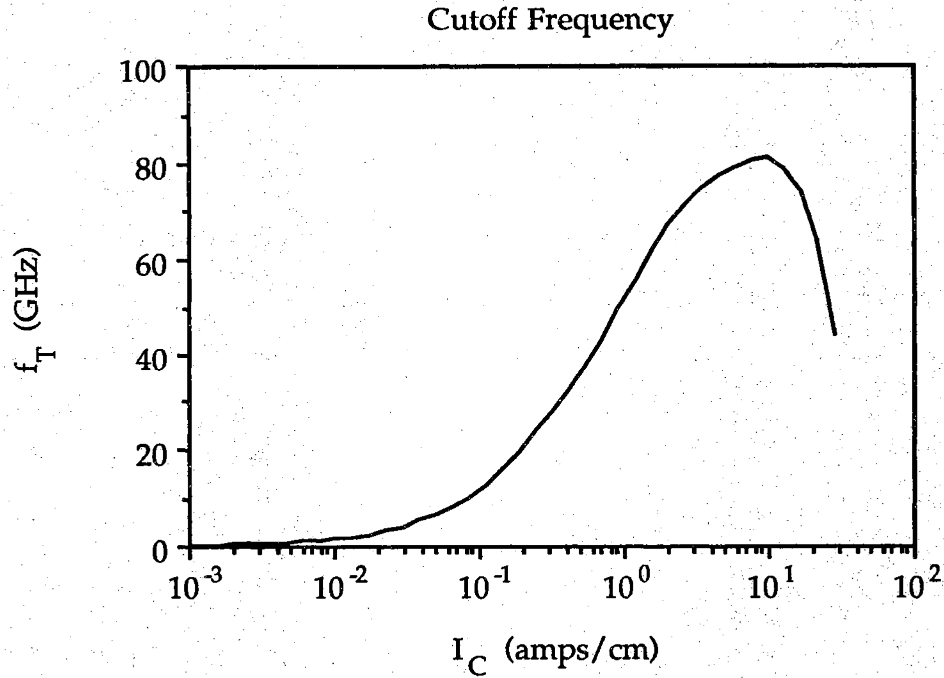

Figure 4.21 Cutoff frequency data for the graded base SiGe HBT.

$$\tau_E = \frac{\partial Q_E}{\partial J_C} \approx \frac{1}{\beta}\left(\frac{W_E^2}{2D_p}\right) \tag{4.3}$$

$$\tau_{EB} = r_e(C_e + C_c + C_p) \approx \frac{kT}{qI_E}(C_\pi + C_\mu) \tag{4.4}$$

$$\tau_B = \int_0^{W_B} \frac{dx}{v(x)} \tag{4.5}$$

$$\tau_{BC} = r_c C_c = \frac{r_c \varepsilon_s}{W_{BC}} \approx \frac{kT}{qI_C} L_C \sqrt{\frac{q\varepsilon_s N_A N_D}{2(N_A + N_D)}} \left(V_{bi} + V_{CB} - \frac{2kT}{q}\right)^{-1/2} \tag{4.6}$$

$$\tau_C \approx \frac{W_C}{2v_s} \tag{4.7}$$

Equations (4.4) - (4.7) are from [Sze81]. In (4.3) - (4.7), r is resistance (Ω - cm), C is capacitance (F/cm), L is length (cm), and v(x) is the electron velocity in the base. Subscripts e, c, and p in (4.4) refer to the emitter, base, and additional parasitics. W_B and W_C are the widths of the neutral base and the depleted collector, respectively. Values for v(x), C_π, C_μ, I_E, and I_C were calculated by PUPHS2D, and the rest of the data can be gathered from the device structures. The approximation of τ_E in (4.3) is only valid for uniformly doped emitters, however it will be used to give a rough estimate. τ_C was calculated using a method developed by Laux [Lau90]. Widths of the neutral base and depleted collector were estimated from the electric field profile in the device for a cross section through the center of the emitter. Integration of the electron velocity profile through this cross section determines the carrier transit times. τ_C is the collector delay time which is actually only a fraction of the collector transit time since an image charge forms at the collector contact as the electron sweeps across the collector space-charge region. The approximation given in (4.7) for τ_C agrees fairly well with Laux's method, however, his method should be more accurate.

Table 4.1 summarizes calculations for the delay components in the advanced silicon BJT and graded base SiGe HBT. Recall the maximum cutoff frequency of the advanced silicon bipolar transistor transistor is 43.8 GHz, which translates to a total transit time of 3.64 ps. The total estimated τ_{EC} is 3.23 ps, corresponding to an f_T of 49 GHz. This is in good agreement with the value calculated by PUPHS2D. The emitter-base junction charging time is the dominant source of delay in this particular device, and the intrinsic base and collector delays are also significant. For the graded base SiGe HBT, the emitter base junction charging time is also large compared to the other delay components. A lightly doped spacer can be put in the emitter-base junction to reduce the junction capacitance as well as forward tunneling [Tan89]. The results of a simulation study by Ugajin [Uga89] show the maximum delay components are the base and collector transit delays. If this is the case, devices must be optimized by either reducing the widths of these regions or increasing the carrier velocities in them. Significant reduction of delays in silicon devices is unlikely due to limitations imposed by base resistance and punchthrough. In SiGe HBT's, the transit times may be reduced by

introducing larger built in fields in the base and optimizing the collector design.

Table 4.1 Delay components for advanced transistors.

τ (ps)	Silicon BJT	SiGe HBT
τ_E	0.07	0.00
τ_{EB}	1.96	1.10
τ_B	0.6	0.5
τ_{BC}	0.05	0.05
τ_C	0.55	0.20
τ_{EC}	3.23	1.85
f_T	49 GHz	86 GHz

4.7. Summary

PUPHS2D was shown to be an accurate computer simulation program (with field-dependent mobility modeled) by comparison with the simulation results of Ugajin [Uga89]. Simulation results for both silicon bipolar transistors and SiGe heterojunction bipolar transistors were presented in this chapter. Conventional and advanced devices were studied. Simulation results for both silicon and SiGe bipolar transistors are in good agreement

with measured results. Simulation of an advanced silicon bipolar transistor gives an f_T of about 44 GHz. SiGe HBT's with a constant germanium concentration in the base have very large current gains and higher f_T's than silicon devices. A graded base SiGe heterojunction bipolar transistor similar to that of Patton *et al.* [Pat90] was simulated, and an f_T of slightly over 80 GHz was predicted by PUPHS2D. The measured value of f_T for this device is reported to be 75 GHz. Delay components for silicon and SiGe transistors were analyzed in order to find limiting performance factors of the devices. Design improvements were proposed based on these results. The future for SiGe HBT's in microwave applications is very promising. Design constraints such as base resistance limit the practical application of silicon devices. The base doping in a silicon BJT cannot be too high or current gain will be low. Many limitations of silicon devices can be overcome with a heterojunction transistor, including base resistance and current gain.

CHAPTER 5: SUMMARY AND RECOMMENDATIONS

5.1. Summary

The main objective of this research was to develop an existing two-dimensional AlGaAs/GaAs HBT simulation tool into an accurate model for the simulation of Si/SiGe HBT's. Additional goals were to assess the model's accuracy by comparison with measured results; to assess the performance of SiGe HBT's in microwave applications and compare to scaled silicon devices; and to explore various design options for SiGe HBT's. Accomplishing the primary goal required a thorough study of the material parameters for both silicon and strained $Si_{1-x}Ge_x$ alloys. This study revealed silicon is a very well characterized material. However, the characterization of SiGe strained layers on Si(100) substrates is in its infancy in comparison. Relatively accurate material parameters for strained SiGe layers grown on Si(100) have been incorporated into PUPHS2D. The carrier mobility models in strained SiGe are very conservative. Mobility enhancements due to strain have not been modeled. As more studies are performed on the electrical properties of SiGe strained layers, the program can be easily modified to include the latest findings.

Field-dependent mobility has been added to the code in order to model the effects of velocity saturation in devices. An uncoupled technique was used to implement field-dependent mobility (terms were not added to the Jacobi matrix). The uncoupled technique converges quickly, and field-dependent mobility models for new material systems are easy to include in PUPHS2D. The accuracy of the field-dependent mobility model was demonstrated in chapters 3 and 4. HBT's and diodes were tested using field-dependent mobility, and the results were consistent with internal device physics. A field-dependent mobility model was added for the AlGaAs/GaAs material system as well.

The PUPHS2D code structure has been modified in order to accommodate additional materials systems. A separate file was created in which all of the material dependent subroutines are stored. Such a file exists for each different material system. Only one of the material files must be compiled with PUPHS2D. Procedures for the addition of new material systems have been discussed, and adding a new material system is now quite easy. Several bugs have been removed from earlier versions of the program. One of these was a normalization error in the current calculation subroutine for bipolar transistors (TRCURR). PUPHS2D has been thoroughly tested and is an accurate tool for the simulation of HBT's.

The simulation results of chapter 4 are very encouraging for the future of SiGe HBT's. Unity gain cutoff frequency of over 80 GHz was demonstrated for a graded base SiGe HBT. This is consistent with Patton's results [Pat90] for a similar transistor. The fastest room temperature silicon transistors have demonstrated f_T's of about 50 GHz. PUPHS2D simulations predict f_T's of nearly 45 GHz for silicon transistors. Improvements for silicon devices are limited by fundamental properties of the semiconductor such as base resistance. SiGe HBT's have a more promising future. SiGe HBT's enjoy many of the processing advantages of silicon devices, which makes them more attractive than III-V HBT's. Low temperature operation has not been investigated in this work due to the lack of accurate SiGe parameters at low temperatures. Enhanced mobilities have been reported in SiGe strained layers at low temperatures, and transistor performance has shown improvement for low temperature operation [Cra90]. This subject may attract more attention in the future and could make a separate thesis itself.

5.2. Recommendations

PUPHS2D has been proven to be an accurate computer model for the simulation of heterojunction bipolar transistors, but there are several possible improvements which could be made to the program. A major improvement would be to replace the LINPACK solver with an iterative solver. LINPACK solves matrix equations by direct inversion of an extremely large matrix which requires an enormous amount of memory. This makes it impractical to run PUPHS2D on smaller computers which do not have large memory

capacities. Iterative techniques have been proven to reduce the amount of memory required to run device simulation programs. Research of an iterative solver at Purdue has shown the memory can be reduced by a factor of ten for devices with a large number of nodes. Implementation of an iterative solver into PUPHS2D would make it practical to run on smaller computers, or, for large systems, many more nodes could be used for better resolution.

The formulation for modeling nonrectangular geometries can cause convergence problems. PUPHS2D could be rewritten such that arbitrary geometries are defined in the input deck. This would require a completely new node indexing scheme and would be a major change to the program. Devices would have to be thoroughly checked for boundaries due to the possible nonrectangular geometries involved.

The input deck in PUPHS2D cannot be considered "user-friendly". Many of the material parameters are hardware into the code. The program could be developed into a more user-friendly tool if many additional options were added to the input deck. For example, the program could read in user-defined material material parameters if appropriate changes were made.

Several improvements in the device physics could be made in the transient analysis routines and mobility models. Amitava Das has been working on the development and optimization of the transient routines, and his work is nearly complete. Transient analysis will include resistors external to the device. This is how transient analyses are performed in laboratories. The majority and minority carrier mobilities are assumed to be the same, although they are believed to be different (see section 2.6). Very conservative SiGe mobility models are used. The most accurate strained layer mobility model must take into account the different mobilities parallel and perpendicular to the growth of the strained layer. One final possible improvement is the implementation of a nonlocalized energy balance equation in order to more accurately model high-field transport. Paul Dodd implemented a localized energy balance equation into PUPHS2D for GaAs [Dod89]. However, convergence was very slow, and he believed the problem could be stabilized by delocalization.

LIST OF REFERENCES

[Ahm86] N. Ahmad and V.K. Arora, *IEEE Trans. Elec. Dev.*, vol. ED-33, p. 1075, 1986.

[Ala86] J.A. del Alamo and R.M. Swanson, "Forward bias tunneling: A limitation to bipolar device scaling," *IEEE Elec. Dev. Lett.*, vol. EDL-7, pp. 629-631, 1986.

[Ala87] J.A. del Alamo and R.M. Swanson, "Measurement of steady-state minority-carrier transport parameters in heavily doped n-type silicon," *IEEE Trans. Elec. Dev.*, vol. ED-34, pp. 1580-1589, 1987.

[Aro82] N.D. Arora, J.R. Hauser and D.J. Roulston, "Electron and hole mobilities in silicon as a function of concentration and temperature," *IEEE Trans. Elec. Dev.*, vol. ED-29, no. 2, pp.292-295, 1982.

[Bac75] G. Baccarani and P. Ostoja, "Electron mobility empirically related to the phosphorous concentration in silicon," *Solid-State Electron.*, vol. 18, p. 579-580, 1975.

[Bar67] H.D. Barber, "Effective mass and intrinsic concentration in silicon," *Solid-State Electron.*, vol. 10, pp. 1039-1051, 1967.

[Bea84] J.C. Bean, L.C. Feldman, A.T. Fiory, S. Nakahara and I.K. Robinson, "Ge_xSi_{1-x}/Si strained layer superlattice growth by molecular beam epitaxy," *J. Vac. Sci. Technol.*, vol. 2a, no. 2, pp. 436-440, 1984.

[Bea88] R.E. Beaty, "A bias tunable monolithic microwave oscillator - the contiguous domain oscillator," Doctoral Thesis, Purdue University, Aug. 1988.

[Blu74] W. Bludau, A. Onton and W. Heinkle, "Temperature dependence of the bandgap of silicon," *J. Appl. Phys.*, vol. 45, no. 4, pp. 1846-1848, 1974.

[Bra58] R. Braunstein, A.R. Moore and F. Herman, "Intrinsic Optical absorption in germanium-silicon alloys," *Phys. Rev.*, vol. 109, no. 3, pp. 695-710, Feb. 1 1958.

[Can75] C. Canali, G. Majni, R, Minder and G. Ottaviani, "Electron and hole drift velocity measurements in silicon and their empirical relation to electric field and temperature," *IEEE Trans. Elec. Dev.*, vol. ED-22, pp. 1045-1047, 1975.

[Cau67] D.M. Caughy and R.E. Thomas, "Carrier mobilities in silicon empirically related to doping and field," *Proc. IEEE*, pp.2192-2193, Dec. 1967.

[Cho75] A.Y. Cho and J.R. Arthur, "Molecular beam epitaxy," *Prog. Solid State Chem.*, vol. 10, pt. 3, pp. 157-191, 1975.

[Coe80] R.W. Coen and R.S. Muller, "Velocity of surface carriers in inversion layers on silicon," *Solid State Electron.*, vol. 23, pp. 35-40, 1980.

[Cra90] E.F. Crabbe, G.L. Patton, J.M.C. Stork, J.H. Comfort, B.S. Meyerson and J.Y.-C. Sun, "Low temperature operation of Si and SiGe bipolar transistors," *Proc. IEDM 1990*, pp. 17-20.

[DAv79] D.C. D'Avanzo, M. Vanzi and R.W. Dutton, "One-dimensional semiconductor device analysis," (SEDAN), Report G-201-5, Stanford University, 1979.

[Dan80] L.M. Dang and M. Konaka, "A two-dimensional computer analysis of triode-like characteristics of short-channel MOSFET's," *IEEE Trans. Elec. Dev.*, vol. ED-27, pp. 1533-1539, 1980.

[DeM88] P.D. DeMoulin, "The physics and modeling of gallium arsenide solar cells," Doctoral Thesis, Purdue University, Jun. 1988.

[Din74] R. Dingle, W. Wiegmann and C.H. Henry, "Quantum states of confined carriers in very thin $Al_xGa_{1-x}As$-GaAs-$Al_xGa_{1-x}As$ heterostructures," *Phys. Rev. Lett.*, vol. 33, no. 14, pp. 827-830, 1974.

[Dod89] P.E. Dodd, "Simulation of Heterojunction Bipolar Transistors in Two Dimensions," MSEE Thesis, Purdue University, School of Electrical Engineering, West Lafayette, Indiana, December 1989.

[Dre55] G. Dresselhaus, A.F. Kip, H. Ku, G. Wagoner and S.M. Christian, "Cylclotron resonance in GeSi alloys," *Phys. Rev.*, vol. 100, no. 4, pp.1218-1219, Nov. 15 1955.

[Dup79] R.D. Dupuis, L.A. Moudy and P.D. Dapkus, "Preparation and properties of $Ga_{1-x}Al_xAs$-GaAs heterojunctions grown by metal-organic chemical vapor deposition," Gallium Arsenide and related compounds 1978, *Inst. Phys. Conf. Ser.*, vol. 45, pp. 1-9, 1979.

[Dzi77] J. Dziewior and W. Schmidt, "Auger coefficients for highly doped and highly excited silicon," *Appl. Phys. Lett.*, vol. 31, no. 5, pp. 346-348, 1977.

[Eng81] W.L. Engl and H. Dirks, "Models of physical parameters," In: Introduction to the Numerical Analysis of Semiconductor Devices and Integrated Circuits, pp. 42-46, Dublin: Boole Press, 1981.

[Fin76] D. Fink and R. Braunstein, "Determination of the conduction band effective masses of the germanium-silicon alloy by infrared cyclotron resonance," *Phys. Stat. Sol. (b)*, vol. 73, p.361-370, 1976.

[Fis89] S.E. Fischer *et al.*, "A 45 GHz Ge/Si heterojunction bipolar transistor fabricated with low temperature epi," in *IEDM Tech. Dig.*, Dec. 1989, pp. 890-892.

[Fos76] J.G. Fossum, "Computer-aided numerical analysis of solar cells," *Solid-State Electron.*, vol. 19, pp. 269-277, 1976.

[Fra83] A.F. Franz, G.A. Franz, S. Selberherr and P. Markowich, "The influence of various mobility models on the iteration process and solution of the basic semiconductor equations," *Proc. NASECODE III*, pp. 117-121, 1983.

[Gok70] B.V. Gokhale, "Numerical solutions for a one-dimensional silicon n-p-n transistor," *IEEE Trans. Elec. Dev.*, vol. ED-17, no. 8, pp. 594-602, 1970.

[Gra82] J.L. Gray, "Two-dimensional modeling of silicon solar cells," Purdue University, School of Electrical Engineering Tech. Rep. TR-EE 82-12, Aug. 1982.

[Han86a] W. Hansch and M. Miura-Mattausch, *J. Appl. Phys.*, vol. 60, p. 650, 1986.

[Han86b] W. Hansch and S. Selberherr, *IEEE Trans. Elec. Dev..*, vol. ED-34, pp. 1074-1078, 1986.

[Has63] H. Hasegawa, "Theory of cyclotron resonance in strained silicon crystals," *Phys. Rev.*, vol. 29, no. 3, p. 1029, 1963.

[Hei73] H.H. Heimeier, Zweidimensioanle numerische Losung eines nichtlinearen Randwertproblems am Beispiel des Transistors im stationaren Zustand. Dissertation, Technische Hochschule Aachen, 1973.

[Hel76] M.W. Heller, R.D. Nasby and R.T. Johnson, "Electrical transport properties of SiGe thermoelectric alloys doped with As, P, and As+P," *J. Appl. Phys.*, vol. 47, no. 9, Sept. 1976.

[Ish90] T. Ishibashi, O. Nakajima, H. Ito, S. Yamahata and Y. Matsouka, "Suppressed base-widening in AlGaAs/GaAs ballistic collection transistors," presented at the 48th Device Research Conference, Santa Barbara, Cailf., June 25-27, 1990.

[Iye89] S.S. Iyer, G.L. Patton, J.M.C. Stork, B.S. Meyerson and D.L. Harame, "Heterojunction bipolar transistors using Si-Ge alloys," *IEEE Trans. Elec. Dev.*, vol. 36, no. 10, pp. 2043-2064, Oct. 1989.

[Jac77] C. Jacoboni, C. Canali, G. Ottaviani and A.A. Quaranta, "A review of some charge transport properties of silicon," *Solid-State Electron.*, vol. 20, p. 77-89, 1977.

[Jac89] C. Jacoboni and P. Lugli, *The Monte Carlo Method for Semiconductor Device Simulation*, p. 144, Springer-Verlag, 1989.

[Jae80] R.C. Jaeger and F.H. Gaensslen, "Simulation of impurity freeze out through numerical solution of Poisson's equation with application to MOS device behavior," *IEEE Trans. Elec. Dev.*, vol. ED-27, no. 5, pp. 914-920, 1980.

[Jag69] R. Jaggi, "High-field drift velocities and current densities in silicon and germanium," *Helv. Phys. Acta*, vol. 42, pp. 941-943, 1969.

[Jain89] S.C. Jain, T.J. Gosling, D.H.J. Totterdell, J. Poortmans, R.J. Mertens, J. Nijs and R. Van Overstaeten, Late news paper presented at ESSDERC '89, Berlin, Sept. 11-15, 1989.

[Joh89] H. Johansson, S. Rudner, D-X. Xu and M. Willander, "Determination of very short minority carrier lifetimes in Si/Ge heterostructure p-n junctions," International workshop on physics of semiconductor devices, New Delhi, India, Dec. 11-15, 1989.

[Jor85] H. Jorke and H.J. Herzog, "Mobility enhancement in modulation doped Si-$Si_{1-x}Ge_x$ superlattice grown by molecular beam epitaxy," *Proc. 1st Int. Symp. Silicon Molecular Beam Epitaxy,* J.C. Bean Ed., Pennington, N.J.: Electrochemical Soc., 1985, p. 352.

[Kar90] M. Karlsteen and M. Willander, "Optimized frequency characteristics of Si/SiGe heterojunction and conventional bipolar transistors," *Solid-State Electron.*, vol. 33, no. 2, pp. 199-204, 1990.

[Kin89] C.A. King, J.L. Hoyt, C.M. Gronet, J.F. Gibbons, M.P. Scott and J. Turner, "Si/$Si_{1-x}Ge_x$ heterojunction bipolar transistors produced by limited reaction processing," *IEEE Elec. Dev. Lett.*, vol. 10, no. 2, pp. 52-54, Feb. 1989.

[Kot79] N. Kotani and S. Kawazu, ""Computer analysis of punch-through in MOSFET's," *Solid-State Electron.*, vol. 22, pp. 63-70, 1979.

[Kri85] S. Krishanmurthy, A. Sher and A-B. Chen, "Generalized Brooks' formula and the electron mobility in Si_xGe_{1-x} alloys," *Appl. Phys. Lett.*, vol. 47, no. 2, pp. 160-162, 1985.

[Kro57] H. Kroemer, "Theory of wide-gap emitter for transistors," *Proc. IRE*, vol. 45, no. 11, pp. 1535-1537, Nov. 1957.

[Kro82] H. Kroemer, "Heterostructure bipolar transistors and integrated circuits, *Proc. IEEE*, vol. 70, no. 1, pp. 13-25, Jan. 1982.

[Lau90] S.E. Laux and W. Lee, "Collector signal delay in the presence of velocity overshoot," *IEEE ELec. Dev. Lett.*, vol. ED-11, no. 4, pp. 174-175, Apr. 1990.

[Lun80] M.S. Lundstrom, "Numerical analysis of silicon solar cells," Purdue University, School of Electrical Engineering Tech. Rep. TR-EE 80-27, Dec. 1980.

[Lun81] M.S. Lundstrom, R.J. Schwartz and J.L. Gray, "Transport equations for the analysis of heavily doped semiconductor devices," *Solid-State Electron.*, vol. 24, pp. 195-202, 1981.

[Mae82] H.M. Manesevit, I.S. Gergis and A.B. Jones, "Electron mobility enhancement in epitaxial multilayer Si-$Si_{1-x}Ge_x$ alloys films on (100) Si," *Appl. Phys. Lett.*, vol. 41, no. 5, pp. 464-466, 1982.

[Manc75] O. Manck, Numerische Analyse des Schaltverhaltens eines zweidimensionalen bipolaren Transistors, Dissertation, Technische Hochschule Aachen, 1975.

[Man82] O. Mandelung, *Vol. 17a, Semiconductors: Intrinsic properties of group IV elements and III-V, II-VI, and I-VII compounds*, Springer-Verlag, Germany, p.454, 1982.

[Mas83] G. Masetti, M. Severi and S. Solmi, "Modeling of carrier mobility against carrier concentration in arsenic-, phosphorus-, and boron-doped silicon," *IEEE Trans. Elec. Dev.*, vol. ED-30, no. 7, pp.764-769, 1983.

[Mat74] J.W. Matthews and A.E. Blakeslee, "Defects in epitaxial multilayers - I: Misfit dislocations," *J. Chrystal Growth*, vol. 27, p. 118, 1974.

[Med76] H.R. Meddins and J.E. Parrot, "The thermal and thermoelectric [illegible]

[illegible]

[Mey86] B.S. Meyerson, "Low temperature silicon epitaxy by ultrahigh vacuum/chemical vapor deposition," Appl. Phys. Lett., vol. 48, pp. 797-799, Mar. 1986.

[Mor90] H. Morkoc and G.B. Gao, "Heterojunction bipolar transistors crack the 200 GHz barrier," to be submitted to *IEEE Circuits and Devices*, 1990.

[Neu81] A. Neugroschel, S.C. Pao and F.A. Lindholm, "A method for determining energy gap narrowing in highly doped semiconductors," *IEEE Trans. Elec. Dev.*, vol. ED-29, pp. 894-902, 1981.

[Neu83] G.W. Neudeck and R.F. Pierret, "The pn junction diode," *Vol. II, The modular series in solid state devices*, pp. 50-53, Addison-Wesley, 1983.

[Nor67] C.B. Norris, Jr., and J.F. Gibbons, "Measurement of high-field carrier drift velocities in silicon by a time-of-flight technique," *IEEE Trans. Elec. Dev.*, vol. ED-14, pp. 38-43, Jan. 1967.

[Pat88] G.L. Patton, S.S. Iyer, S.L. Delage, S. Tiwari and J.M.C. Stork, "Silicon-germanium-base heterojunction bipolar transistors by molecular beam epitaxy," *IEEE Elec. Dev. Lett.*, vol. 9, no. 4, pp. 165-167, Apr. 1988.

[Pat89] G.L. Patton, D.L. Harame, J.M.C. Stork, B.S. Meyerson, G.J.Scilla and E. Ganin,"Graded-SiGe-base, poly-emitter heterojunction bipolar transistors," *IEEE Elec. Dev. Lett.*, vol. 10, no. 12, pp. 534-536, Dec. 1989.

[Pat90] G.L. Patton, J.H. Comfort, B.S. Meyerson, E.F. Crabbe, G.J. Scilla, E. De Fresart, J.M.C. Stork, J.Y.C. Sun, D.L. Harame and J.N. Burghartz, "75 GHz f_T SiGe-base heterojunction bipolar transistors," *IEEE Elec. Dev. Lett.*, vol. 11, no. 4, pp. 171-173, 1990.

[Pea89] T.P. Pearsall, "Silicon-germanium alloys and heterostructures: optical and electronic properties," *CRC Critical Reviews in Solid State and Materials Sciences.*, vol. 15, Issue 6, pp. 551-600, 1989.

[Pej89] B. Pejcinovic, L.E. Kay, T-W. Tang and D.H. Navon, "Numerical simulation and comparison of Si BJT's and $Si_{1-x}Ge_x$ HBT's," *IEEE Trans. Elec. Dev.*, vol. ED-36, no. 10, pp. 2129-2137, 1989.

[Peo85] R. People and J.C. Bean, "Calculation of critical layer thickness versus lattice mismatch for Ge_xSi_{1-x}/Si strained layer heterostructures," *Appl. Phys. Lett.*, vol. 47, p.322, 1985.

[Peo86] R. People, "Physics and applications of Ge_xSi_{1-x}/Si strained layer heterostructures," *IEEE J. Quantum Elec.*, vol. 22, no. 9, pp. 1696-1710, Sept. 1986.

[Plu77] J.C. Plunkett and J.L. Stone, "A computer algorithm for accurate and repeatable profile analysis of using anodization and stripping of silicon," *Solid-State Electron.*, vol. 20, p. 447-453, 1977.

[Poo89] J. Poortmans, R.P. Mertens, S.C. Jain, J. Nijs and R. Van Overstraeten, *Proc. ESSDERC 1989*, Berlin, Sept. 11-15, p. 807, 1989.

[Rac89] M. Racanelli and D.W. Grove, "Calculated high frequency performance of an npn $Si_{1-x}Ge_x$ HBT," Department of Electrical and Computer Engineering, Carnegie Mellon University, 1989.

[Sch84] R.J. Schuelke, "Numerical simulation of semiconductor heterostructures," Doctoral Thesis, Purdue University, Aug. 1984.

[Shi90] N. Shigyo, H. Tanimoto, M. Norishima and S. Yasuda, "Minority carrier mobility model for device simulation," *Solid-State Electron.*, vol. 33, no. 6, pp. 727-731, 1990.

[Sho48] W. Schockley, U.S. Patent No. 2,569,347, filed June 26 1948, issued Sept. 25, 1951.

[Slo76] J.W. Slotboom and H.C. DeGraaff, "Measurements of bandgap narrowing in Si bipolar transistors," *Solid-State Electron.*, vol. 19, p. 857, 1976.

[Smi87] C. Smith and A.D. Welbourn, *"IEEE Proc. Bipolar Circuits and Technology meeting,"* Minneapolis, p. 57, 1987.

[Sug89] M. Sugiyama, "A 40 GHz f_T Si bipolar transistor LSI technology," *IEDM Tech. Dig.*, Dec. 1989, pp. 221-224.

[Sut77] J.E. Sutherland and J.R. Hauser, "A computer analysis of heterojunction and graded composition solar cells," *IEEE Trans. Elec. Dev.*, vol. ED-24, no. 4, pp. 363-372, 1977.

[Swi86a] S.E. Swirhun, J.A. del Alamo and R.N. Swanson, "Measurement of hole mobility in heavily doped n-type silicon," *IEEE Elec. Dev. Lett.*, vol. EDL-7, no. 3, pp.168-171, 1986.

[Swi86b] S.E. Swirhun, Y-H. Kwark and R.M. Swanson, *Tech. Dig. IEDM*, p. 24, 1986.

[Sze81] S.M. Sze, *Physics of semiconductor devices*, second edition, p. 850, John Wiley & Sons, 1981.

[Tan89] D.D. Tang and P.F. Lu, *IEEE Elec. Dev. Lett.*, vol. 10, p. 67, 1989.

[Tat88] T. Tatsumi, H. Hirayama and N. Aizaki, "Si/$Ge_{0.3}Si_{0.7}$ heterojunction bipolar transistor made with Si molecular beam epitaxy," *Appl. Phys. Lett.*, vol 52, no 11, pp. 895-897, Mar. 14 1988.

[Tem88] H. Temkin, J.C. Bean, A. Antreasyan and R. Leibenguth, "Ge_xSi_{1-x}/Si strained layer heterostructure bipolar transistors," *Appl. Phys. Lett.*, vol. 52, no. 13, pp. 1089-1091, March 28 1988.

[Tho82] K.K. Thornber, "Current equation for velocity overshoot," *IEEE Elec. Dev. Lett.*, vol. EDL-3, no.3, pp. 69-71, 1982.

[Uga89] M. Ugajin, S. Konaka and K. Yokoyama, "A simulation study of high-speed heteroemitter bipolar transistors," *IEEE Trans. Elec. Dev.*, vol. 36, no. 6, pp. 1102-1109, June 1989.

[Wie80] A.W. Wiedner, "Emitter effects in shallow bipolar devices: measurements and consequences," *IEEE Journal of Solid State Circuits*, vol. SC-15, p. 467, 1980.